

Improving Data Throughput for Single-Conductor Wireless Power Transfer Systems Employing Sheath Helices

by

Semion Belau

A thesis submitted in partial fulfillment of the requirements for the degree of

Master of Science
in
Electromagnetics and Microwaves

Department of Electrical and Computer Engineering
University of Alberta

© Semion Belau, 2020

Abstract

Historically, power transmission and data communication have been dealt with as separate problems. While communication has been conducted wirelessly for over a century, power has traditionally been transmitted via transmission line. However, the recent push for wireless power transmission (WPT) has sparked new interest in integrating the two.

This thesis investigates the capability of a novel single-conductor WPT system to be used as a communication channel. The system was used to support the transfer of on-off keyed data with and without encoding. Messages were recovered using a software-defined receiver and the results showed that the system is able to support data rates in the hundreds of kilobits per second, which is appropriate for RFID and NFC. However, this first investigation evidenced that data rates were limited by: (a) the ripple voltage produced at the output of the receiver and (b) the bandwidth of the channel, warranting two other investigations into ripple voltage reduction and bandwidth enlargement.

A mathematical criterion was formulated in order to minimize the ripple voltage and improve the reliability of communication with a low modulation index under amplitude shift keying. Simulation results with a software-defined receiver confirmed that the use of the criterion produces the smallest bit error rate.

Bandwidth enlargement was undertaken as a whole system design by employing band-pass filter (BPF) theory. Four single-conductor systems, each with a distinct combination of filter order and bandwidth, were simulated. To assist in the design, an equivalent lumped-element model was derived for each system. The simulation results illustrated the effectiveness and ease of using BPF theory in designing single-conductor systems with different bandwidths.

Preface

This thesis presents research undertaken into communication on a single-conductor system. The systems under investigation in Chapter 4 were simulated and constructed by Fabiano Cezar Domingos, Susanna Vital de Campos de Freitas, and Rashid Mirzavand.

Elements of Sections 4.1 and 4.2 were presented at the 2019 IEEE Wireless Power Transfer Conference and published in the conference proceedings under the title “Data Communication Over a Novel Capacitive Resonant Wireless Power Transmission System.” This paper has been co-authored by Susanna Vital de Campos de Freitas, Fabiano Cezar Domingos, Dr. Rashid Mirzavand, and Dr. Pedram Mousavi.

A version of Sections 4.1 and 4.2 was submitted for publication in the IET Science, Measurement & Technology journal under the title “Characterization of a Resonant Capacitively Coupled Wireless Power Transfer System for Communication Purposes at 6 MHz”. This paper has been co-authored by Susanna Vital de Campos de Freitas, Fabiano Cezar Domingos, Dr. Rashid Mirzavand, and Dr. Pedram Mousavi.

A version of Section 4.3 was accepted for presentation at the 2020 IEEE Wireless Power Transfer Conference under the title “Low Ripple Envelope Detection for Load Modulated Communication in SWIPT”. This paper has been co-authored by Susanna Vital de Campos de Freitas, Fabiano Cezar Domingos, Dr. Rashid Mirzavand, and Dr. Pedram Mousavi.

Acknowledgments

First, I would like to thank my supervisor Dr. Pedram Mousavi for taking me into his group and for his support and encouragements. His optimism was infectious and pushed me to overcome the challenges that arose as part of my research. Apart from his academic support, Dr. Mousavi strove to create a cohesive group and make me feel welcome, for which I am extremely grateful. May his, Dr. Mojgan Daneshmand's, and their daughters' memory be a blessing.

Next, I would like to thank Dr. Rashid Mirzavand and the rest of my research group. Their help, advice, support, and collaboration are highly valued and were influential in the development of my research.

I would also like to acknowledge my course professors for enhancing my knowledge in the fields of signal processing, electromagnetism, and communication and for further strengthening my curiosity in them.

Finally, I want to thank my family and my friends for all their support during this journey. Without their kind words, acts of kindness, encouragement, reassurances, and confidence in me, I would not have been able to succeed. They were always there to remind me of my worth and make sure that I felt loved.

Table of Contents

List of Tables	vii
List of Figures	viii
List of Abbreviations	xi
Chapter 1 Introduction	1
1.1 A short history of wireless power transmission and communication.....	1
1.2 Motivation	3
1.3 Objective.....	3
1.4 Thesis structure.....	4
Chapter 2 Inductive Wireless Power Transfer	5
2.1 Fundamentals of inductive wireless power transfer	5
2.1.1 Faraday’s Law	5
2.1.2 Ampère’s Law.....	6
2.1.3 Inductance	7
2.2 Resonant inductive WPT.....	13
2.2.1 Power gain definitions	13
2.2.2 Non-resonant inductive WPT	14
2.2.3 Magnetic resonance WPT	17
Chapter 3 The Sheath Helix and Single-Conductor Power Transmission	28
3.1 Resonant modes on the sheath helix	29
3.1.1 Half-wave sheath helix.....	30
3.1.2 Quarter-wave sheath helix.....	32
3.2 Sheath helices in single-conductor WPT	33
Chapter 4 Communication for Wireless Power Transfer Systems	36
4.1 The channel frequency response and measurement setup.....	36
4.2 Communication on a single-conductor channel	39
4.2.1 Envelope detector	40
4.2.2 Fifth-order Butterworth band-pass filter	43

4.2.3	Schmitt trigger	43
4.2.4	Line codes	46
4.2.5	Simulation and measurement results.....	47
4.3	Improved asynchronous ASK receiver.....	55
4.3.1	Envelope detector	55
4.3.2	Input band-pass filter	55
4.3.3	Simulation results	56
4.3.4	Application to WIPT	60
Chapter 5	Band-Pass Filter Theory in the Design of Single-Conductor Channels	62
5.1	Inductively coupled resonators in the design of maximally flat band-pass filters	64
5.2	Sheath helix equivalent circuit model.....	67
5.2.1	Quarter-wave sheath helix.....	67
5.2.2	Capacitively coupled quarter-wave sheath helices	70
5.3	Implementation of quarter wave sheath helices in BPFs.....	73
5.3.1	Second order BPF with 10% bandwidth	73
5.3.2	Second order BPF with 50% bandwidth.....	74
5.3.3	Third order BPF with 10% bandwidth.....	76
5.3.4	Third order BPF with 50% bandwidth.....	77
Chapter 6	Conclusion.....	79
6.1	Future work.....	80
References.....		82
Appendix A.	Isolation Transformers.....	88
Appendix B.	Probability of Error for the Asynchronous Detection of OOK Data	91
Appendix C.	Envelope Detector Algorithm	94

List of Tables

Table I	Comparison of 2-resonator and 3-resonator systems	24
Table II	System dimensions and component values.....	38
Table III	LPF and BPF parameters.....	48
Table IV	Sheath helix dimensions.....	67
Table V	Design parameters of the second order BPF with 10% bandwidth	73
Table VI	Coil inductor parameters for the second order BPF with 10% bandwidth	74
Table VII	Design parameters of the second order BPF with 50% bandwidth	75
Table VIII	Coil inductor parameters for the second order BPF with 50% bandwidth	75
Table IX	Design parameters of the third order BPF with 10% bandwidth	76
Table X	Coil inductor parameters for the third order BPF with 10% bandwidth.....	77
Table XI	Design parameters of the third order BPF with 50% bandwidth.....	78
Table XII	Coil inductor parameters for the third order BPF with 50% bandwidth	78

List of Figures

Figure 2.1	Visualization of Faraday’s law (left) and Ampère’s law (right).	5
Figure 2.2	Inductance relates the current to the magnetic flux it generates.	8
Figure 2.3	Multi-turn inductor.	9
Figure 2.4	Coupled inductors with a short-circuited secondary.....	12
Figure 2.5	Generalized two-port network.....	13
Figure 2.6	Basic configuration for inductive WPT.....	14
Figure 2.7	Power gain and $ S_{21} ^2$ plots for $R_S = R_L = 50 \Omega$, $R_1 = 3 \Omega$, $R_2 = 6 \Omega$, $L_1 = 1 \mu\text{H}$, and $L_2 = 2.2 \mu\text{H}$	16
Figure 2.8	Compensated inductive WPT circuit.	17
Figure 2.9	$ S_{21} ^2$ plots for (a) $R_S = R_L = 50 \Omega$, $R_1 = 3 \Omega$, $R_2 = 6 \Omega$, $L_1 = 1 \mu\text{H}$, $L_2 = 3.3 \mu\text{H}$, $C_1 = 253 \text{ pF}$, and $C_2 = 77 \text{ pF}$ and (b) $R_S = R_L = 50 \Omega$, $R_1 = R_2 = 6 \Omega$, $L_1 = L_2 = 3.3 \mu\text{H}$, and $C_1 = C_2 = 77 \text{ pF}$	19
Figure 2.10	Power gain for magnetic resonance WPT with $R_S = R_L = 50 \Omega$, $R_1 = 3 \Omega$, $R_2 = 6 \Omega$, $L_1 = 1 \mu\text{H}$, $L_2 = 2.2 \mu\text{H}$, $C_1 = 253 \text{ pF}$, and $C_2 = 115 \text{ pF}$	22
Figure 2.11	3-resonator WPT circuit.	23
Figure 2.12	Range of load impedances available to 2- and 3-resonator systems with $R_1 = 50 \Omega$ and $L_1 = L_2 = L_3 = 1 \mu\text{H}$ at a resonant frequency of $f_0 = 10 \text{ MHz}$	24
Figure 2.13	(a) Equivalent representation of a 2-resonator WPT circuit. (b) Even mode half circuit and (c) odd mode half circuit for the circuit in (a).	27
Figure 3.1	Stray capacitance between the windings of a coil.....	29
Figure 3.2	Four-coil system setup used by Kurs et al. [8] with two relay resonators.....	31
Figure 3.3	Half-wave sheath helix.....	31
Figure 3.4	Quarter-wave sheath helix.	33
Figure 3.5	Coupling to and from (a) an arbitrarily shaped conductor and (b) a capacitive discontinuity using quarter-wave sheath helices.	35
Figure 4.1	(a) System diagram. (b) System implemented in the lab with the transformers used in the inset.	37
Figure 4.2	Frequency response of the channel.	39
Figure 4.3	SDR block diagram.	40
Figure 4.4	Spectra of the rectified signal as given by (4.4) and an ideal low-pass filter.....	41
Figure 4.5	Square-law envelope detector.....	42

Figure 4.7	Hysteresis loop of Schmitt triggers.....	44
Figure 4.6	Combined effect of an LPF and various BPFs with different cutoff frequencies with $f_m = 1$ MHz	44
Figure 4.8	Schmitt trigger vs. a single threshold detector.	45
Figure 4.9	BER vs. SNR for a single threshold detector and a Schmitt trigger.	46
Figure 4.10	Modified Miller encoding as specified in [51].....	46
Figure 4.11	BER vs. SNR for OOK modulated signals with varying data rates: (a) 106 kb/s, (b) 424 kb/s, and (c) 1000 kb/s.	50
Figure 4.12	Eye diagrams for the demodulated OOK signals with data rates: (a) 106 kb/s, (b) 424 kb/s, and (c) 1000 kb/s.	51
Figure 4.13	BER vs. SNR for MMC modulated signals with varying data rates: (a) 26.5 kb/s, (b) 106 kb/s, and (c) 250 kb/s.....	53
Figure 4.14	Eye diagrams for demodulated MMC modulated signals with data rates: (a) 26.5 kb/s, (b) 106 kb/s, and (c) 250 kb/s.	54
Figure 4.15	Contribution of the BPF in balancing the symbol durations.....	56
Figure 4.16	(a) Qi channel and (b) its frequency response (S_{21} parameter).	58
Figure 4.17	Biphase mark line code [54].	58
Figure 4.18	BER performance for various cutoff frequencies: (a) 14 kHz, (b) 6 kHz, (c) 1.28 kHz, (d) 357.1 Hz, (e) 89.3 Hz, and (f) 44.6 Hz. The dashed line approximates the best performance at each frequency.	59
Figure 4.19	Performance comparison of receivers with different cutoff frequencies.	60
Figure 4.20	Received signal after passing through an envelope detector with $f_{c,LPF} = 357.1$ Hz. The HIGH and LOW level durations are $\Delta t_{AB} = 253 \mu\text{s}$ and $\Delta t_{BC} = 246 \mu\text{s}$, respectively.....	60
Figure 5.1	Channel frequency response for a resonant WPT system with frequency splitting.....	62
Figure 5.2	An N^{th} order (a) ladder network and (b) impedance transformer synthesis of a BPF.	64
Figure 5.3	Impedance inverter implemented as an inductively coupled circuit.	66
Figure 5.4	N^{th} order inductively coupled resonator synthesis of a BPF.....	67
Figure 5.5	Equivalent lumped-element model of the quarter-wave sheath helix resonator. ..	68
Figure 5.6	(a) HFSS model of the quarter-wave sheath helix resonator. (b) Reactances of the sheath helix and its equivalent lumped-element circuit.	69

Figure 5.7	(a) HFSS model of the half-wave sheath helix resonator. (b) Equivalent lumped-element circuit of the half-wave sheath helix resonator. (c) Reactances of the sheath helix and its equivalent lumped-element circuit.	71
Figure 5.8	(a) HFSS model of the half-wave sheath helix resonator with a capacitive discontinuity. (b) Equivalent lumped-element circuit of the HFSS model. (c) Reactances of the HFSS model and the equivalent lumped-element circuit.	72
Figure 5.9	Circuit representation of a second order BPF with a sheath helix.	73
Figure 5.10	$ S_{21} $ parameters of the second order BPF with 10% bandwidth.	74
Figure 5.11	$ S_{21} $ parameters of the second order BPF with 50% bandwidth.	75
Figure 5.12	Circuit representation of the third order BPF with sheath helices and a capacitive discontinuity.	76
Figure 5.13	$ S_{21} $ parameters of the third order BPF with 10% bandwidth.	77
Figure 5.14	$ S_{21} $ parameters of the third order BPF with 50% bandwidth.	78
Figure A.1	(a) An inductively-loaded monopole antenna with an electrically small ground plane fed directly by a coaxial cable. (b) An inductively-loaded monopole fed with an isolation transformer.	89
Figure A.2	Measured channel response with up to five transformers at each port.	90
Figure B.2	Shifting threshold level as the SNR decreases for SNRs of (a) 15 dB, (b) 10 dB, (c) 5 dB, and (d) 0 dB. The noise distribution is $f_0(\rho)$ and $f_1(\rho)$ when bit 0 and bit 1 are transmitted, respectively, with $A = 5$	93

List of Abbreviations

AC	Alternate current
ADS	Advanced Design System
AM	Amplitude modulation
ASK	Amplitude shift keying
AWG	American wire gauge
AWGN	Additive white Gaussian noise
BER	Bit error rate
BPF	Band-pass filter
DC	Direct current
EMF	Electromotive force
FSK	Frequency shift keying
HFSS	High-frequency structure simulator
IIR	Infinite impulse response
ISI	Intersymbol interference
LHS	Left-hand side
LPF	Low-pass filter
MIMO	Multiple-input, multiple-output
MMC	Modified Miller code
NFC	Near-field communication
OFDM	Orthogonal frequency-division multiplexing
OOK	On-off keying
PAPR	Peak-to-average power ratio
RF	Radio frequency
RFID	Radio frequency identification
RHS	Right-hand side
SDR	Software-defined receiver
SNR	Signal-to-noise ratio
SPS	Solar-power satellites
SWIPT	Simultaneous wireless information and power transfer
VNA	Vector network analyzer
WIPT	Wireless information and power transfer

WPT Wireless power transmission
WSN Wireless sensor networks

Chapter 1 Introduction

1.1 A SHORT HISTORY OF WIRELESS POWER TRANSMISSION AND COMMUNICATION

The areas of wireless transmission of power and data are rooted in two discoveries of the 19th century. In 1820, Hans Christian Ørsted observed that an electric current affected the direction pointed to by a compass, thus discovering that a current produces a magnetic field and establishing the first link between electricity and magnetism. This discovery led to the works of Jean-Baptiste Biot and Félix Savart, of the Biot-Savart law, and to those of André-Marie Ampère, of the renowned Ampère's law and the unit of current named in his honour. In 1831, Michael Faraday discovered the second link between electricity and magnetism when he observed that a changing magnetic flux produced a current: Faraday's law [1]. This law and Ørsted's observation (as well as subsequent works by Biot, Savart, and Ampère), which is described by Ampère's law, form the basis of transformer action and inductive power transfer.

It was James Clerk Maxwell who, in 1865, formulated the preceding discoveries on electricity and magnetism in 20 equations in his paper titled "A Dynamical Theory of the Electromagnetic Field" [1] and later, in 1873, in his "Treatise on Electricity and Magnetism" [2]. In these works, Maxwell noted that a changing electric field was equivalent to a current in producing magnetic fields. This correction to Ampère's law led him to theorize that electric and magnetic fields could propagate through a medium in the form of an electromagnetic wave that travelled at the speed of light, which was experimentally confirmed by Heinrich Rudolf Hertz in 1886 [1]–[3]. Thus, electromagnetic wave propagation forms the basis of radiative power transfer and modern communication technologies.

In 1901, Guglielmo Marconi was able to wirelessly send a telegraph radio signal across the Atlantic Ocean from Poldhu, Cornwall to St. John's, Newfoundland with an antenna [4]. Around the same time, Nikola Tesla experimented with wireless power transfer (WPT) using large coils in order to transfer power through the ionosphere [5], [6]. While Tesla's wireless power experiments were not fruitful, Marconi's experiments formed the basis of wireless communication and eventually matured into today's communication networks. Wireless power would not receive much attention for several decades.

In 1963, William C. Brown and his team at Raytheon demonstrated their microwave power transmission system, which converted 400 W of microwave power to 100 W of DC power. Further innovation together with Professor Roscoe H. George of Purdue University culminated in the development of the first rectenna and a demonstration of wireless power transfer to a model helicopter in 1964. In working towards solar-power satellites (SPS), in which a satellite converts solar energy to microwave energy and then radiates it down to Earth, a WPT demonstration was made in 1975 at the JPL Goldstone Facility in which 30 kW of DC power was harvested at a distance of 1.6 km from the transmitter [7]. Ever since, steady research has been undertaken in WPT.

A significant breakthrough in near-field WPT occurred in 2007 when Marin Soljačić and his team at the Massachusetts Institute of Technology showed that efficiency gains can be achieved when the receiver and transmitter are operated in resonance at the same frequency [8], sparking new research into resonant WPT.

In recent years, two industrial alliances have been formed to standardize and commercialize near-field WPT: the Wireless Power Consortium (WPC), formed in 2008 and administering the Qi standard since 2010 [9], and the AirFuel Alliance, formed 2015 from the merge between the Alliance for Wireless Power and the Power Matter Alliance [10]. Currently, Qi is leading the market [11].

Although many commercial products exist that implement either the Qi or AirFuel standards, RFID is an even older and more ubiquitous technology that can be traced back to the 1970's [12]. The mechanism of operation is simple: a transmitter sends a signal to a passive (battery-less) receiver and the receiver then uses this signal for both energy harvesting as well as communication with the transmitter via backscatter (or load) modulation. Unlike the Qi and AirFuel standards, RFID can be implemented in both the near- and far-fields.

Given that research in WPT stretches back to the 1960's, near-field WPT has yet to reach ubiquity and far-field WPT has yet to be implemented in a network (whereas wireless cellular communication is already in its fifth generation) [13]. Furthermore, there is a push to integrate WPT and wireless communication into wireless information and power transfer (WIPT). Under this new paradigm, data and power will be transmitted on the same waveform (called simultaneous WIPT or SWIPT) or power will be transmitted in the downlink and data will be

transmitted in the uplink (under the schemes of wirelessly powered communication and wirelessly powered backscatter communication) [13].

1.2 MOTIVATION

Wireless electronics have penetrated almost every aspect of our lives and are expected to continue to do so with wireless sensor networks (WSNs) and the Internet of Things (IoT). Thus far, this trend is mostly limited to our communication networks (e.g., Wi-Fi and the implementation of 5G communication). However, as the number of devices continues to grow, there will be an increased need to power them. Powering these devices with wires will become highly inconvenient and expensive, whereas batteries take up a lot of space in electronics and require either charging or replacement (which is wasteful). In some cases, it is even inconvenient, costly, or hazardous to replace the battery, as in biomedical implants or industrial sensors that may be buried underground.

In the case of biomedical implants, near-field wireless power transfer is an attractive solution [6]. However, both near- and far-field WPT and communication are impeded when the device is buried underground or is otherwise obstructed from the WPT transmitter by a conductive object. In such cases, it is conducive to utilize the existing conductive infrastructure to transfer both power and data [14], [15], which requires novel designs and innovative, elegant solutions.

1.3 OBJECTIVE

The objective of this thesis is to extend the research presented in [16]–[19] on WPT via sheath helices and a single conductor (henceforth termed single-conductor WPT or single-conductor systems) to include data transfer. Whereas the focus of [16]–[19] was strictly limited to power transmission, different challenges are present when attempting to reliably transmit and receive data, chief among them being bandwidth.

Moreover, with accelerated research into the simultaneous transmission of power and data, methods for the efficient harvesting of power and successful reception of data are necessary such that they do not interfere with each other. This is a highly desired goal for battery-less electronics and is therefore discussed here as well.

Hence, the objectives of the thesis are threefold:

1. Demonstrate the ability of the presented system to accommodate data communication (with a focus on commercial data transmission such as RFID and near-field communication).
2. Develop design criteria and guidelines for the reception of amplitude shift keyed data modulated on top of a power signal with minimal disruption to power harvesting.
3. Formalize the design of single-conductor systems where bandwidth is the prime design parameter as opposed to a consequence of the design.

1.4 THESIS STRUCTURE

This thesis is organized as follows:

Chapter 2 develops of the fundamentals of inductive coupling and power transfer by deriving them from Maxwell's equations. The concepts are then developed into magnetic resonance WPT as an improvement on traditional inductive power transfer. Additionally, a relay system is discussed.

Chapter 3's focus is on single-conductor transmission lines with a focus on the sheath helix, which is used in the design of the single-conductor system.

Chapter 4 characterizes the system as a communication channel for amplitude modulated data. The chapter also discusses the architectural requirements of the receiver for successful asynchronous reception of the data. These ideas eventually evolve into a new criterion for the asynchronous receiver.

Chapter 5 focuses on the design of single-conductor systems using band-pass filter theory in order to enable designers to have control of the bandwidth and thus enhance both the communication and power transfer capabilities of the system. Examples with simulation results are provided to showcase the advantages of this design procedure.

Finally, Chapter 6 concludes this thesis with suggestions for future work and improvements.

Chapter 2 Inductive Wireless Power Transfer

This chapter provides an overview of inductive WPT and its progression into resonant WPT. A review of Maxwell's equations is presented first, from which the fundamental concepts of inductive WPT will be developed. These basic concepts are then used to introduce resonant WPT and its advantages over non-resonant WPT. In order to compare the two schemes, definitions of power gain are provided.

Additionally, a 3-resonator system is explored as the most basic case of a resonant WPT system with relays and its advantages over the 2-resonator system are discussed.

Finally, the chapter concludes with a brief discussion of the frequency splitting phenomenon inherent to resonant WPT.

2.1 FUNDAMENTALS OF INDUCTIVE WIRELESS POWER TRANSFER

2.1.1 FARADAY'S LAW

Faraday's law is given in its differential form by

$$\nabla \times \mathbf{E} = -\mu \frac{\partial \mathbf{H}}{\partial t} \tag{2.1}$$

Simply stated, Faraday's law says that a time-varying magnetic field \mathbf{H} gives rise to an electric field \mathbf{E} that circulates around the magnetic field lines and that the two are related by the magnetic permeability μ (Figure 2.1).

Integrating both sides over a surface \mathcal{S}

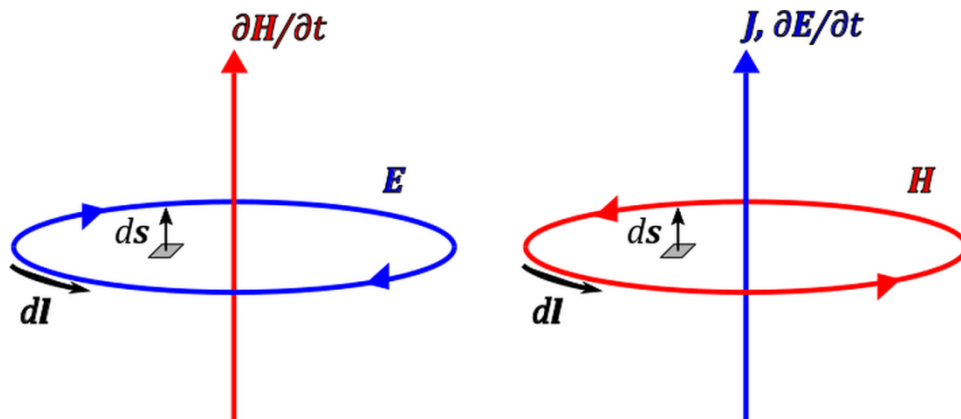


Figure 2.1 Visualization of Faraday's law (left) and Ampère's law (right).

$$\int_{\mathcal{S}} \nabla \times \mathbf{E} \cdot d\mathbf{s} = \oint_{\mathcal{C}} \mathbf{E} \cdot d\mathbf{l} = -\mu \frac{\partial}{\partial t} \int_{\mathcal{S}} \mathbf{H} \cdot d\mathbf{s} \quad (2.2)$$

where $d\mathbf{l}$ is a differential line element along the boundary curve \mathcal{C} that encloses \mathcal{S} and $d\mathbf{s}$ is a differential surface element of \mathcal{S} . The second integral was obtained by applying Stoke's theorem and represents an electromotive force (EMF), or voltage. This is Faraday's law in its integral form and it states that a time-varying magnetic flux through a surface \mathcal{S} , represented by the third integral, induces an EMF around the boundary curve \mathcal{C} that encloses said surface. The above equation can be more succinctly expressed as

$$\mathcal{E} = -\frac{\partial \Phi}{\partial t} \quad (2.3)$$

where \mathcal{E} is the induced EMF and Φ is the magnetic flux through surface \mathcal{S} .

Based on the above, when a free charged particle is placed in this field it will move under the action of the induced EMF. The direction of motion of this charged particle is such that it will induce a magnetic field that opposes the change in the first one in what is known as Lenz's law, which is represented by the minus sign on the RHS of Eq. (2.3). It follows that when a conductive loop is placed in the field such that the magnetic field lines penetrate the enclosed area, the free electrons in the conductor will flow to produce a current.

2.1.2 AMPÈRE'S LAW

The dual to Faraday's law is Ampère's law, which is given by its differential form

$$\nabla \times \mathbf{H} = \mathbf{J} + \varepsilon \frac{\partial \mathbf{E}}{\partial t} \quad (2.4)$$

The law states that a current density \mathbf{J} produces a magnetic field that circulates around it. It also states that time-varying electric fields can also produce a magnetic field that circulates around the electric field lines with a constant of proportionality ε , the electric permittivity (Figure 2.1). As with Faraday's law, integrating both sides over surface \mathcal{S}

$$\int_{\mathcal{S}} \nabla \times \mathbf{H} \cdot d\mathbf{s} = \oint_{\mathcal{C}} \mathbf{H} \cdot d\mathbf{l} = \int_{\mathcal{S}} \left(\mathbf{J} + \varepsilon \frac{\partial \mathbf{E}}{\partial t} \right) \cdot d\mathbf{s} \quad (2.5)$$

where the second integral was again obtained by invoking Stoke's theorem to arrive at Ampère's law in its integral form. The term $\varepsilon \frac{\partial \mathbf{E}}{\partial t}$ is called the displacement current and it plays a role in

the response of a capacitor to time-varying currents. However, in closed conductive loops, $\partial \mathbf{E} / \partial t = 0$ and (2.5) simplifies to

$$\oint_c \mathbf{H} \cdot d\mathbf{l} = I \quad (2.6)$$

where I is the total current flowing through the conductor.

2.1.3 INDUCTANCE

2.1.3.1 Self inductance

In much the same way that capacitance C is defined as the ratio of the charge Q present on a pair of conductors to the voltage V developed between them (mathematically described by $C = Q/V$), self-inductance L is defined as the ratio of the magnetic flux Φ to the current I that generates and encloses it (see Figure 2.2), as given by

$$L = \frac{\mu \int_s \mathbf{H} \cdot d\mathbf{s}}{I} = \frac{\Phi}{I} \quad (2.7)$$

Isolating Φ in (2.7) and differentiating with respect to time

$$L \frac{di}{dt} = \frac{d\Phi}{dt} = v \quad (2.8)$$

where I was changed to i to reflect the change from a DC to an AC quantity and the last equality is due to Faraday's law in (2.3), where v is the AC voltage developed across the inductor. In other words, inductance is the ability of an inductor to resist changes in current. It is prudent to mention that (2.8) is only valid for quasistatic conditions, i.e., when the inductor is electrically short such that the instantaneous AC current is nearly the same at all points along the inductor wire.

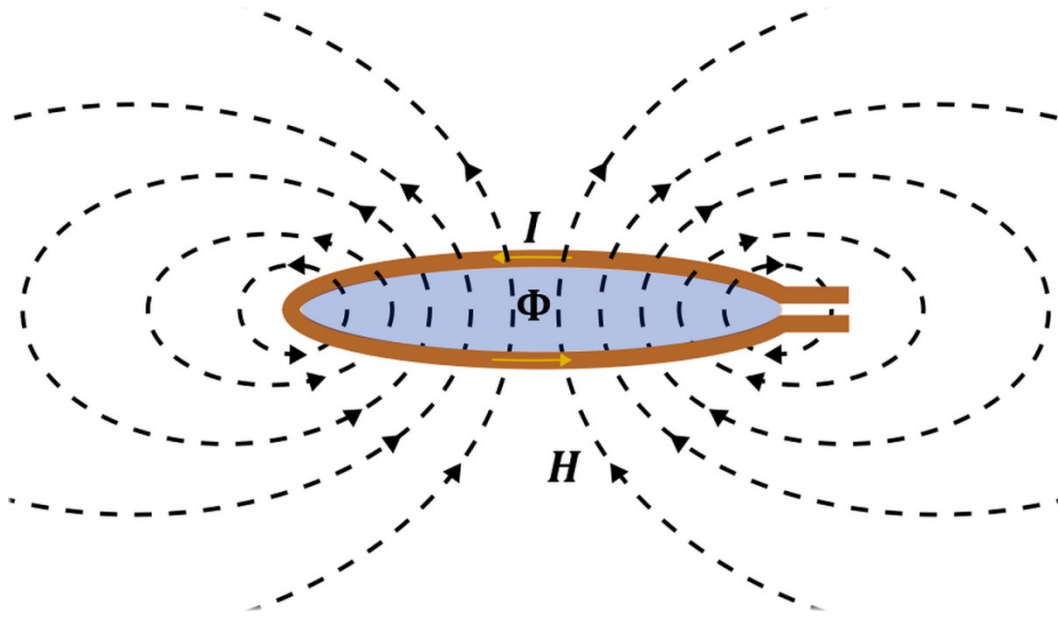


Figure 2.2 Inductance relates the current to the magnetic flux it generates.

A valuable property of inductance is that it can be increased conveniently by creating multi-turn inductors (Figure 2.3) where all the turns are connected in series such that the same current i flows in each. If the turns are close to each other such that all (or most) of the magnetic flux of one turn passes through all the other turns, then using (2.8) the voltage v_n across each loop of an N -turn inductor is given by

$$v_n = \sum_{n=1}^N \frac{d\Phi_n}{dt} = \frac{di}{dt} \sum_{n=1}^N L_n \quad (2.9)$$

where Φ_n is the flux produced by a single turn and L_n is the inductance of each individual loop. Because the turns are connected in series, the total voltage across the inductor is the sum of the single-turn voltages

$$v = \sum_{n=1}^N v_n = \frac{di}{dt} \sum_{n=1}^N \sum_{n=1}^N L_n = N \frac{di}{dt} \sum_{n=1}^N L_n \quad (2.10)$$

For identical loops, the inductance of each loop must be the same, i.e., $L_n = L_0$ for all n . Thus,

$$v = N^2 L_0 \frac{di}{dt} = L \frac{di}{dt} \quad (2.11)$$

The last equality demonstrates that the total inductance of a multi-turn inductor increases linearly with the square of the number of turns.

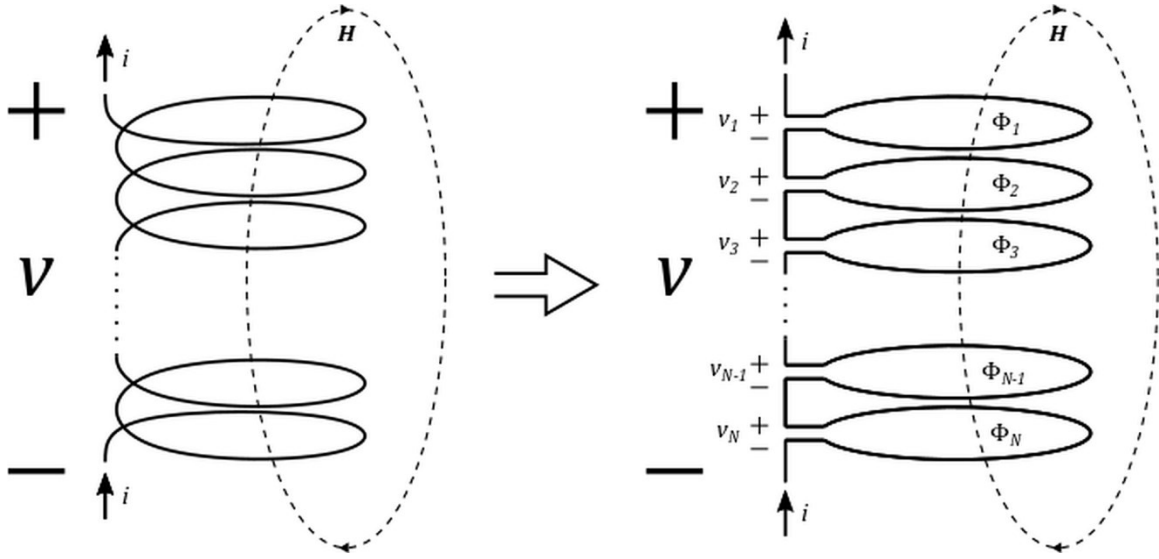


Figure 2.3 Multi-turn inductor.

2.1.3.2 Magnetic vector potential

Gauss' law for magnetic fields states that magnetic fields do not have point sources and is mathematically described by [20]

$$\nabla \cdot (\mu \mathbf{H}) = 0 \quad (2.12)$$

Using the identity $\nabla \cdot \nabla \times \mathbf{A} = 0$, we define

$$\mu \mathbf{H} = \nabla \times \mathbf{A} \quad (2.13)$$

Substituting this into (2.4) for a conductor and using another vector identity, we arrive at

$$\nabla \times \nabla \times \mathbf{A} = \nabla(\nabla \cdot \mathbf{A}) - \nabla^2 \mathbf{A} = \mu \mathbf{J} \quad (2.14)$$

To define a vector field completely, its divergence and curl must be defined and thus the divergence of \mathbf{A} can be set arbitrarily to zero, i.e., $\nabla \cdot \mathbf{A} = 0$. As a result (2.14) becomes

$$-\nabla^2 \mathbf{A} = \mu \mathbf{J} \quad (2.15)$$

To solve for \mathbf{A} , let us look at Gauss' law for electric fields [21]

$$\nabla \cdot \mathbf{E} = \frac{\rho}{\epsilon} \quad (2.16)$$

where ρ is the charge density that produces the electric field. Eq. (2.16) simply states that the source of electric fields is charge. The electric field can be written in terms of the electric potential as

$$\mathbf{E} = -\nabla V \quad (2.17)$$

Substituting into (2.16)

$$-\nabla \cdot \nabla V = -\nabla^2 V = \frac{\rho}{\varepsilon} \quad (2.18)$$

which takes the same form as (2.15). It is also known that the electric potential at a distance $\|\mathbf{r}\|$ from a charge distribution is given by

$$V = \frac{1}{4\pi\varepsilon} \int_{\mathcal{V}} \frac{\rho dv}{\|\mathbf{r}\|} \quad (2.19)$$

which is the solution to (2.18). Then by comparison, the solution to (2.15) is

$$\mathbf{A} = \frac{\mu}{4\pi} \int_{\mathcal{V}} \frac{\mathbf{J} dv}{\|\mathbf{r}\|} \quad (2.20)$$

Due to the similarities between (2.15) and (2.18) [or (2.19) and (2.20)], \mathbf{A} is called the magnetic vector potential.

The magnetic vector potential can be used to calculate magnetic flux as in

$$\Phi = \int_{\mathcal{S}} (\nabla \times \mathbf{A}) \cdot d\mathbf{s} = \oint_{\mathcal{C}} \mathbf{A} \cdot d\mathbf{l} \quad (2.21)$$

thereby replacing a surface integral with a simpler contour integral.

2.1.3.3 Mutual inductance

Consider two current carrying loops. As in (2.7), the mutual inductance M_{21} between them is defined as the ratio of the flux enclosed by one loop Φ_2 to the current I_1 flowing on the other loop, which produced it [20]

$$M_{21} = \frac{\Phi_2}{I_1} \quad (2.22)$$

Substituting (2.20) and (2.21) into (2.22)

$$M_{21} = \frac{\mu}{4\pi I_1} \oint_{\mathcal{C}_2} \int_{\mathcal{V}_1} \frac{\mathbf{J}_1 dv_1}{\|\mathbf{r}_{12}\|} \cdot d\mathbf{l}_2 \quad (2.23)$$

where \mathbf{r}_{12} is the displacement vector from the volume element dv_1 to the line element $d\mathbf{l}_2$. For quasistatic scenarios, i.e., where the fields vary slowly with time, the currents can be assumed to be distributed uniformly across the cross-sectional area of the conductors. Thus, the term $\mathbf{J}_1 dv_1$ can be written as $I_1 d\mathbf{l}_1$ or as $I_1 d\mathbf{l}_1$ (where the vector direction is absorbed by the line element) and (2.23) becomes

$$M_{21} = \frac{\mu}{4\pi} \oint_{C_2} \oint_{C_1} \frac{d\mathbf{l}_1 \cdot d\mathbf{l}_2}{\|\mathbf{r}_{12}\|} \quad (2.24)$$

The above result is known as Neumann's formula. Noting that the order of integration in this case is irrelevant and that the dot product is commutative, it is evident that

$$M_{21} = \frac{\mu}{4\pi} \oint_{C_2} \oint_{C_1} \frac{d\mathbf{l}_1 \cdot d\mathbf{l}_2}{\|\mathbf{r}_{12}\|} = \frac{\mu}{4\pi} \oint_{C_1} \oint_{C_2} \frac{d\mathbf{l}_2 \cdot d\mathbf{l}_1}{\|\mathbf{r}_{21}\|} = M_{12} \quad (2.25)$$

i.e., mutual inductance between two current loops is not dependent on the source of the magnetic field but only on the geometry of the two loops and their relative orientations. When the distance between two coupled coils is much larger than their dimensions, the mutual inductance between them is approximately proportional to the inverse cubed distance between them, i.e., $M_{ij} \propto d_{ij}^{-3}$ [20].

Next, the EMF produced in one coil due to the flux produced by the other coil is given by Faraday's law (2.3)

$$\mathcal{E}_2 = -M \frac{di_1}{dt} \quad (2.26)$$

The total EMF produced in the coil is the sum of the EMF produced by self-inductance [given by (2.3)] and the EMF produced by mutual inductance [given by (2.26)]. If there are N current carrying inductors then the voltage across each of the inductors is given by the matrix equation

$$\begin{bmatrix} v_1 \\ v_2 \\ \vdots \\ v_N \end{bmatrix} = \begin{bmatrix} L_1 & \pm M_{12} & \cdots & \pm M_{1N} \\ \pm M_{21} & L_2 & \cdots & \pm M_{2N} \\ \vdots & \vdots & \ddots & \vdots \\ \pm M_{N1} & \pm M_{N2} & \cdots & L_N \end{bmatrix} \times \frac{d}{dt} \begin{bmatrix} i_1 \\ i_2 \\ \vdots \\ i_N \end{bmatrix} \quad (2.27)$$

The \pm sign signifies that the mutual coupling can either enhance the voltage or decrease it depending on the relative current flows [as evidenced by the dot product in (2.24)]. If an inductor is wound such that an external magnetic field induces current flow in the same direction as the existing current, M takes on a positive sign, otherwise it takes on a negative sign. Since the voltages and currents of interest are sinusoidal, (2.27) can be written in phasor notation as

$$\begin{bmatrix} V_1 \\ V_2 \\ \vdots \\ V_N \end{bmatrix} = j\omega \begin{bmatrix} L_1 & \pm M_{12} & \cdots & \pm M_{1N} \\ \pm M_{21} & L_2 & \cdots & \pm M_{2N} \\ \vdots & \vdots & \ddots & \vdots \\ \pm M_{N1} & \pm M_{N2} & \cdots & L_N \end{bmatrix} \begin{bmatrix} I_1 \\ I_2 \\ \vdots \\ I_N \end{bmatrix} \quad (2.28)$$

where ω is the angular frequency of the voltages and currents and $V_1 \dots V_N$ and $I_1 \dots I_N$ are the complex (frequency-domain) phasor representations of their respective real (time-domain) voltages and currents.

2.1.3.3.1 Energy considerations and the magnetic coupling coefficient

Consider the two coupled inductors with inductances L_1 and L_2 in Figure 2.4. From (2.27)

$$\begin{aligned} v_1 &= L_1 \frac{di_1}{dt} + M \frac{di_2}{dt} \\ 0 &= M \frac{di_1}{dt} + L_2 \frac{di_2}{dt} \end{aligned} \quad (2.29)$$

Solving for v_1 in terms of i_1 :

$$v_1 = \frac{L_1 L_2 - M^2}{L_2} \frac{di_1}{dt} \quad (2.30)$$

Then the energy stored in the magnetic fields is given by

$$E = \int_{t_1}^{t_2} v_1 i_1 dt = \int_{i_1(t_1)}^{i_1(t_2)} \frac{L_1 L_2 - M^2}{L_2} \frac{di_1}{dt} i_1 dt = \frac{1}{2} \frac{L_1 L_2 - M^2}{L_2} i_1^2 \quad (2.31)$$

where we set $i_1(t_1) = 0$. The expression in (2.31) must always be non-negative, i.e., $E \geq 0$. The only way this inequality can be satisfied is if [22]

$$M \leq \sqrt{L_1 L_2} \quad (2.32)$$

Eq. (2.32) sets the upper limit on M , such that M can be expressed as

$$M = k \sqrt{L_1 L_2} \quad (2.33)$$

where k is called the magnetic coupling coefficient subject to $0 \leq k \leq 1$ and it represents the fraction of magnetic flux that links the two coils.

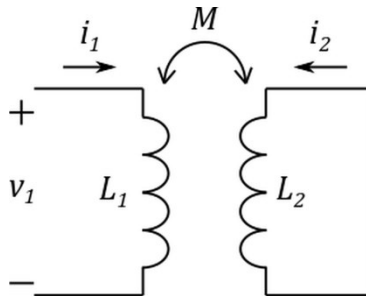


Figure 2.4 Coupled inductors with a short-circuited secondary.

2.2 RESONANT INDUCTIVE WPT

2.2.1 POWER GAIN DEFINITIONS

Consider the circuit in Figure 2.5 where the black-box two-port network is characterized by its S-parameters. Three power gains can be defined [3]:

- Power gain: the ratio of the power consumed by the load to the power input to the network.

$$G = \frac{P_L}{P_{in}} = \frac{|S_{21}|^2(1 - |\Gamma_L|^2)}{(1 - |\Gamma_{in}|^2)|1 - S_{22}\Gamma_L|^2} \quad (2.34)$$

- Available power gain: the ratio of the maximum available power from the network to the maximum available power from the source. The maximum available power from the source occurs when the source and the input to the network are conjugately matched, and the maximum available power from the network occurs when the load and the output of the network are conjugately matched.

$$G_A = \frac{P_{avn}}{P_{avs}} = \frac{|S_{21}|^2(1 - |\Gamma_S|^2)}{|1 - S_{11}\Gamma_S|^2(1 - |\Gamma_{out}|^2)} \quad (2.35)$$

- Transducer power gain: the ratio of the power consumed by the load to the maximum available power from the source.

$$G_T = \frac{P_L}{P_{avs}} = \frac{|S_{21}|^2(1 - |\Gamma_S|^2)(1 - |\Gamma_L|^2)}{|1 - \Gamma_S\Gamma_{in}|^2|1 - S_{22}\Gamma_L|^2} \quad (2.36)$$

The reflection coefficient Γ is defined as

$$\Gamma = \frac{Z - Z_R^*}{Z + Z_R} \quad (2.37)$$

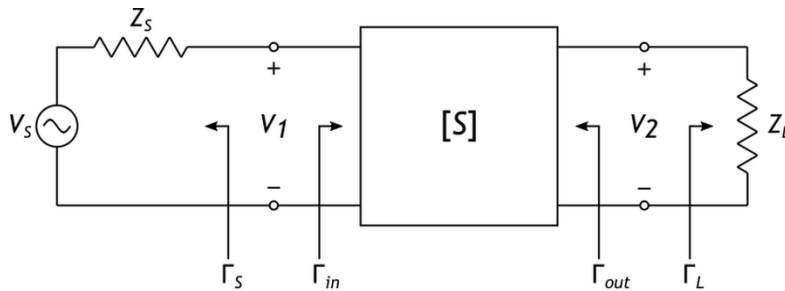


Figure 2.5 Generalized two-port network.

where Z is the impedance of interest and Z_R is a reference impedance (which in the case of a transmission line is simply its characteristic impedance Z_0). However, if there are no transmission lines (i.e., the transmission line is electrically short), Z_R can be set arbitrarily. As a result, at the source $Z_R = Z_S^*$ and at the load $Z_R = Z_L^*$ so that $\Gamma_S = \Gamma_L = 0$. Hence (2.34)-(2.36) simplify to

$$G = \frac{|S_{21}|^2}{(1 - |\Gamma_{in}|^2)} \quad (2.38)$$

$$G_A = \frac{|S_{21}|^2}{(1 - |\Gamma_{out}|^2)} \quad (2.39)$$

$$G_T = |S_{21}|^2 \quad (2.40)$$

Hence, the transducer gain will also be referred to as the S_{21} parameter.

Another useful relation is that for S_{21} [23]

$$S_{21} = 2 \frac{V_L}{V_S} \sqrt{\frac{Z_S}{Z_L}} \quad (2.41)$$

For the remainder of this thesis, only the power gain G and the transducer gain $G_T = |S_{21}|^2$ will be of interest as they are most commonly used in literature.

2.2.2 NON-RESONANT INDUCTIVE WPT

The most basic inductive WPT circuit is shown in Figure 2.6. The available power from the source and the input and output powers are given by

$$P_{avs} = \frac{|V_S|^2}{8R_S} \quad (2.42)$$

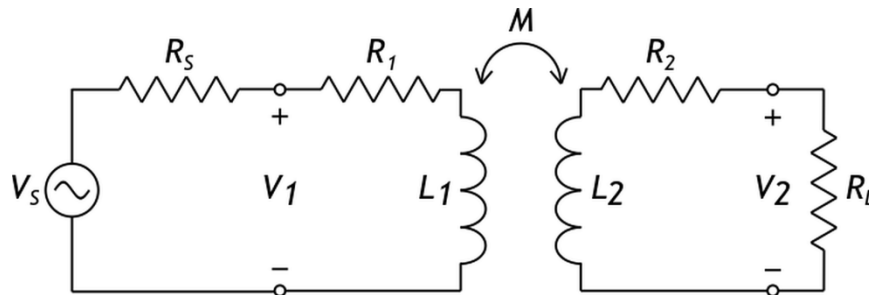


Figure 2.6 Basic configuration for inductive WPT.

$$P_{in} = \frac{|V_S|^2}{2|\hat{Z}_1\hat{Z}_2 + \omega^2 M^2|^2} \left(\text{Re}\{Z_1\}|\hat{Z}_2|^2 + \omega^2 M^2 \text{Re}\{\hat{Z}_2\} \right) \quad (2.43)$$

$$P_L = \frac{|V_S|^2 \omega^2 M^2 R_L}{2|\hat{Z}_1\hat{Z}_2 + \omega^2 M^2|^2} \quad (2.44)$$

where $Z_1 = R_1 + j\omega L_1$, $\hat{Z}_1 = R_S + Z_1$, $Z_2 = R_2 + j\omega L_2$, and $\hat{Z}_2 = R_L + Z_2$. The power gain is obtained by substituting (2.43) and (2.44) into (2.34)

$$G = \frac{\omega^2 M^2 R_L}{\text{Re}\{Z_1\}|\hat{Z}_2|^2 + \omega^2 M^2 \text{Re}\{\hat{Z}_2\}} \quad (2.45)$$

and the transducer gain is obtained by substituting (2.42) and (2.44) into (2.36)

$$G_T = |S_{21}|^2 = \frac{4\omega^2 M^2 R_S R_L}{|\hat{Z}_1\hat{Z}_2 + \omega^2 M^2|^2} \quad (2.46)$$

It is easy to show that (2.45) and (2.46) do not attain a local maximum with respect to either ω or M (as in Figure 2.7). Thus, we can increase the power gain and the output power only by increasing either the frequency or the magnetic coupling. As was discussed in Section 2.1.3.3.1 and given by (2.33), M reaches its maximum when $k = 1$, which physically means that the two inductors are perfectly coupled.

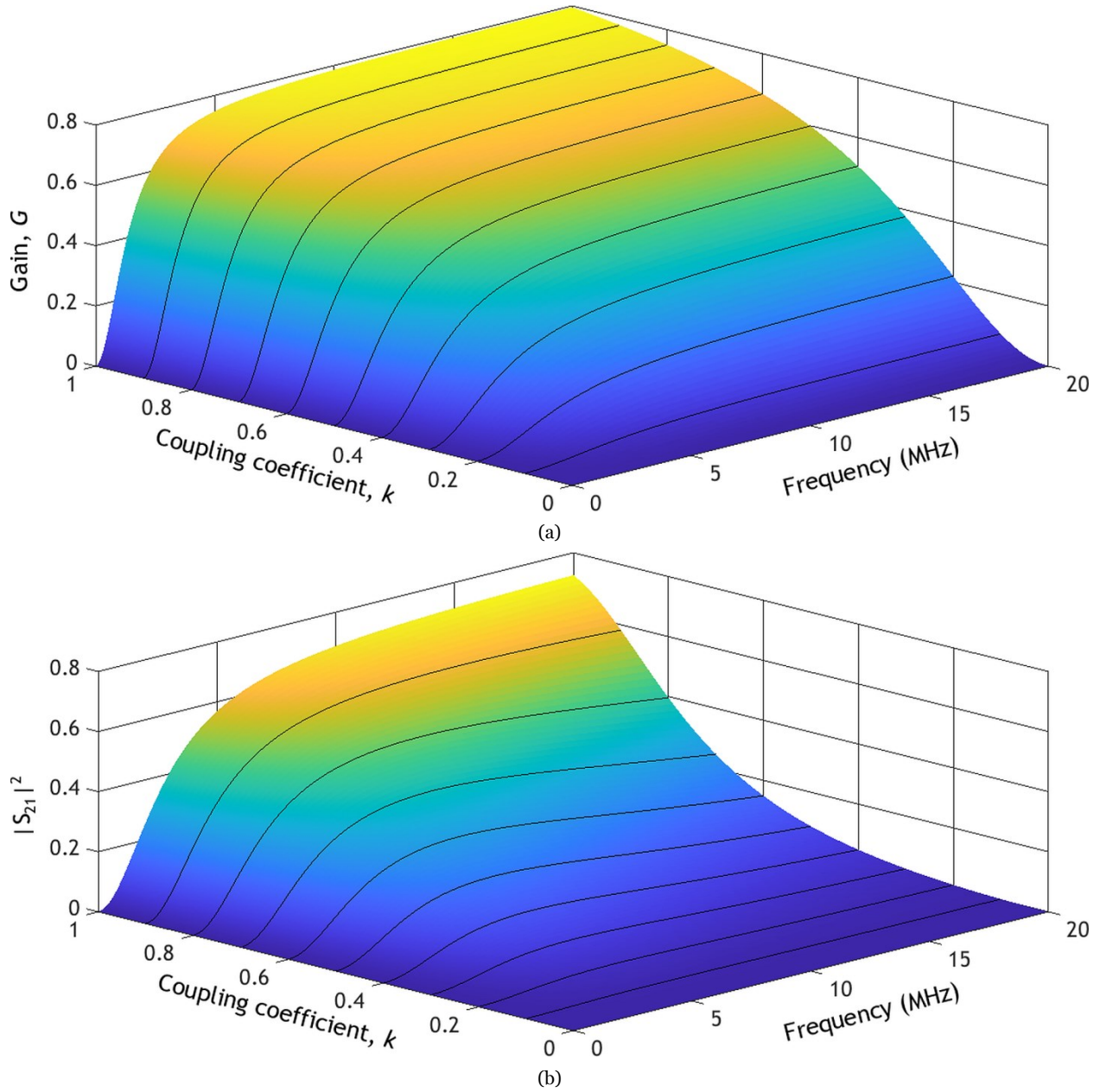


Figure 2.7 Power gain and $|S_{21}|^2$ plots for $R_s = R_L = 50 \Omega$, $R_1 = 3 \Omega$, $R_2 = 6 \Omega$, $L_1 = 1 \mu\text{H}$, and $L_2 = 2.2 \mu\text{H}$

While attaining $k = 1$ is practically impossible, it is possible to attain high coupling by wrapping both inductors around the same magnetic core. The high magnetic permeability μ of the magnetic core prevents most of the magnetic field from escaping as given by [3]

$$\Gamma_{\parallel} = \frac{\eta_2 \cos \theta_2 - \eta_1 \cos \theta_1}{\eta_2 \cos \theta_2 + \eta_1 \cos \theta_1} \quad (2.47)$$

$$\Gamma_{\perp} = \frac{\eta_2 \cos \theta_1 - \eta_1 \cos \theta_2}{\eta_2 \cos \theta_1 + \eta_1 \cos \theta_2}$$

where Γ_{\parallel} and Γ_{\perp} are the reflection coefficients for parallel and perpendicular electromagnetic field polarizations, respectively, θ_1 and θ_2 are the angles of incidence and transmission, respectively, at the interface between two materials, and η_1 and η_2 are the intrinsic medium impedances given by

$$\eta = \sqrt{\frac{\mu}{\epsilon}} \quad (2.48)$$

Let the first medium be the magnetic core and the second medium be free space. Substituting (2.48) into any equation in (2.47) and letting the magnetic core permeability grow without bound, we get

$$\Gamma \rightarrow -1 \text{ as } \mu \rightarrow \infty \quad (2.49)$$

where the subscript on Γ was omitted because the result is identical for both polarizations. The above result demonstrates that most of the fields incident on the magnetic core-air interface reflect back into the magnetic core and are therefore contained within it, resulting in high magnetic coupling. This is how electric transformers maintain high power transfer (large $|S_{21}|^2$) and high power gain (large G).

2.2.3 MAGNETIC RESONANCE WPT

2.2.3.1 2-resonator system

Now consider the compensated circuit in Figure 2.8. The expression for transducer gain in (2.46) can be rewritten as

$$|S_{21}|^2 = \frac{4\omega^2 M^2 R_S R_L}{[(R_1 + R_S)(R_2 + R_L) - X_1 X_2 + \omega^2 M^2]^2 + [(R_1 + R_S)X_2 + (R_2 + R_L)X_1]^2} \quad (2.50)$$

where X_1 and X_2 are the total reactances of each of the coupled circuits. By differentiating (2.50) with respect to X_1 and X_2 , it is possible to find values for the reactances that produce the maximum output power, which results in

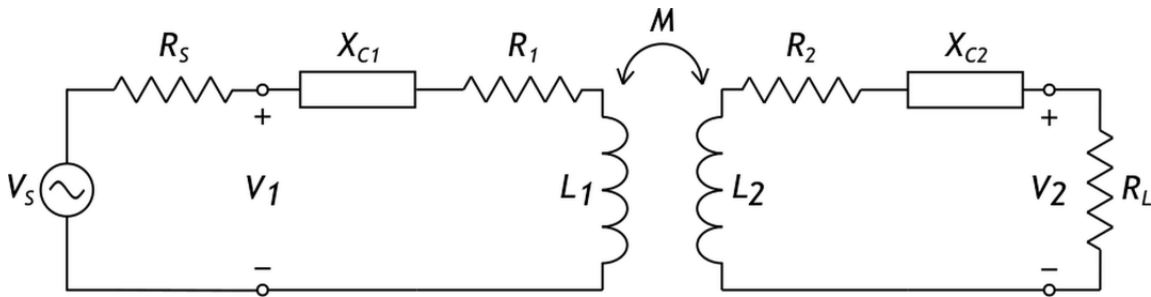


Figure 2.8 Compensated inductive WPT circuit.

$$(X_1, X_2) = \begin{cases} (0,0) & , \omega^2 M^2 - \hat{R}_1 \hat{R}_2 < 0 \\ \left(\sqrt{\frac{\hat{R}_1}{\hat{R}_2} (\omega^2 M^2 - \hat{R}_1 \hat{R}_2)}, \sqrt{\frac{\hat{R}_2}{\hat{R}_1} (\omega^2 M^2 - \hat{R}_1 \hat{R}_2)} \right) & , \omega^2 M^2 - \hat{R}_1 \hat{R}_2 > 0 \\ \left(-\sqrt{\frac{\hat{R}_1}{\hat{R}_2} (\omega^2 M^2 - \hat{R}_1 \hat{R}_2)}, -\sqrt{\frac{\hat{R}_2}{\hat{R}_1} (\omega^2 M^2 - \hat{R}_1 \hat{R}_2)} \right) & , \omega^2 M^2 - \hat{R}_1 \hat{R}_2 > 0 \end{cases} \quad (2.51)$$

where $\hat{R}_1 = R_S + R_1$ and $\hat{R}_2 = R_L + R_2$. The conditions associated with each case can be derived from the second derivate test for maxima and minima of multivariate functions, which states that for a function $f(x, y)$ to have local maxima and minima, $\frac{\partial^2 f}{\partial x^2} \frac{\partial^2 f}{\partial y^2} - \left(\frac{\partial^2 f}{\partial x \partial y} \right)^2 > 0$ must be satisfied at the critical values of $f(x, y)$. The first case on the RHS of (2.51) says that in the under coupled condition (i.e., $\omega_0^2 M^2 - \hat{R}_1 \hat{R}_2 < 0$), maximum power transfer may be achieved when both coupled circuits are resonant, i.e., each of the inductors is compensated with a capacitor to cancel its reactance and both resonate at the same frequency ω_0 . The second and third cases say that in the over coupled condition (i.e., $\omega_0^2 M^2 - \hat{R}_1 \hat{R}_2 > 0$), maximum power transfer may be achieved when the total reactances are either both inductive or both capacitive (i.e., the compensation capacitors' influence causes the overall reactances to become capacitive). And in the critically coupled condition (i.e., $\omega_0^2 M^2 - \hat{R}_1 \hat{R}_2 = 0$), (2.51) states that maximum power transfer may be attained when the reactances are zero, as well. Thus, the critical coupling condition attains the maximum transducer gain of

$$|S_{21}|_{max}^2 = \frac{R_S R_L}{\hat{R}_1 \hat{R}_2} = \frac{R_S R_L}{(R_1 + R_S)(R_2 + R_L)} \quad (2.52)$$

It is worth noting that in the over coupled condition [second and third cases in (2.51)] the maximum transducer gain of (2.52) is attained when $\hat{R}_1 = \hat{R}_2 = \hat{R}$ and $X_1 = X_2 = X$ (but in general may produce lower values as shown in Figure 2.9).

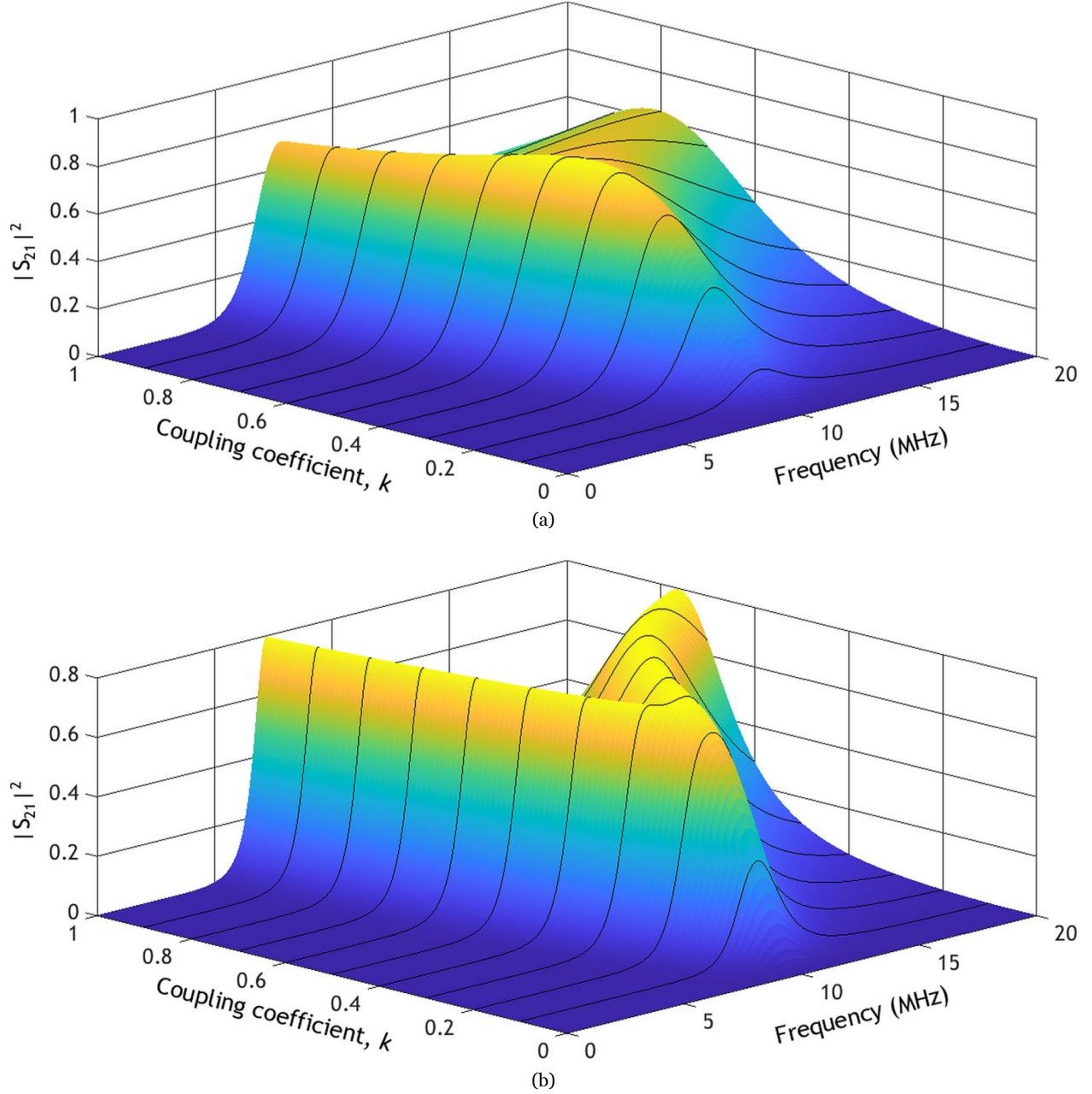


Figure 2.9 $|S_{21}|^2$ plots for (a) $R_S = R_L = 50 \Omega$, $R_1 = 3 \Omega$, $R_2 = 6 \Omega$, $L_1 = 1 \mu\text{H}$, $L_2 = 3.3 \mu\text{H}$, $C_1 = 253 \text{ pF}$, and $C_2 = 77 \text{ pF}$ and (b) $R_S = R_L = 50 \Omega$, $R_1 = R_2 = 6 \Omega$, $L_1 = L_2 = 3.3 \mu\text{H}$, and $C_1 = C_2 = 77 \text{ pF}$.

Now, let us compare the transducer gains for inductive and resonant WPT. Taking the derivative of (2.46) with respect to frequency and equating to zero, it can be found that maximum transducer gain for inductive WPT is achieved at the frequency

$$\omega_c = \sqrt{\frac{\hat{R}_1 \hat{R}_2}{L_1 L_2 - M^2}} \quad (2.53)$$

and the maximum transducer gain is

$$|S_{21,I-WPT}|^2 \Big|_{\omega=\omega_c} = \frac{4M^2 R_S R_L}{(\hat{R}_1 L_2 + \hat{R}_2 L_1)^2} \quad (2.54)$$

The first thing to note about this is that maximum output power can only be extracted when there is 100% coupling between the two inductors, as noted earlier. The second thing to note is that the output power of inductive WPT is always less than or equal to the output power of resonant WPT. This can be verified by subtracting (2.54) from (2.52) as follows:

$$\frac{R_S R_L}{\hat{R}_1 \hat{R}_2} - \frac{4M^2 R_S R_L}{(\hat{R}_1 L_2 + \hat{R}_2 L_1)^2} \geq 0 \quad (2.55)$$

Manipulating the inequality

$$(\hat{R}_1 L_2 + \hat{R}_2 L_1)^2 - 4\hat{R}_1 \hat{R}_2 M^2 \geq 0 \quad (2.56)$$

The LHS is minimized when $M = \sqrt{L_1 L_2}$, producing

$$(\hat{R}_1 L_2 - \hat{R}_2 L_1)^2 \geq 0 \quad (2.57)$$

which is true for all values of \hat{R}_1 , \hat{R}_2 , L_1 , and L_2 . In fact, the only time both WPT schemes produce the same output power is when $(\hat{R}_1 L_2 - \hat{R}_2 L_1)^2 = 0$ and $k = 1$.

It was shown that for inductive WPT, maximum power transfer is achieved when $k = 1$, which is impractical. For resonant WPT at resonance, the maximum transducer gain as a function of mutual inductance M is

$$|S_{21}(M)|^2 \Big|_{\omega=\omega_0} = \frac{4\omega_0^2 M^2 R_S R_L}{(\hat{R}_1 \hat{R}_2 + \omega_0^2 M^2)^2} \quad (2.58)$$

and in terms of the coupling coefficient

$$|S_{21}(k)|^2 \Big|_{\omega=\omega_0} = \frac{\hat{Q}_1}{Q_S} \frac{4k^2 \hat{Q}_1 \hat{Q}_2}{(1 + k^2 \hat{Q}_1 \hat{Q}_2)^2} \frac{\hat{Q}_2}{Q_L} \quad (2.59)$$

where $\hat{Q}_1 = \omega_0 L_1 / \hat{R}_1$ and $\hat{Q}_2 = \omega_0 L_2 / \hat{R}_2$ are the loaded quality factors (Q factors) of the resonators, and $Q_S = \omega_0 L_1 / R_S$ and $Q_L = \omega_0 L_2 / R_L$ are the external Q factors of the resonators. To achieve the maximum transducer gain specified by (2.52), the following condition must be met

$$M_{critical} = \frac{\sqrt{\hat{R}_1 \hat{R}_2}}{\omega_0} \quad (2.60)$$

or in terms of the coupling coefficient

$$k_{critical} = \frac{1}{\sqrt{\hat{Q}_1 \hat{Q}_2}} \quad (2.61)$$

The important conclusion to draw from this is that coupling does not need to be 100% anymore in order to achieve maximum output power. For example, when $\hat{R}_1 = \hat{R}_2 = 50 \Omega$, $L_1 = L_2 = 10 \mu\text{H}$, and $\omega_0 = 2\pi \times 10 \text{ MHz}$, we need a mutual inductance of $M = 796 \text{ nH}$, which corresponds to a coupling of only $k = 0.080$, which is very small. This ability to transfer large amounts of power (larger than those achievable by inductive WPT) with small coupling coefficients is the greatest benefit of resonant WPT as it enables high power transfer over larger distances or alternatively, for a wider range of orientations between the two inductors.

Next, the power gain G in (2.45) for inductive WPT can be re-written for resonant WPT as

$$G = \frac{\omega^2 M^2 R_L}{R_1 |\hat{R}_2 + jX_2|^2 + \omega^2 M^2 \hat{R}_2} \quad (2.62)$$

where it is clear that it is not dependent on the resonant characteristics of the source resonator and that the only influence that the source resonator has on G is through the inductor's resistance R_1 and mutual inductance M .

By differentiating (2.62) with respect to ω and equating to zero, maximum power gain is attained when

$$\omega = \sqrt{\frac{2}{2L_2 C_2 - (\hat{R}_2 C_2)^2}} \quad (2.63)$$

It is evident from (2.63) and Figure 2.10 that, unlike the transducer gain $|S_{21}|^2$, power gain attains a maximum at a single frequency independent of M . As well, from (2.62) and Figure 2.10, it is easy to determine that maximum power gain continues to increase with increasing M .

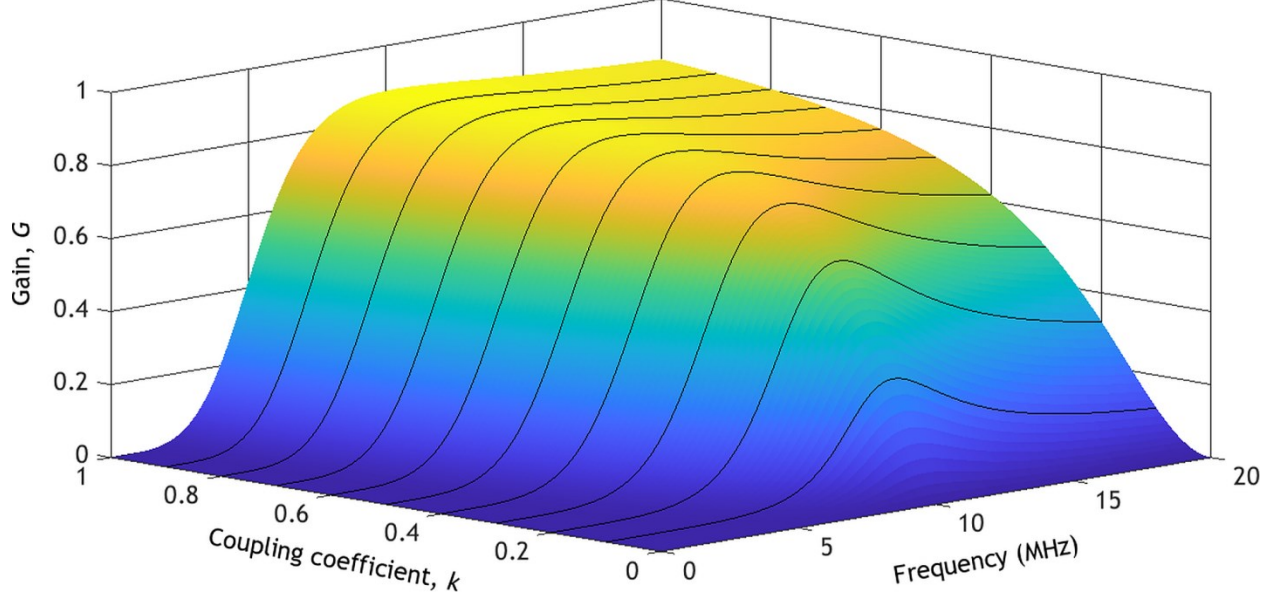


Figure 2.10 Power gain for magnetic resonance WPT with $R_S = R_L = 50 \Omega$, $R_1 = 3 \Omega$, $R_2 = 6 \Omega$, $L_1 = 1 \mu\text{H}$, $L_2 = 2.2 \mu\text{H}$, $C_1 = 253 \text{ pF}$, and $C_2 = 115 \text{ pF}$.

2.2.3.2 3-resonator system

Consider the circuit in Figure 2.11 consisting of a source resonator, a relay resonator, and a load resonator, where all the resonators have the same resonant frequency (i.e., $L_1 C_1 = L_2 C_2 = L_3 C_3 = 1/\omega_0^2$). It was seen in the 2-coil case that maximum power can be transferred when the individual resonators are operated at the resonant frequency. When all three coils are resonant, the transducer gain is given by [24]

$$\begin{aligned}
 |S_{21,3-res}|^2 &= \frac{4R_S R_L (\omega_0^4 M_{12}^2 M_{23}^2 + \omega_0^2 M_{13}^2 R_2^2)}{(\hat{R}_1 R_2 \hat{R}_3 + \omega_0^2 M_{12}^2 \hat{R}_3 + \omega_0^2 M_{23}^2 \hat{R}_1 + \omega_0^2 M_{13}^2 R_2)^2 + 4\omega_0^6 M_{12}^2 M_{23}^2 M_{13}^2} \\
 &= \frac{\hat{Q}_1}{Q_S} \frac{4(k_{12}^2 k_{23}^2 \hat{Q}_1 Q_2^2 \hat{Q}_3 + k_{13}^2 \hat{Q}_1 \hat{Q}_3)}{(1 + k_{12}^2 \hat{Q}_1 Q_2 + k_{23}^2 Q_2 \hat{Q}_3 + k_{13}^2 \hat{Q}_1 \hat{Q}_3)^2 + 4k_{12}^2 k_{23}^2 k_{13}^2 \hat{Q}_1^2 Q_2^2 \hat{Q}_3^2} \frac{\hat{Q}_3}{Q_L}
 \end{aligned} \tag{2.64}$$

For fixed resonator parameters (i.e., R , L , and C), the maximum power transfer is found by differentiating (2.64) with respect to k_{12} and k_{23} (or M_{12} and M_{23}) and equating to zero to produce the condition

$$k_{12}^2 \hat{Q}_1 = k_{23}^2 \hat{Q}_3 \quad \text{or} \quad M_{12}^2 \hat{R}_1 = M_{23}^2 \hat{R}_3 \tag{2.65}$$

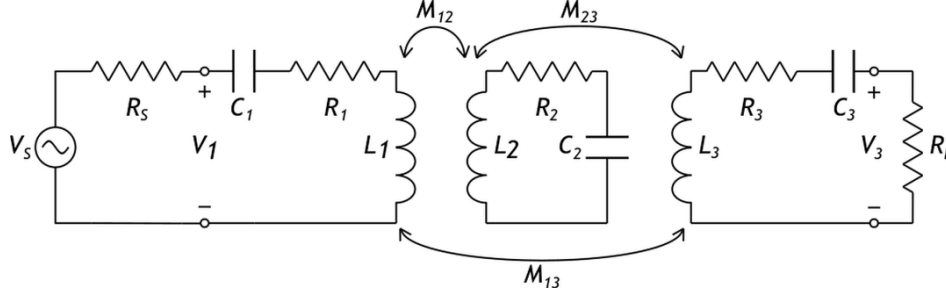


Figure 2.11 3-resonator WPT circuit.

Substituting (2.65) into (2.64) produces

$$|S_{21,3-res}|_{max}^2 = 4 \frac{\hat{Q}_1}{Q_S} \frac{k_{12}^4 \hat{Q}_1^2 Q_2^2 + k_{13}^2 \hat{Q}_1 \hat{Q}_3}{(1 + 2k_{12}^2 \hat{Q}_1 Q_2 + k_{13}^2 \hat{Q}_1 \hat{Q}_3)^2 + 4k_{12}^4 k_{13}^2 \hat{Q}_1^3 Q_2^2 \hat{Q}_3} \frac{\hat{Q}_3}{Q_L} \quad (2.66)$$

If the 3-resonator system is converted into a 2-resonator system by removing the relay resonator in the middle ($k_{12} = k_{23} = 0$), the maximum transducer gain [obtained by differentiating (2.64) with respect to k_{13}] will be

$$|S_{21,2-res}|_{max}^2 = \frac{\hat{Q}_1 \hat{Q}_3}{Q_S Q_L} \quad (2.67)$$

which is identical to (2.52), as expected. It can be determined from (2.66) and (2.67) that a 2-resonator system is capable of transferring more power than a 3-resonator system. $|S_{21,3-res}|_{max}^2$ will approach $|S_{21,2-res}|_{max}^2$ when $k_{12}^2 \hat{Q}_1 Q_2 \gg 1$ and $k_{13} \ll 1$ (i.e., non-adjacent coupling is negligible as in [25], [26]), thereby emphasizing the importance of large Q factors. However, the benefits of the 3-resonator system over the 2-resonator system are its ability to transfer more power for a range of loads and the extension of WPT distance. Consider the condition for maximum power transfer for the 2-resonator and 3-resonator systems with $R_1 = R_2 = R_3 = 0$, $R_S = 50 \Omega$, and $f_0 = 10$ MHz shown in Table I. It is possible to see that the total distance in the 3-resonator system can be set arbitrarily, whereas the distance between the coils in the 2-resonators system is fixed. Moreover, because maximum power transfer in the 3-resonator system depends on the ratio of mutual inductances, a wider range of loads can be matched to the source. It can be observed in Figure 2.12 that the range of loads afforded to the 3-resonator system dwarfs the one available to the 2-resonator system. In fact, [24] showed that if $k_{13} < \frac{1}{\sqrt{3\hat{Q}_1\hat{Q}_3}} = \frac{k_{13,critical}}{\sqrt{3}}$ [where $k_{13,critical}$ is given by (2.61)], the 3-resonator configuration performs better than the 2-resonator one.

Table I Comparison of 2-resonator and 3-resonator systems

	Case 1 ($R_L < R_S$)	Case 2 ($R_L > R_S$)
Load	$R_L = 10 \Omega$	$R_L = 250 \Omega$
2-resonator M (2.60)	$M_{13} = 356 \text{ nH}$	$M_{13} = 1.78 \text{ }\mu\text{H}$
3-resonator M (2.65)	$M_{12} = 2.24 M_{23}$ ($d_{12} \approx 0.76 d_{23}^1$)	$M_{12} = 0.45 M_{23}$ ($d_{12} \approx 1.30 d_{23}^1$)

¹Mutual inductance is approximately proportional to the inverse cubed distance between two coils, d .

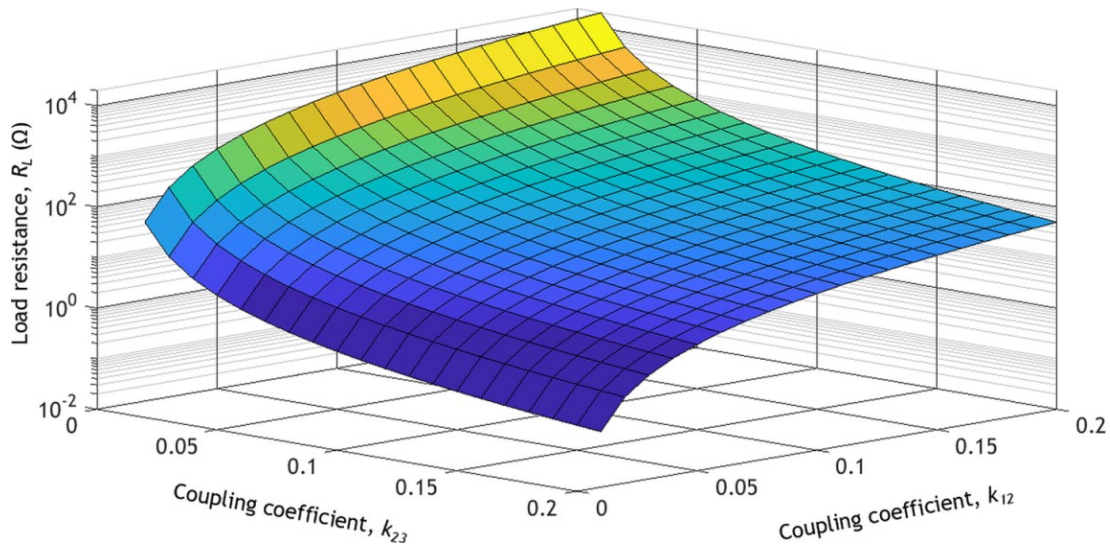
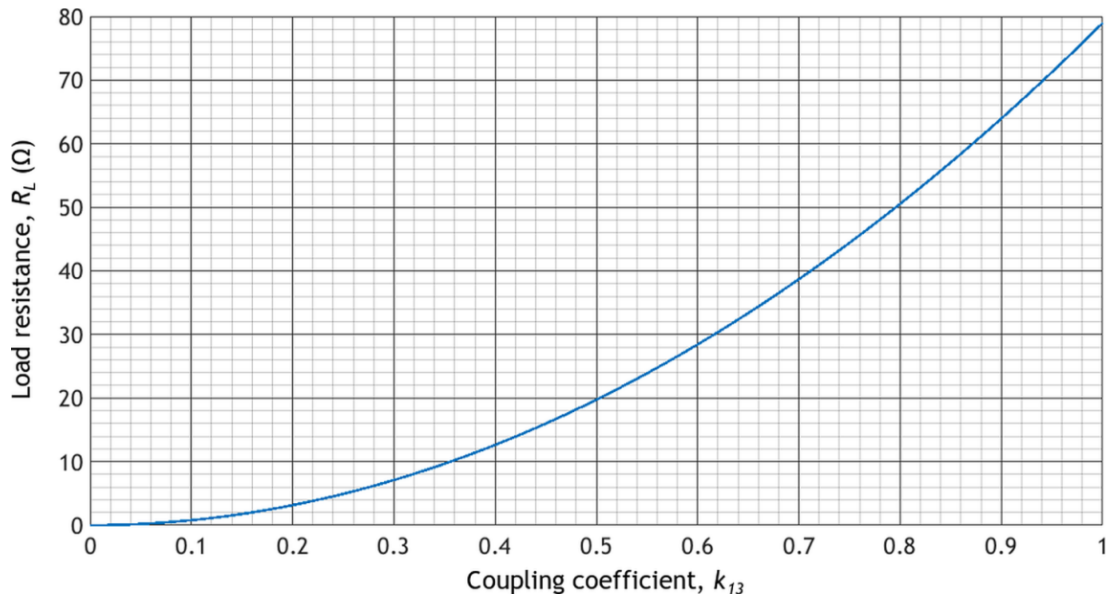


Figure 2.12 Range of load impedances available to 2- and 3-resonator systems with $\hat{R}_1 = 50 \Omega$ and $L_1 = L_2 = L_3 = 1 \mu\text{H}$ at a resonant frequency of $f_0 = 10 \text{ MHz}$

Assuming that $k_{13} \ll 1$, the power gain is given by [26]

$$G = \frac{k_{12}^2 k_{23}^2 Q_1 Q_2^2 \hat{Q}_3}{(1 + k_{12}^2 Q_1 Q_2 + k_{23}^2 Q_2 \hat{Q}_3)(1 + k_{23}^2 Q_2 \hat{Q}_3)} \frac{\hat{Q}_3}{Q_L} \quad (2.68)$$

It was shown above that $|S_{21,3-res}|^2$ maximizes with respect to both k_{12} and k_{23} , but observe that (2.68) maximizes only with respect to k_{23} . Thus, it is possible to optimize the coupling between the second and third coils for maximum power gain and then further optimize the coupling between the first and second coils to obtain maximum $|S_{21,3-res}|^2$ subject to the maximum power gain condition. It was shown in [25], [26] that the 3-resonator system can achieve relatively high power gains and output powers simultaneously, whereas the 2- and 4-resonator systems can attain a maximum in one parameter to the detriment of the other.

2.2.3.3 Frequency splitting

Revisiting the 2-resonator system, equations (2.60) and (2.61) describe the critical coupling condition $\omega_0^2 M^2 - \hat{R}_1 \hat{R}_2 = 0$. When $M < M_{critical}$, the resonators are under coupled and maximum power transfer can only be attained when both coupled resonators are operated at resonance ω_0 , as described by the first case in (2.51). When $M > M_{critical}$, the resonators are said to be over coupled and (2.51) states that there are two reactance values for each resonator that produce maximum power transfer. In other words, there are two frequencies at which maximum power transfer is achieved [23], [27], [28]. This phenomenon is known as frequency splitting.

In the special case of symmetric resonators (i.e., $\hat{R}_1 = \hat{R}_2 = \hat{R}$ and $X_1 = X_2 = X$), differentiating (2.50) with respect to frequency and equating to zero will give us the frequencies that produce the maxima and minima of the transducer gain

$$\frac{\partial}{\partial \omega} |S_{21}|^2 = \frac{-8\omega M^2 R_S R_L (\omega^2 M^2 - \hat{R}^2 - X^2)(\omega^2 M^2 + \hat{R}^2 - 2\omega X X' + X^2)}{[(R^2 - X^2 + \omega^2 M^2)^2 + 4R^2 X^2]^2} = 0 \quad (2.69)$$

where $X = \omega_0 L \left(\frac{\omega}{\omega_0} - \frac{\omega_0}{\omega} \right)$ and $X' = \partial X / \partial \omega$. Then the locations of the minima and maxima are given by

$$\omega_{min}^2 M^2 + \hat{R}^2 - 2\omega_{min} X X' + X^2 = 0 \quad (2.70)$$

$$\omega_{max}^2 M^2 - \hat{R}^2 - X^2 = 0 \quad (2.71)$$

Solving (2.70) and (2.71) for the frequencies produces

$$f_{min} = f_0 \sqrt{\frac{1}{2(1-k^2)} \left[-(2 - \hat{Q}^{-2}) + \sqrt{(2 - \hat{Q}^{-2})^2 + 12(1 - k^2)} \right]} \quad (2.72)$$

$$f_{max} = f_0 \sqrt{\frac{1}{2(1-k^2)} \left[(2 - \hat{Q}^{-2}) \pm \sqrt{(2 - \hat{Q}^{-2})^2 - 4(1 - k^2)} \right]} \quad (2.73)$$

where $\hat{Q} = \hat{Q}_1 = \hat{Q}_2$.

Examining (2.73), frequency splitting occurs when the discriminant $(2 - \hat{Q}^{-2})^2 - 4(1 - k^2) = 0$ and the coupling coefficient at which this occurs is

$$k_{split} = \frac{1}{\hat{Q}} \sqrt{1 - \frac{1}{4\hat{Q}^2}} \quad (2.74)$$

Note that when $\hat{Q} \gg 1$, $k_{split} \approx k_{critical}$ and the two split frequencies are

$$f_e \approx \frac{f_0}{\sqrt{1+k}} \quad (2.75)$$

$$f_o \approx \frac{f_0}{\sqrt{1-k}} \quad (2.76)$$

where the subscripts stand for even and odd and represent the resonant frequencies when even and odd excitation modes are applied to the circuit in Figure 2.13.

When an even mode is excited (i.e., $V_1 = V_2$), the circuit in Figure 2.13(a) can be represented by the half-circuit in Figure 2.13(b), which has a resonant frequency equal to (2.75). When an odd mode is excited (i.e., $V_1 = -V_2$), the circuit in Figure 2.13(a) can be represented by the half-circuit in Figure 2.13(c), which has a resonant frequency equal to (2.76) [29].

There are a few things to note from the above analysis: (a) While these approximations are valid only for $Q \gg 1$, they are useful because from (2.50), in order to achieve high power transfer and large distances, Q must be very large. (b) When the resonators are not symmetric, the analysis becomes very complicated and involves solving an 8th-order equation [28].

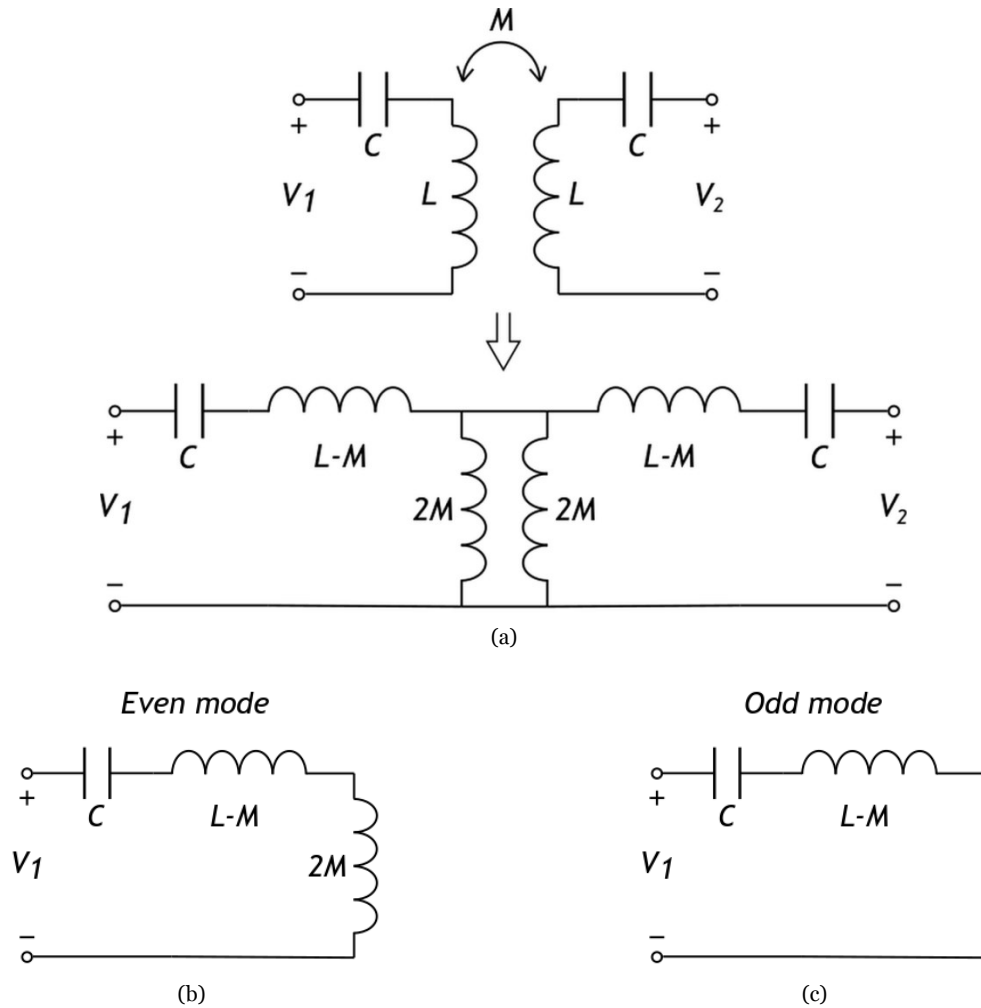


Figure 2.13 (a) Equivalent representation of a 2-resonator WPT circuit. (b) Even mode half circuit and (c) odd mode half circuit for the circuit in (a).

In general, an N -resonator system will have at most N resonant frequencies, which may deviate greatly from the resonant frequencies of the individual resonators. The factors that affect the system's resonant frequency include: the individual resonators' resonant frequency, the mutual coupling between all resonators, and the load impedances [30].

Chapter 3 The Sheath Helix and Single-Conductor Power Transmission

Power transmission is most commonly performed using two or more conductors and ordinarily thought of in terms of circuits that have a source and a ground. However, the transmission of electrical energy may also be performed by employing only a single conductor (without a ground) – as in the waveguide – or without a conductor whatsoever – as with antennas.

In 1899, Sommerfeld discussed the possibility of electromagnetic field propagation along a single straight, cylindrical conductor with a finite conductivity in the form of surface waves [31], [32]. However, propagation in this manner is not very practical because a large portion of the power extends to a distance much greater than the diameter of the conductor and thus, creates difficulties in launching the electromagnetic waves. Goubau continued the work and showed that the bulk of the power can be constrained to a small distance around the conductor either by modifying the surface of the conductor or by coating it with a dielectric [31], [32]. That made the launching and reception of the waves more practical by means of a coaxial cable whose outer conductor has been flared out in the shape of a horn. The advantage of the single-conductor transmission line is that it exhibits less loss than traditional two-conductor transmission lines. However, the “horn” launchers are still quite bulky, which makes the technology practical only at higher frequencies.

Another single-conductor medium of transmission is the helix (also known as the sheath helix), which was studied in 1898 by Pocklington [33]. The sheath helix may be regarded as a circular waveguide with fields both inside and outside it. Solutions to Maxwell’s equations for the sheath helix dictate that the fields outside it must be evanescent. Thus, power flows only along the surface of the helix and none flows radially outwards from it. Hence, the helix is a surface waveguide, too. Nikola Tesla experimented with such coils [5], [34] in order to transmit power wirelessly over great distances. As noted in [5], [32], [34], it is very straightforward to couple to and from the helix by way of a second inductively coupled coil (as in a transformer). This makes the sheath helix more practical than the Goubau transmission line at low frequencies.

3.1 RESONANT MODES ON THE SHEATH HELIX

As discussed in Section 2.1.3.1, the equation for inductance (2.8) is only an approximation that is valid when the inductor is electrically short (i.e., the AC current magnitudes are nearly uniform throughout the coil at all points in time). However, as the AC frequency is increased, the current distribution along the coil will become increasingly non-uniform. Moreover, in addition to the magnetic coupling between the individual windings of the coil, there is also stray capacitance between them (as shown in Figure 3.1). Thus, the coil will cease to behave purely as an inductor and will even attain self-resonance.

Due to the failure of the quasistatic model to accurately predict the behaviour of the coil at the high frequency regime, it is better to approach it from the point of view of propagating waves. Using this approach, the characteristic equation governing the behaviour of the helix in cylindrical coordinates is given by [35]

$$k^2 \frac{K_1(\tau\rho)I_1(\tau\rho)}{K_0(\tau\rho)I_0(\tau\rho)} = \tau^2 \tan^2 \psi \quad (3.1)$$

where k is the propagation constant in free space, I_0 and I_1 are the modified Bessel functions of the first kind, K_0 and K_1 are the modified Bessel functions of the second kind, ψ is the pitch angle of the helix, and τ is given by

$$\tau^2 = \beta^2 - k^2 \quad (3.2)$$

where β is the propagation constant of the fields of the helix. Two regimes arise from (3.1). A small number of turns per wavelength characterizes the first regime, whereby (3.1) can be approximated by [35]

$$k = \beta \sin \psi \quad (3.3)$$

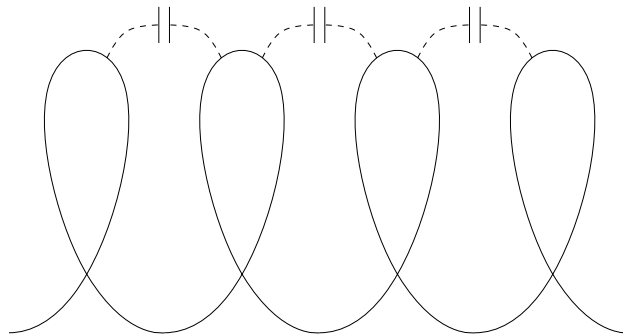


Figure 3.1 Stray capacitance between the windings of a coil.

from which it is possible to derive $v_p = c \sin \psi$. This result demonstrates that the helix acts to slow down the field propagation from the speed of light in free space c to v_p , thus reducing the free-space wavelength λ_0 . The other regime is characterized by a large number of turns per wavelength, and (3.1) is approximated by [35]

$$k = \frac{\beta}{\sqrt{1 + 160 \sqrt{\frac{r^6}{p^5 \lambda_0}}}} \quad (3.4)$$

where r and p are the radius and pitch of the helix, respectively. In this regime, the field propagation slows down even further. This regime governs the helices discussed in this thesis.

Although the sheath helix behaviour is better explained with propagating waves, it will be seen in Chapter 5 that for the special case of resonant sheath helices, the use of an equivalent lumped-element circuit is very beneficial in the design of single-conductor systems.

3.1.1 HALF-WAVE SHEATH HELIX

In 2007, Kurs et al. [8] presented their work on resonant inductive WPT in which they used four coils with two relay resonators, as illustrated in Figure 3.2. The relay resonators they used were helical coils with their ends left open-circuited. Even though the ends of the helix are open-circuited, current may still flow by forming a standing wave in the same manner that current flows on a dipole antenna [36].

Consider the helix in Figure 3.3, where the current at its ends must be zero. The helix has n turns, a radius r , and a pitch p between the turns. If the coil is electrically short (i.e., $2\pi r \ll \lambda$, where λ is the wavelength of the resonant mode) the current can be assumed to take on a sinusoidal distribution as described by [8], [35], [37]–[40]

$$I(z) = I_0 \cos\left(\frac{\pi}{l} z\right), \quad -l/2 \leq z \leq l/2 \quad (3.5)$$

where I_0 is the maximum current magnitude and $l = np$ is the length of the helix. Therefore, the helix is able to support a resonant mode, which has zero current and maximum voltage at its ends and maximum current and zero voltage at its centre – as in a dipole antenna. In this manner, the coil is able to transmit electromagnetic energy despite not having a return path (i.e., a ground).

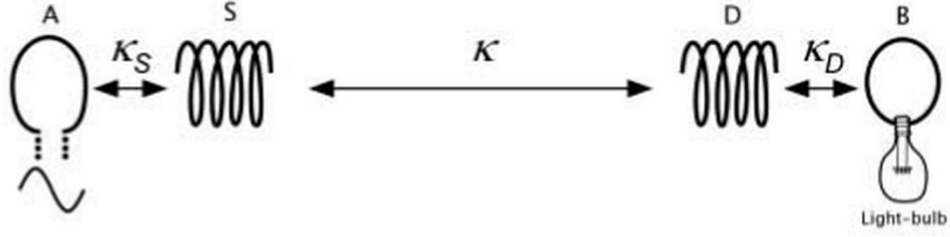


Figure 3.2 Four-coil system setup used by Kurs et al. [8] with two relay resonators.

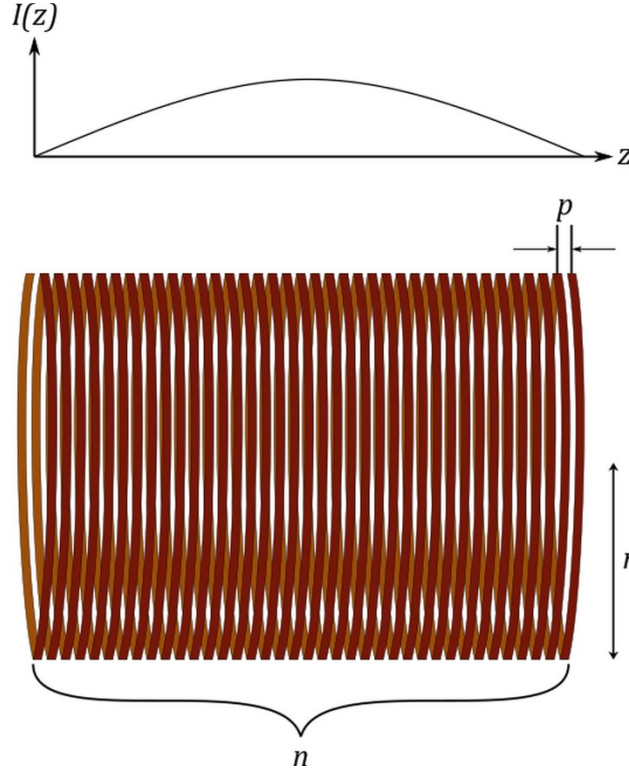


Figure 3.3 Half-wave sheath helix.

Using (3.4) and $l = np = 2\lambda_0$, the resonant frequencies supported by this coil are approximated by [39], [40]

$$f_0 = \frac{c}{13.26} \left(\frac{m^4 p}{r^6 n^4} \right)^{\frac{1}{5}}, \quad m = 1, 2, 3, \dots \quad (3.6)$$

where m indicates the number of half-wavelengths supported by the coil. However, because higher frequencies introduce extra modes of propagation, only the mode corresponding to $m = 1$ is of interest. Given that an open-circuited coil is able to resonate, it can be incorporated into the design of magnetic resonance WPT systems in place of the traditional LC resonators.

If the ends of the helix are instead connected to a source or a ground, the helix will behave like a half-wave transmission line with a low voltage/high current at the ends and a high voltage/low current at the midway point. Then the current profile will be given by

$$I(z) = I_0 \sin\left(\frac{\pi}{l}z\right), \quad -l/2 \leq z \leq l/2 \quad (3.7)$$

3.1.2 QUARTER-WAVE SHEATH HELIX

If one end of the helix is connected to ground (or a source) and the other remains open-circuited (as illustrated in Figure 3.4), the helix will be able to support quarter-wave resonances, with a high current/low voltage at the grounded end and a low current/high voltage at the open-circuited end. The current profile is described by

$$I(z) = I_0 \sin\left(\frac{\pi}{2l}z\right), \quad 0 \leq z \leq l \quad (3.8)$$

and the helix is reminiscent of the monopole antenna. Tesla coils [5], [34], [35] are a famous example of these.

Using (3.4) and $l = np = 4\lambda_0$, the quarter-wave resonant frequencies supported by these coils

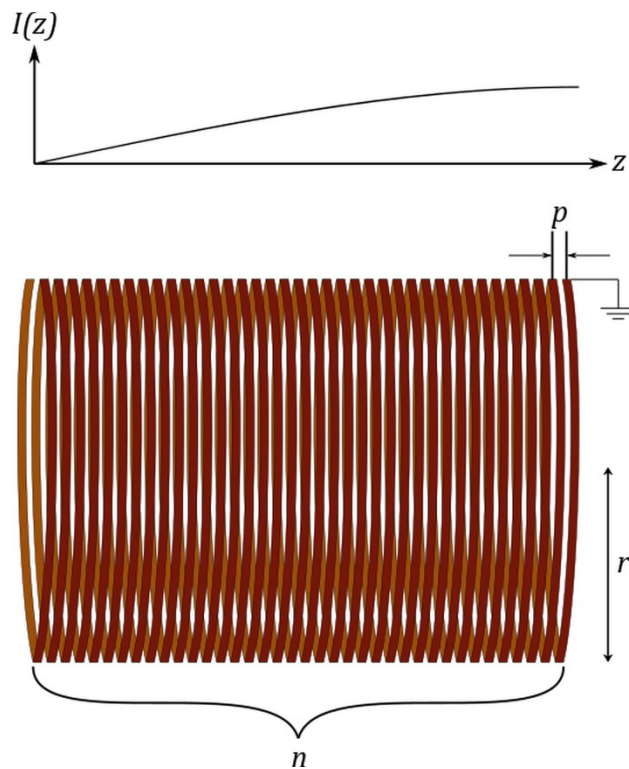


Figure 3.4 Quarter-wave sheath helix.

are approximated by [39], [40]

$$f_0 = \frac{c}{23.08} \left(\frac{m^4 p}{r^6 n^4} \right)^{\frac{1}{5}}, \quad m = 1, 3, 5, \dots \quad (3.9)$$

and again, only the $m = 1$ mode is considered to prevent the propagation of higher order modes.

Again, because these coils are resonant, they can be used in magnetic resonance WPT in place of lumped-element LC resonators. Quarter-wave sheath helices can be used as transmitters or receivers [37], [41]–[43] by connecting one end to a source or a load, respectively. In [43], a quarter-wave sheath helix was used as a transmitter, a half-wave coil was used as a relay, and an LC resonator was used as the receiver.

3.2 SHEATH HELICES IN SINGLE-CONDUCTOR WPT

Discussed above, quarter-wave sheath helices can be used as transmitters or receivers. However, they can also be used as relay coils [16], [18], [44], [45]. To be able to use quarter-wave sheath helices as relays, one end has to be grounded or alternatively connected to a large conductor.

[44], [45] discuss the possibility of using an arbitrarily shaped conductor to transmit energy. To achieve this, a quarter-wave helix is connected at one end to a conductor in order to couple energy into it, and a second quarter-wave helix is connected to it as well in order to couple energy out of it [shown in Figure 3.5(a)]. Care must be taken, as the size and shape of the conductor in the middle will affect the resonant frequency. As well, if the resistance of the conductor is large, the Q factor will be reduced – reducing the amount of power that makes it through to the other end of the system while broadening its bandwidth [3]. While a broader bandwidth is beneficial for communication purposes, the increased loss will reduce the SNR and increase the bit error rate (as will be demonstrated in the next chapter). Hence, care must also be taken to ensure that the conductor has low loss. For example, if the coils are connected by a mere wire then the wire must be electrically short at the desired frequency of operation so that the system is not detuned from its designed resonance frequency and the loss is kept low. The difference in operation between this single-conductor system and a Goubau line is that the latter sustains a propagating wave and, as a result, can be of any length, whereas quarter-wave helices operate in resonance and require the conductor between them to be electrically short.

In [16], [18], the conductive medium in the middle is replaced with two large capacitive plates [as in Figure 3.5(b)]. The additional capacitance shifts the resonant frequency. However, if the plates are made large enough, the large capacitance provides low impedance and does not significantly affect the resonant frequency. In other words, the large plate provides a large conductive surface for charges to flow on (i.e., a ground) and, due to electrostatic induction, induces charges to flow on the second plate and the second quarter-wave helix. In this situation, the large capacitance is akin to a short circuit and the two quarter-wave helices behave as a single half-wave helix. Thus, it is possible to transmit energy across a metallic barrier, which would normally be impossible via inductive or resonant WPT. This system configuration will be considered in the following chapters.

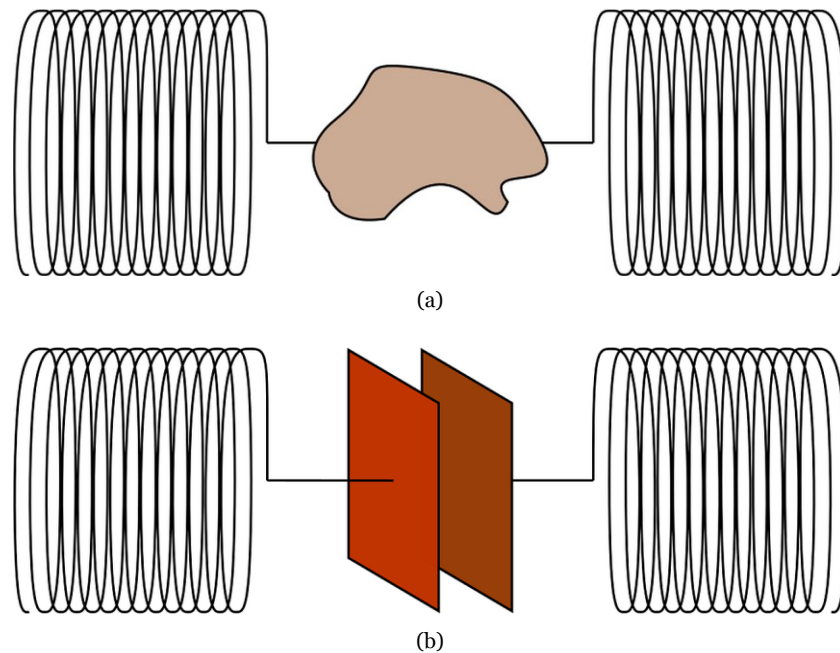


Figure 3.5 Coupling to and from (a) an arbitrarily shaped conductor and (b) a capacitive discontinuity using quarter-wave sheath helices.

Chapter 4 Communication for Wireless Power Transfer Systems

In Chapter 2, we have seen how power may be transmitted wirelessly via inductive coupling and enhanced by resonance, and the previous chapter introduced the sheath helix as a transmission medium that utilizes a single conductor. This chapter explores a resonant single-conductor system for the purposes of WPT and communication that utilizes sheath helices. The benefits of such a system include the reduction of systems from two wires to one, utilization of existing conductive infrastructure instead of dedicated transmission lines, and transmission to devices that are obstructed by conductive media such as buried sensors or biomedical implants. The applications of this technology could include the integration of a pipe for the transmission of power and data to underground sensors in a wellbore or the wireless charging of a device (e.g., cell phone) with a metallic encasing.

This chapter builds on concepts introduced in [16], [17], [44], [45]. As the aforementioned literature focuses on power transmission, this chapter's focus is on the data transfer performance of the single-conductor system. Specifically, it explores the ability of the system to be used with sensors that employ RFID and NFC communication protocols. In addition, a novel method for the improvement of asynchronous envelope detection is presented to assist in WIPT.

4.1 THE CHANNEL FREQUENCY RESPONSE AND MEASUREMENT SETUP

A channel's frequency response dictates its limits of communication such as the bandwidth of communication, maximum error-free data rate, frequencies of operation, and more. A channel whose frequency response is flat over the frequencies of interest is known as a flat channel and one that varies with frequency is known as frequency-selective. As can be expected, a frequency-selective channel is not desired since the variations in channel gain (i.e., $|S_{21}|$) alter the shape of the signal, which may introduce intersymbol interference (ISI, i.e., pulse shapes from past symbols that alter the pulse shapes of future symbols) and degrade performance.

Discussed in the last chapter, a WPT system may be constructed using quarter-wave sheath helices with a capacitive discontinuity to couple between them. It was shown in [16], [18] that in addition to the benefits of magnetic resonant WPT, the capacitive plates provide immunity to misalignments.

The single-conductor system used in this thesis is shown in Figure 4.1. The transmitter and receiver consist of a single-turn coil with a compensation capacitor placed in parallel and the relay consists of two quarter-wave sheath helices that are coupled to each other via large conductive plates. Hence, although the system utilizes a single-conductor transmission medium, power and data are transmitted wirelessly via magnetic coupling in order to couple to and out of the medium and via capacitive coupling between the conductive plates.

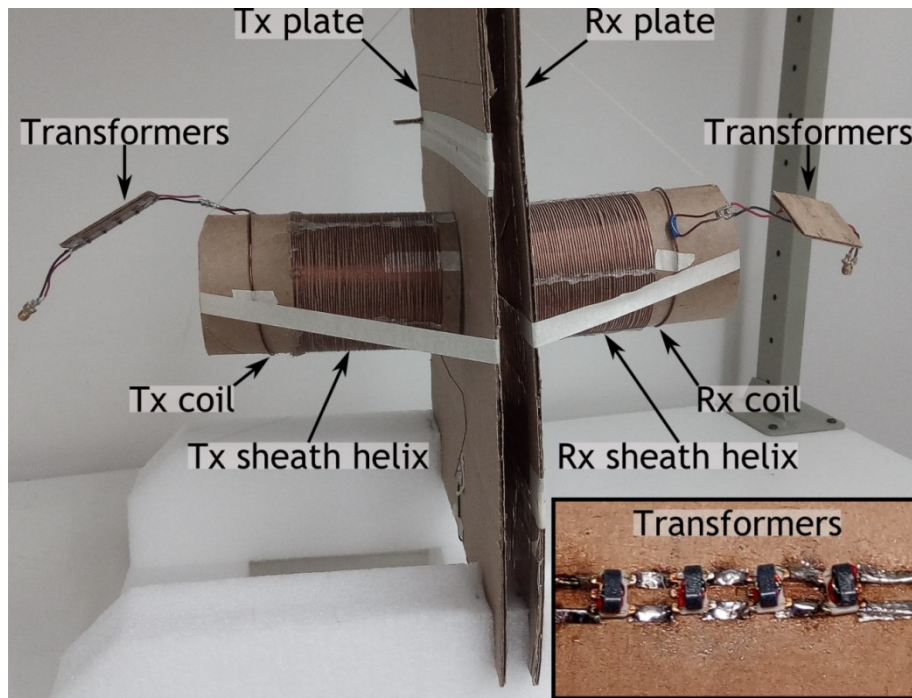
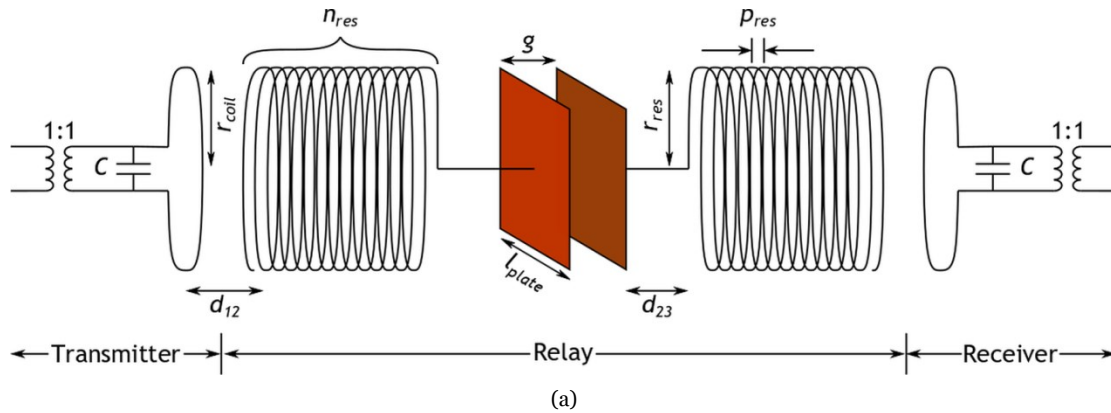


Figure 4.1 (a) System diagram. (b) System implemented in the lab with the transformers used in the inset.

As discussed in Section 3.1, the sheath helix is a slow wave structure, allowing it to be highly compact. Additionally, because the sheath helix is electrically short, it does not radiate, ensuring that the bulk of the power coupled to it is transmitted. For these reasons, the sheath helix was employed as the medium of transmission. The physical properties of the system are listed in Table II. Given these parameters, the resonant frequency of the relay can be calculated by (3.2) to be approximately 6.45 MHz.

Table II System dimensions and component values

Parameter	Description	Value
n_{res}	Sheath helix number of turns	55
r_{res}	Sheath helix radius	42 mm
a_{res}	Sheath helix wire diameter	0.51 mm (24 AWG)
p_{res}	Sheath helix turn pitch	1.51 mm
r_{coil}	Feed coil radius	42 mm
a_{coil}	Feed coil wire diameter	1.29 mm (16 AWG)
l_{plate}	Edge length of capacitive plates	30 cm
t_{plate}	Thickness of capacitive plates	90 μ m
g	Gap between capacitive plates	10 mm
d_{12}	Separation between coil and sheath helix	1 mm
d_{23}	Separation between sheath helix and capacitive plate	10 mm
C	Feed coil compensation capacitor	1.68 nF

The frequency response of the WPT system (henceforth also known as the channel) was measured with a Rohde & Schwarz ZVL13 VNA due to the equivalence between the S_{21} parameter and the frequency response. However, the S_{21} was highly variable when the VNA or the coaxial cables were touched, making the measurement unreliable. A similar effect has been discussed in [46] while measuring monopole antenna parameters when the antenna was directly connected to a measurement device via a coaxial cable. To remedy this, the authors isolated the antenna from the feed cable by a cascade connection of four 1:1 low-loss transformers. This isolation proved to be beneficial in the measurement of the WPT system described here, as well, where the transformers were added to both the input and output ports (see Figure 4.1). Four transformers were used here as well because it was observed to be the minimum amount to satisfactorily stabilize the response (see Appendix A). In order to obtain the frequency response of the channel alone, the effect of the isolation transformers was de-embedded from the

combined system's frequency response in MATLAB by converting the measured S-parameters of the cascaded transformers and the combined system to T-parameters. The frequency responses of the channel with the transformers and of the de-embedded channel are plotted in Figure 4.2. As observed in Figure 4.2, the maximum channel gain for the de-embedded channel occurs around 5.96 MHz and represents a deviation of only 7.7% from the value predicted above by (3.2). The difference can be explained by noting that: (3.2) is an approximation, the capacitive plates do not accurately represent an infinite ground plane (and introduce a non-zero impedance), the combination of the single-turn coil and shunt capacitor may not resonate exactly at the design frequency, and the system may be coupled to other objects due to the charge buildup at the helices' open ends.

4.2 COMMUNICATION ON A SINGLE-CONDUCTOR CHANNEL

A MATLAB simulation was used to test the communication capability of the channel. The channel S-parameters were converted to an IIR channel filter used to filter a simulated baseband signal that was upconverted to 6.01 MHz. The reason 6.01 MHz was used instead of 5.96 MHz is to be able to predict the response when the actual channel is used, which requires the transformers in the measurement setup. Before being filtered by the channel filter, additive white Gaussian noise (AWGN) was added to the passband signal. Finally, the noise-corrupted and filtered signal was processed by a software-defined receiver (SDR) meant to mimic the

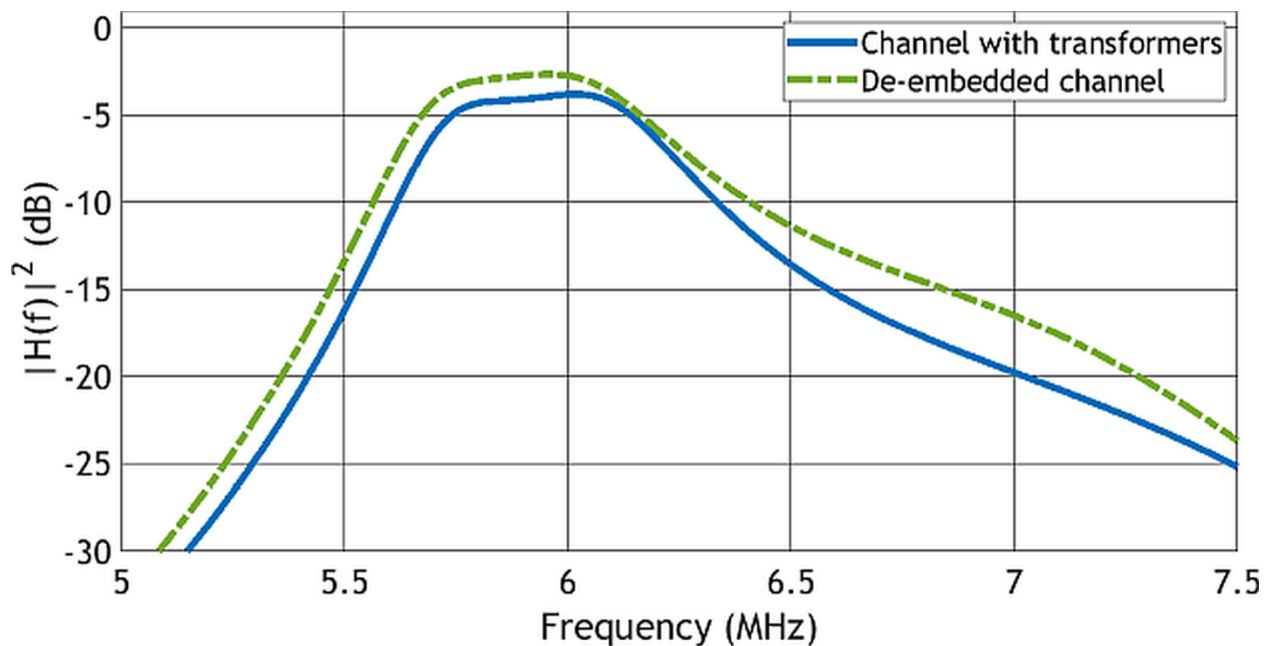


Figure 4.2 Frequency response of the channel.

operation of an envelope detection receiver.

The structure of the SDR consisted of the following blocks (Figure 4.3):

1. fifth-order Butterworth band-pass filter (BPF)
2. envelope detector
3. Schmitt trigger
4. Sampler

4.2.1 ENVELOPE DETECTOR

An envelope detector consists of a rectifying device (e.g., a diode) and a low-pass filter (LPF). Rectifying devices are inherently non-linear and as a result produce outputs whose spectrum consists of intermodulation products of the spectrum of their inputs [3]. Consider the diode, where the current flowing through it is given by [47]

$$i = I_S [e^{v_D(t)/V_T} - 1] \quad (4.1)$$

where I_S is the saturation current (the current when the diode is reverse biased), V_T is the thermal voltage (approximately equal to 25 mV at room temperature), and $v_D(t) = V_D + v_a(t)$ is the voltage across the diode, which is composed of a DC voltage V_D and an AC voltage $v_a(t)$. Using a Taylor representation for the exponential, (4.1) becomes

$$i(t) = I_S \left[e^{V_D/V_T} - 1 + \frac{e^{V_D/V_T}}{V_T} v_a(t) + \frac{e^{V_D/V_T}}{2V_T^2} v_a^2(t) + \dots \right] \quad (4.2)$$

For an amplitude-shift keying (ASK), the amplitude of a sinusoidal carrier signal is modulated such that $V_D = 0$ and the AC voltage is

$$v_a(t) = V_0 [1 + km(t)] \cos(\omega_0 t) \quad (4.3)$$

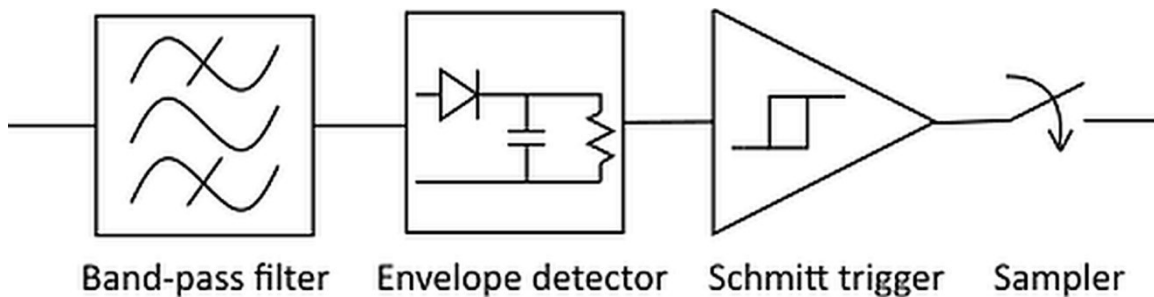


Figure 4.3 SDR block diagram.

where V_0 and $\omega_0 = 2\pi f_0$ are the carrier signal's amplitude and angular frequency, $m(t)$ is the message signal that satisfies $|m(t)| \leq 1$, and k is the modulation index such that $0 \leq k \leq 1$. Substituting (4.3) into (4.2)

$$\begin{aligned}
 i(t) &= I_S \left\{ \frac{V_0}{V_T} [1 + km(t)] \cos(\omega_0 t) + \frac{V_0^2}{2V_T^2} [1 + km(t)]^2 \cos^2(\omega_0 t) + \dots \right\} \\
 &= I_S \left\{ \frac{V_0^2}{4V_T^2} + \frac{V_0^2}{2V_T^2} km(t) + \frac{V_0^2}{4V_T^2} k^2 m^2(t) + \frac{V_0}{V_T} [1 + km(t)] \cos(\omega_0 t) \right. \\
 &\quad \left. + \frac{V_0^2}{4V_T^2} [1 + km(t)]^2 \cos(2\omega_0 t) + \dots \right\}
 \end{aligned} \tag{4.4}$$

Given that the message signal has its own spectrum with a dominant frequency component at f_m , (4.4) dictates that the diode current will have frequency component at DC, f_m , $2f_m$, f_0 , $f_0 \pm f_m$, $2f_0$, $2f_0 \pm f_m$, $2f_0 \pm 2f_m$, and so on. To recover the message $m(t)$, the output in (4.4) can be passed through a filter that will remove the components that are greater than f_m (see Figure 4.4).

However, practical filters are far from ideal and do not have sharp cutoff frequencies. As a result, filtered intermodulation products also make it through to produce a ripple voltage at the

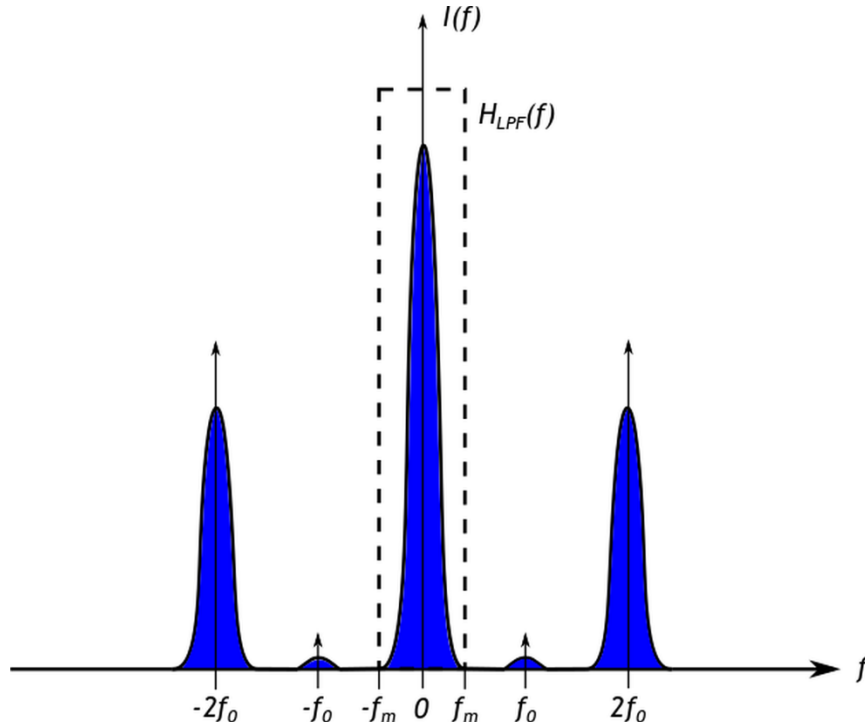


Figure 4.4 Spectra of the rectified signal as given by (4.4) and an ideal low-pass filter.

output. For a first-order LPF, the ripple voltage is approximated by [47]

$$V_r \approx \frac{n\pi V_p f_c}{f_0} \quad (4.5)$$

under the condition that $n\pi f_c/f_0 \ll 1$ where $n = 1$ for a full-wave rectifier and $n = 2$ for a half-wave rectifier, f_c is the cutoff frequency of the LPF, and V_p is the peak of the envelope. Henceforth, a full-wave rectifier is assumed.

The SDR was implemented in MATLAB with a square-law envelope detector as shown in Figure 4.5. The output of the square operation to the input signal in (4.3) produces

$$v_D^2 = \frac{V_0^2}{2}[1 + 2km(t) + k^2m^2(t)] + \frac{V_0^2}{2}[1 + 2km(t) + k^2m^2(t)] \cos(2\omega_0 t) \quad (4.6)$$

Examining (4.4), the $\cos(\omega_0 t)$ term has a smaller factor than the DC and $\cos(2\omega_0 t)$ terms and can be neglected. Hence, (4.4) and (4.6) are approximately equivalent within a factor of $I_S/2V_T^2$.

The cutoff frequency of the LPF was chosen so that the pulse shape of the symbols is retained. For a rectangular pulse shape, it is necessary to maintain sharp transitions and as a result the rise time of the LPF is considered. Rise time T_r is defined as the time it takes for the signal to go from 10% to 90% of the final value and for a first-order LPF is approximated by [48]

$$T_r \approx \frac{0.35}{f_c} \quad (4.7)$$

To maintain sharp transitions, a rise time of at most one tenth of the symbol duration has been chosen, where the symbol duration is given by $T_s = 1/f_m$. Substituting into (4.5) and solving for f_c ,

$$3.5f_m \leq f_c \ll \frac{f_0}{n\pi} \quad (4.8)$$

where the right inequality ensures a small ripple voltage and that the carrier signal is filtered out [49].

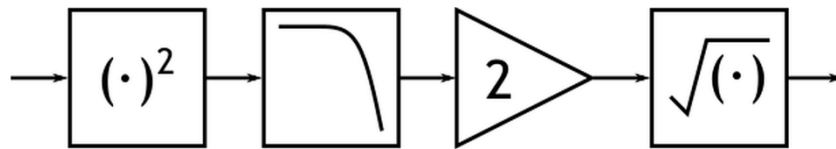


Figure 4.5 Square-law envelope detector.

4.2.2 FIFTH-ORDER BUTTERWORTH BAND-PASS FILTER

The purpose of the input BPF is to remove as much of the unwanted components of the incoming signal. The BPF was centred on f_0 and designed to be a fifth-order Butterworth filter in order to have extremely sharp transitions and a flat passband that will not distort the incoming signal.

To determine the appropriate passband, it is necessary to know the equivalent noise bandwidth. For any filter, the equivalent noise bandwidth is defined as the double-sided bandwidth of a brickwall (ideal) filter that passes the same white noise power as the non-ideal filter and is given by [50]

$$B_N = \int_{-\infty}^{\infty} \left| \frac{H(\omega)}{H_{max}} \right|^2 d\omega \quad (4.9)$$

where $H(\omega)$ is the frequency response of the non-ideal filter and $|H_{max}|$ is the maximum value of the non-ideal filter's response. For a first-order Butterworth filter $B_N = \pi f_c$. For a fifth-order Butterworth filter $B_N = 2.03 f_c$. In order to not affect the output of the envelope detector, the BPF was designed to have the same noise bandwidth as the LPF as follows

$$B_N = \pi f_{c,LPF} = 2.03 f_{c,BPF} \quad (4.10)$$

With the lower limit of $f_{c,LPF}$ given in (4.8) and using (4.10), the cutoff frequency of the BPF was chosen to be $f_{c,BPF} = 1.54 f_{c,LPF} = 5.42 f_m$ (but was set to $f_{c,BPF} = 5.5 f_m$ in the SDR). Figure 4.6 demonstrates the validity of (4.10) (though it shows that $f_{c,BPF} = 4.5 f_m$ would also be quite suitable).

4.2.3 SCHMITT TRIGGER

For on-off keyed (OOK) messages (a type of ASK) the transmitter sends a HIGH value or a LOW value (A and 0 , respectively) corresponding to the transmission of bits 1 and 0 . The probability of error for an envelope detector under OOK modulation is (see Appendix B)

$$p_e = \frac{1}{2} \left[\int_z^{\infty} \frac{2\rho}{N_0} e^{-\frac{\rho^2}{N_0}} d\rho + \int_{\rho=0}^z \frac{2\rho}{N_0} e^{-\frac{\rho^2+A^2}{N_0}} I_0\left(\frac{2\rho A}{N_0}\right) d\rho \right] \quad (4.11)$$

where z is the detection threshold above which the detector detects bit 1 and below which it detects bit 0 , N_0 is the power spectral density of the white noise, and I_0 is the modified Bessel function of the first kind and zero order.

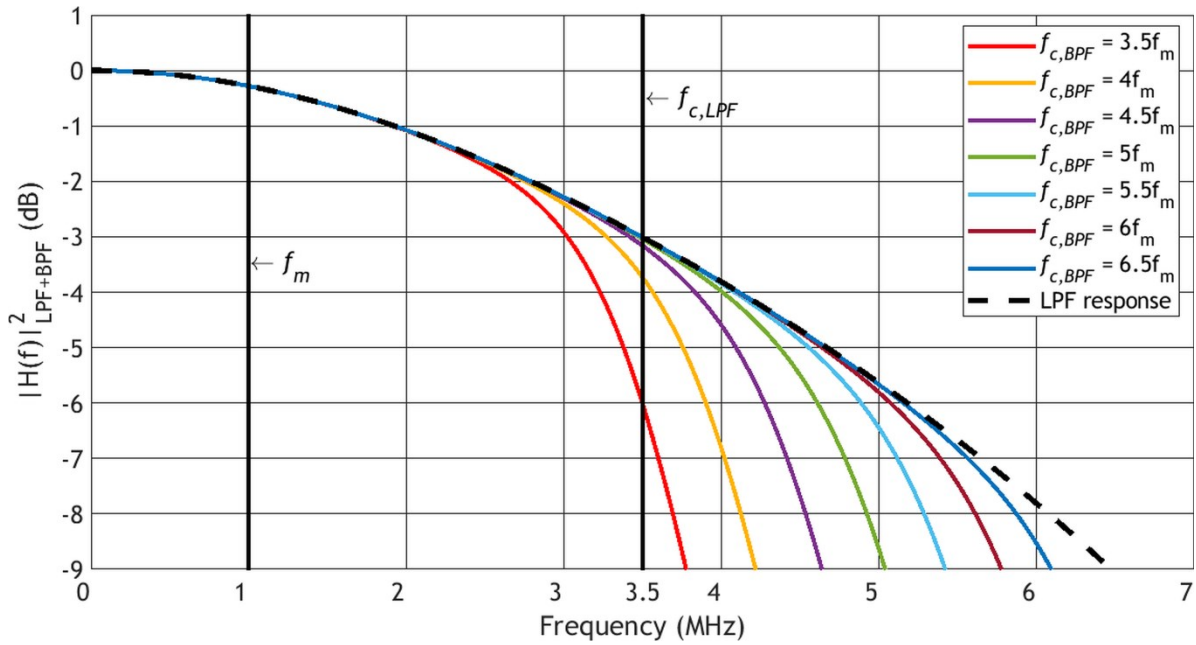


Figure 4.6 Combined effect of an LPF and various BPFs with different cutoff frequencies with $f_m = 1$ MHz.

Eq. (4.11) represents the probability of error for a detector with a single threshold, but performance can be improved with a Schmitt trigger. Figure 4.7 shows that a Schmitt trigger utilizes two threshold levels (z_1 and z_2) with hysteresis to improve the noise immunity. In a single threshold detector the test is very simple: if the signal is above the threshold, output bit 1, otherwise, output bit 0, as shown in Figure 4.8. In a Schmitt trigger, two conditions must be met: (a) if the signal was originally LOW and is now higher than threshold level z_2 , output bit 1, and (b) if the signal was originally HIGH and is now lower than threshold level z_1 , output bit 0, otherwise, maintain the original bit value, as shown in Figure 4.8. To accommodate the extra threshold level, (4.11) is modified to

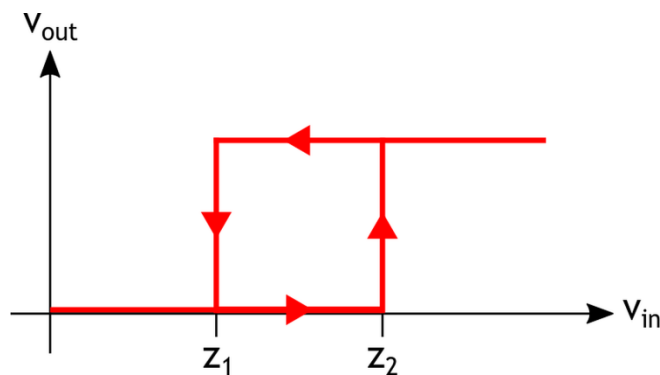


Figure 4.7 Hysteresis loop of Schmitt triggers.

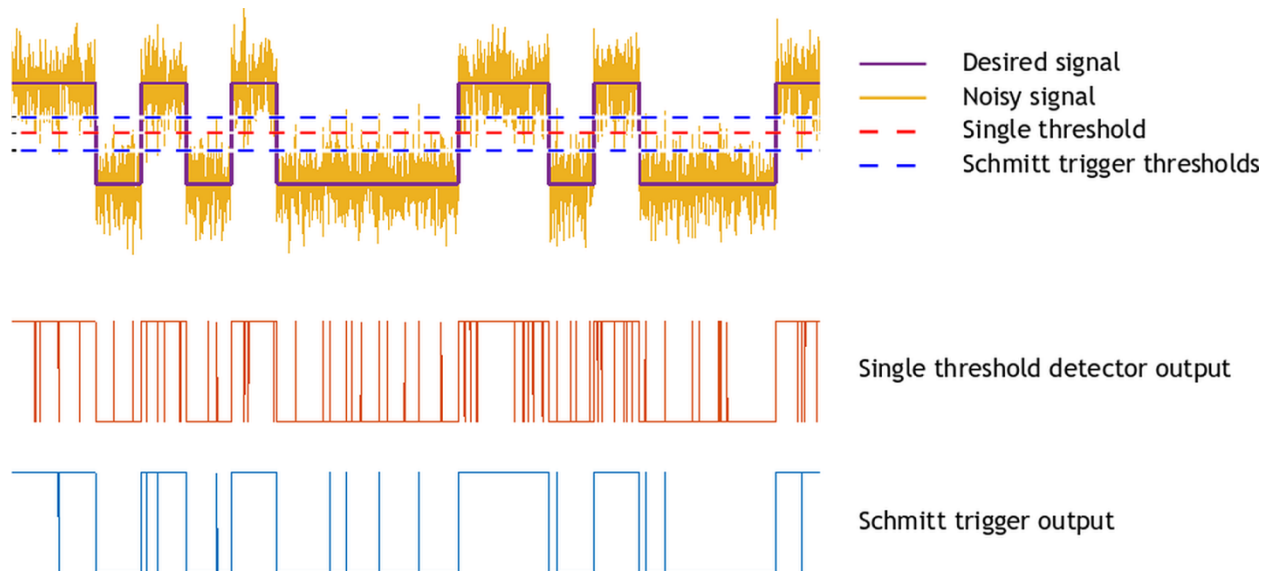


Figure 4.8 Schmitt trigger vs. a single threshold detector.

$$p_e = \frac{1}{2} \left[\int_{z_2}^{\infty} \frac{2\rho}{N_0} e^{-\frac{\rho^2}{N_0}} d\rho + \int_{\rho=0}^{z_1} \frac{2\rho}{N_0} e^{-\frac{\rho^2+A^2}{N_0}} I_0\left(\frac{2\rho A}{N_0}\right) d\rho \right] \quad (4.12)$$

Figure 4.9 compares the performance of the two detectors via a BER vs. SNR curve with $z = A/2$ for the single threshold detector and $z_1 = A/3, z_2 = 2A/3$ for the Schmitt trigger. It is evident that the Schmitt trigger provides an improved performance with a 2.5 dB improvement over the single threshold detector.

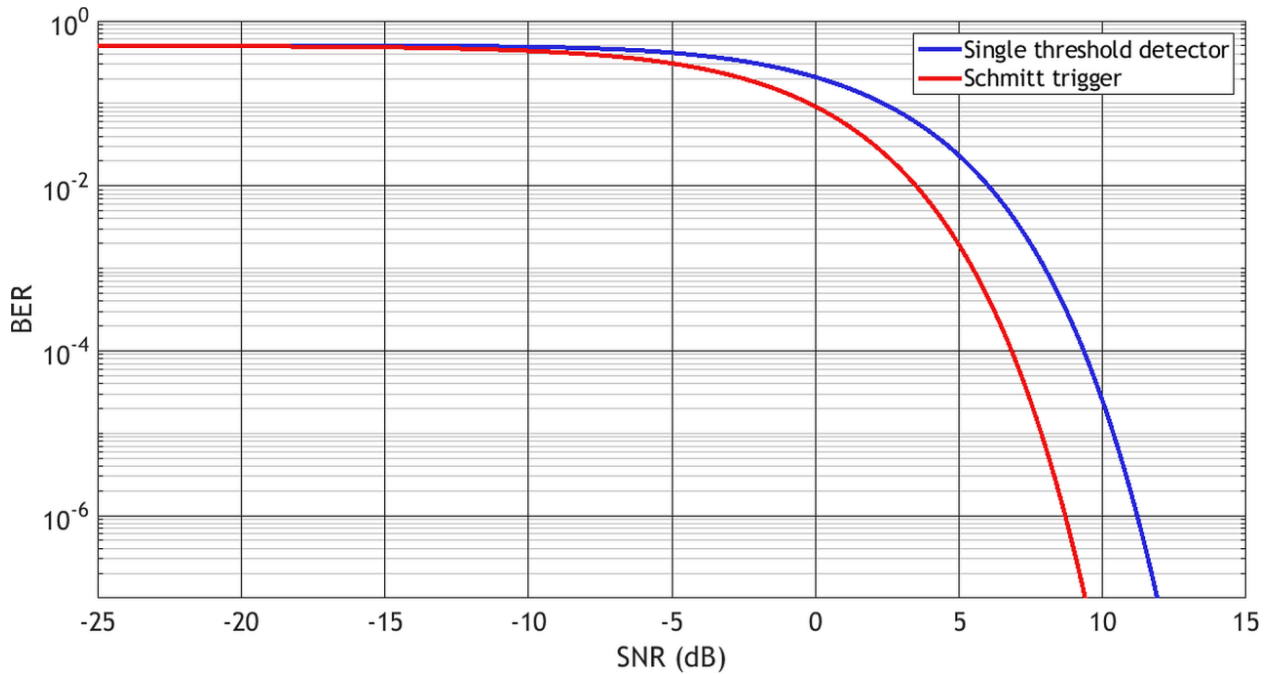


Figure 4.9 BER vs. SNR for a single threshold detector and a Schmitt trigger.

4.2.4 LINE CODES

OOK and modified Miller coding (MMC) were used in the investigation. OOK was chosen due to its simplicity in encoding and decoding and MMC is commonly used in RFID [51] and NFC [52]. In MMC, the bits are represented by the position of a zero pulse within the bit duration as illustrated in Figure 4.10. As shown, there are three code words for: a bit 0 following a bit 0, a bit 0 following a bit 1, and a bit 1, each consisting of four symbols per bit. Hence, for an OOK message, f_m is equivalent to the data rate, but for an MMC message, f_m is equivalent to the symbol rate (which is four times the data rate).

In applications where the receiver is battery-less, the transmitter must also provide power. However, in order to send data on the same frequency simultaneously, the power signal (i.e., the carrier) must be modulated, and that reduces the maximum achievable amount of transmitted

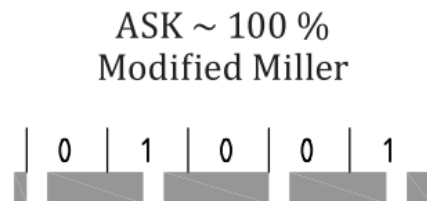


Figure 4.10 Modified Miller encoding as specified in [51]

power. It was shown in [53] that there is a trade-off between achieving maximum power transmission and maximum data rate. MMC is an attempt at minimizing the amount of amplitude modulations to ensure high power transfer. The powers associated with each bit transmission are

$$p_{1|0} = p_{1|1} = \frac{3}{4} \cdot \frac{A^2}{2} \quad p_{0|1} = \frac{A^2}{2} \quad p_{0|0} = \frac{3}{4} \cdot \frac{A^2}{2} \quad (4.13)$$

where $A^2/2$ is the unmodulated carrier power and the notation $x|y$ represents bit x following bit y . Then the total power transmitted is given by

$$\begin{aligned} p &= P(0|0)P(0)p_{0|0} + P(0|1)P(1)p_{0|1} + P(1|0)P(0)p_{1|0} + P(1|1)P(1)p_{1|1} \\ &= \frac{1}{2} \cdot \frac{1}{2} \left(\frac{3}{4} + 1 + \frac{3}{4} + \frac{3}{4} \right) \frac{A^2}{2} = \frac{13}{16} \cdot \frac{A^2}{2} \end{aligned} \quad (4.14)$$

whereas for OOK the transmitted power is $A^2/4$. But because in MMC four symbols are used to represent a single bit, the data rate is a fourth of the OOK rate. Hence, while MMC transmits more power than OOK, its data rate is lower.

4.2.5 SIMULATION AND MEASUREMENT RESULTS

The performance of the channel was tested by creating data streams of 10,000 bits encoded with OOK and MMC, which were upconverted to 6.01 MHz, filtered with the MATLAB channel filter, and processed with the SDR described above. Note that the RFID and NFC standards [51], [52] specify a carrier frequency of 13.56 MHz, whereas the channel operates at 6.01 MHz. Nevertheless, a data rate of 106 kb/s and MMC were used as in [53]. To confirm the results, the same data streams were imported to a Rohde & Schwarz SMW200A vector signal generator, which upconverted them to 6.01 MHz and added white Gaussian noise to them. The signal generator was connected to the single-conductor system via the transformers (as described above) and the output was captured on an oscilloscope. The oscilloscope signals were then processed with the same SDR used in simulation.

BER versus SNR plots were produced for both the simulated and measured outputs to evaluate the performance. To measure the SNR of the measured output, a separate noise measurement was made and the SNR calculated as follows:

$$\begin{aligned} p_r &= E[|R|^2] = E[|S + N|^2] \\ &= E[|S|^2] + 2E[|S|]E[|N|] + E[|N|^2] \\ &= p_s + p_n \end{aligned} \quad (4.15)$$

where $E[\cdot]$ is the expectation function, p_r , p_s , and p_n are the received signal, transmitted signal, and noise powers, respectively, and R , S , and N are the random variables that represent them, respectively. From (4.15), the SNR was calculated as

$$SNR = \frac{p_s}{p_n} = \frac{p_r - p_n}{p_n} \quad (4.16)$$

where p_r and p_n were measured at the output of the BPF.

Equations (4.8) and (4.10) were derived to ensure that the extracted envelope of the incoming OOK signal maintains the sharp rising and falling edges of the rectangular pulse shape. However, they are valid only for flat channels. Because frequency-selective channels (of which the single-conductor system is an example) introduce ISI (i.e., increase T_r), the combination of the channel and the LPF increases T_r above what (4.8) and (4.10) were designed to achieve. The LPF and BPF were designed to produce $T_r = 0.94 \mu\text{s}$ for 106 kb/s OOK messages and a flat channel, but the channel limited T_r to a minimum of 1.3 μs . Via simulation, it was discovered that an $f_{c,LPF}$ of nine times the symbol rate ($f_{c,LPF} = 9f_m$) decreased T_r sufficiently and resulted in better BER performance. The LPF and BPF parameters are listed in Table III. Table III shows that the relationship between $f_{c,LPF}$ and $f_{c,BPF}$ does not adhere to (4.10) any longer, and the BPF's cutoff frequency remains $f_{c,BPF} = 5.5f_m$. Since the BPF's bandwidth is larger than the channel's, and the channel is responsible for most of the signal distortion, the BPF does not appreciably distort the signal further.

Table III LPF and BPF parameters

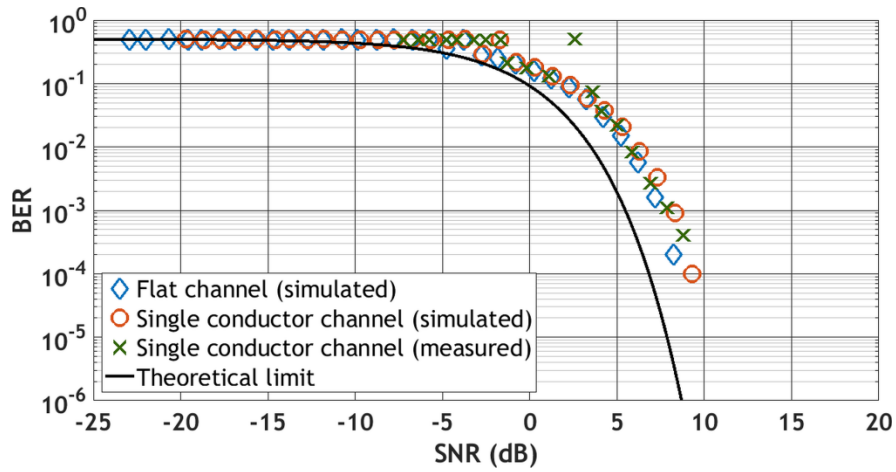
Parameter	Case 1	Case 2	Case 3
OOK Data rate, R_b (kb/s)	106	424	1000
MMC Data rate, R_b (kb/s)	26.5	106	250
LPF cutoff frequency, $f_{c,LPF}$ (MHz)	0.954	3.816	9
BPF bandwidth, $B_{BPF} = 2f_{c,BPF}$ (MHz)	1.166	4.664	11

4.2.5.1 On-off keying

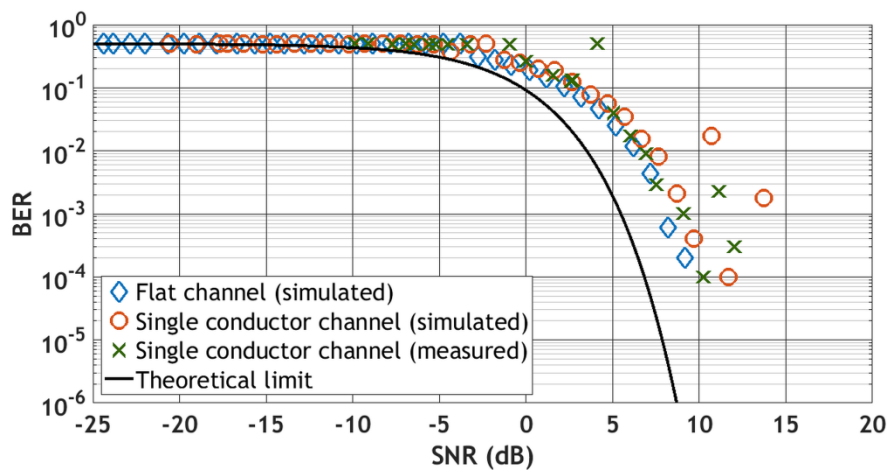
The BER performance of the channel for OOK data is shown in Figure 4.11 for both the simulated and measured outputs. The data rates used were 106, 424, and 1000 kb/s. These results were compared to the performance of a flat channel with only AWGN present.

Observe in Figure 4.11 that as the data rate is increased, the BER increases as well and the channel performance deviates from the flat channel's. Examining the eye diagram for 106 kb/s in Figure 4.12(a), the signal shape is unambiguous, with sharp transitions, a small ripple voltage, and a wide-open eye. This is expected because the bulk of the signal spectrum is captured within the channel bandwidth (approximately 530 kHz). For 424 kb/s [Figure 4.12(b)], the transitions widen, the ripple voltage is increased, the rise time is increased (i.e., more ISI is introduced), the signal begins to resemble a triangular wave more than a rectangular one, and the eye begins to close as the channel filters more of the signal's spectrum. At 1000 kb/s [Figure 4.12(c)], the channel filters almost all of the signal's spectrum and causes the transitions to be very wide, the rise time to greatly increase (such that a single symbol interferes with the next three symbols due to ISI), and the eye to close almost completely. Moreover, the $f_{c,LPF}$ no longer satisfies the right inequality of (4.8) so that a large ripple voltage is present, which produces errors at the output of the Schmitt trigger.

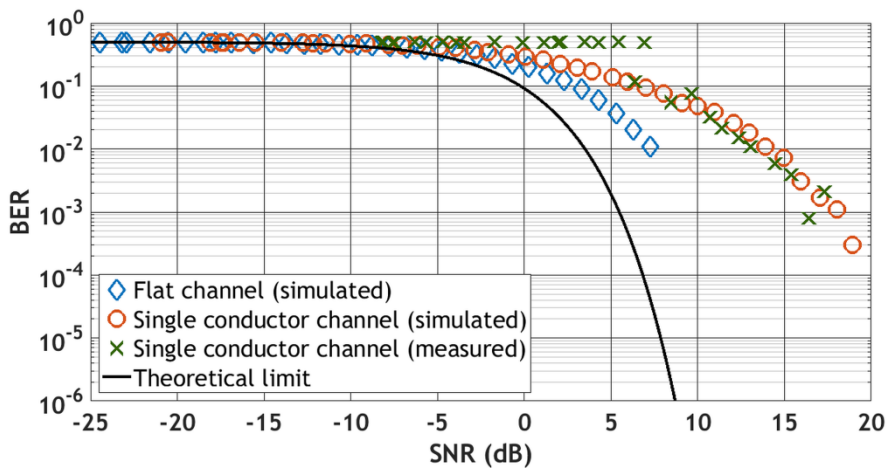
At 106 kb/s, the performance does not exactly match that of the flat channel because, as mentioned previously, a higher $f_{c,LPF}$ is required to combat the increased T_r produced by the channel. This higher cutoff frequency introduces a higher ripple voltage, which is detrimental to performance.



(a)

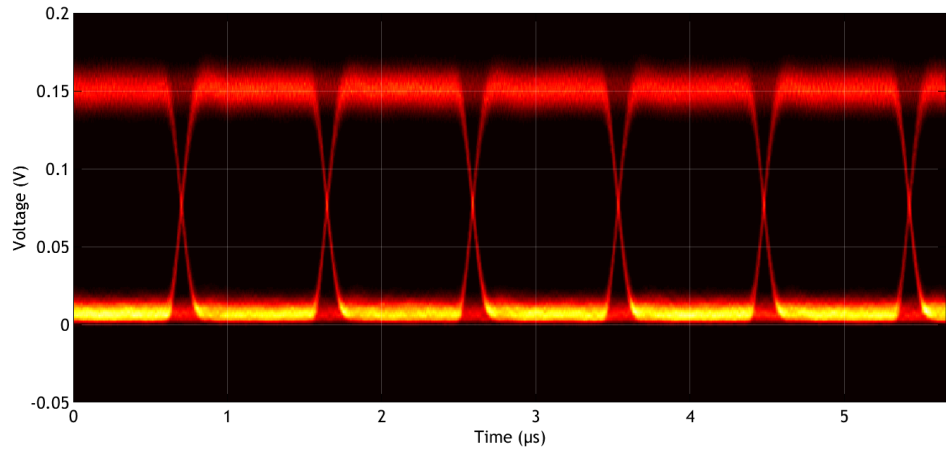


(b)

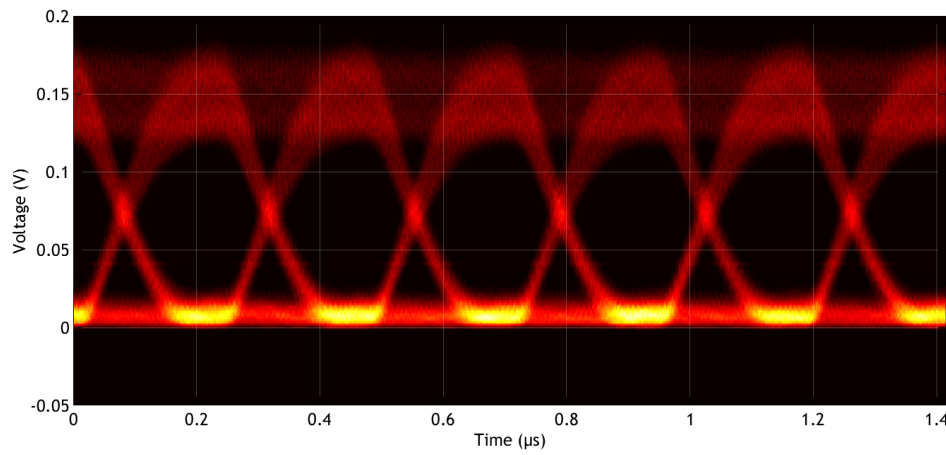


(c)

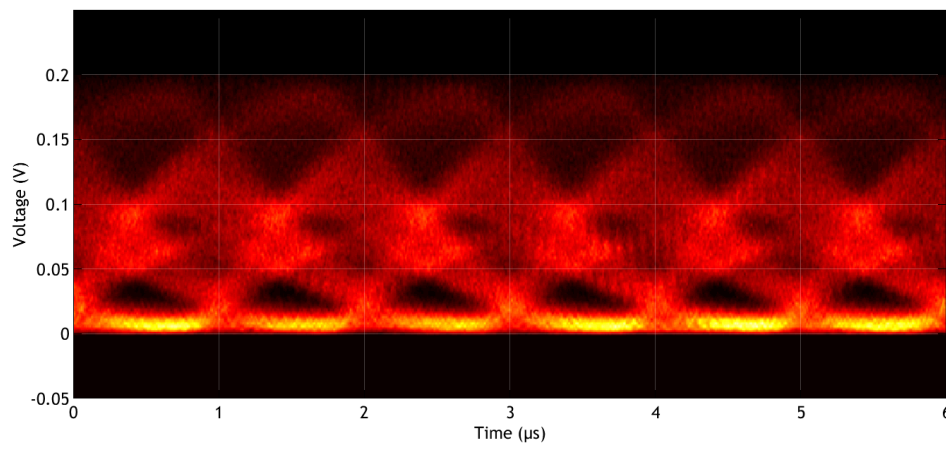
Figure 4.11 BER vs. SNR for OOK modulated signals with varying data rates: (a) 106 kb/s, (b) 424 kb/s, and (c) 1000 kb/s.



(a)



(b)



(c)

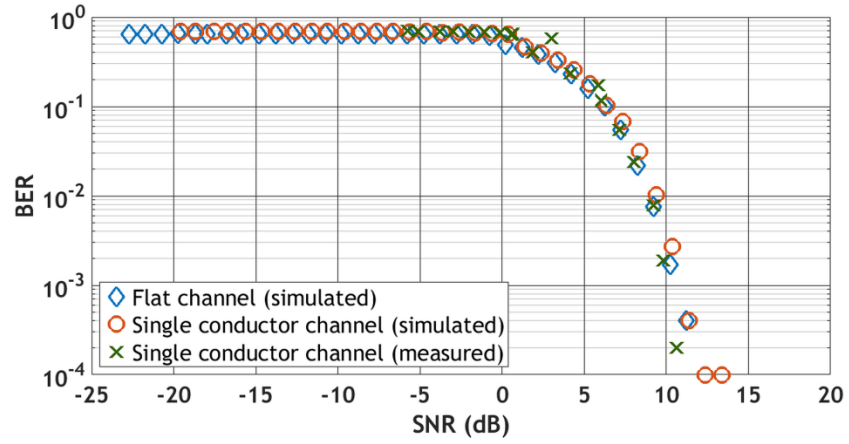
Figure 4.12 Eye diagrams for the demodulated OOK signals with data rates: (a) 106 kb/s, (b) 424 kb/s, and (c) 1000 kb/s.

4.2.5.2 Modified Miller code

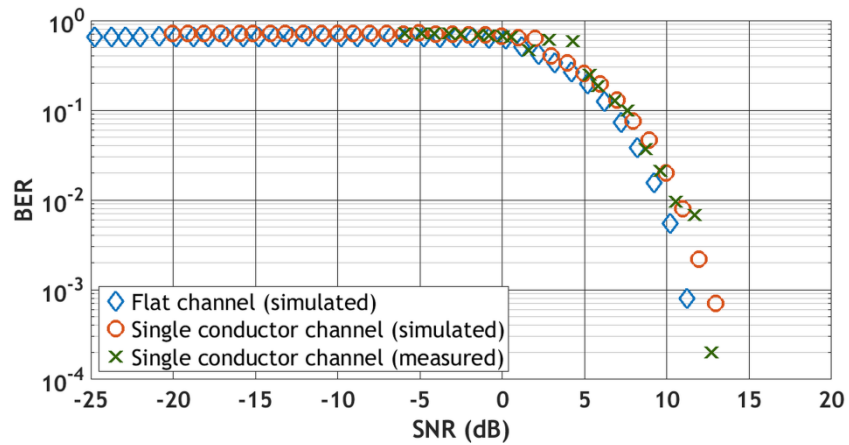
The BER performance was also investigated for MMC data as it was for OOK data. The data rates used were 26.5, 106, and 250 kb/s to maintain the same symbol rates as those used for OOK.

Figure 4.13 shows that as the data rate increases, the BER increases as well. The results can be explained in the same manner as for OOK because the pulse shape is the same (26.5 kb/s MMC is analogous to 106 kb/s OOK, 106 kb/s MMC is analogous to 424 kb/s OOK, and 250 kb/s MMC is analogous to 1000 kb/s OOK). However, the case of 250 kb/s MMC is of note as evidenced by the eye diagram in Figure 4.14(c). Because MMC has short durations in which the signal is low, the signal does not reach that level at this high rate. Thus, the eye not only closes from the top but also from the bottom, as opposed to its corresponding case of 1000 kb/s OOK shown in Figure 4.12(c). Therefore, message recovery is further degraded, as compared to the recovery of OOK messages.

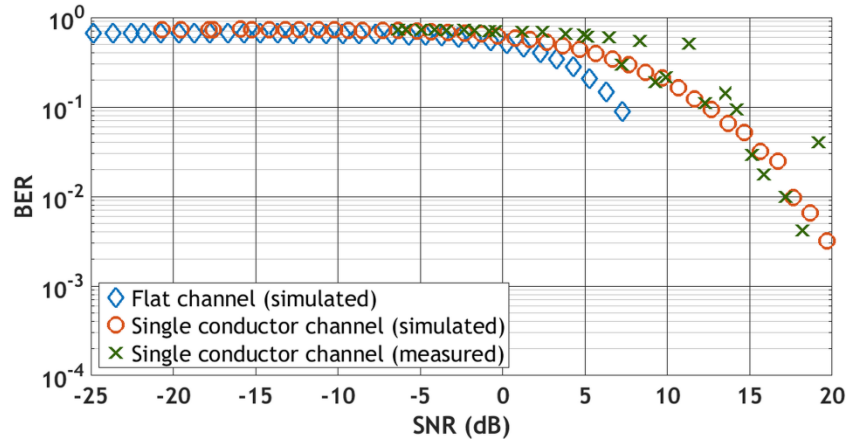
Comparing Figure 4.11 and Figure 4.13, it can be seen that the BER for OOK flattens at 0.5 but for MMC it flattens above 0.5. As well, the successful recovery of MMC messages requires higher SNR than their corresponding OOK messages. The reason is that MMC uses four symbols to encode a single bit and all four must be recovered correctly as opposed to the single symbol per bit used in OOK. Additionally, the MMC BER for the single-conductor channel is higher than that of the flat channel, which is most likely due to ripple voltage and ISI.



(a)

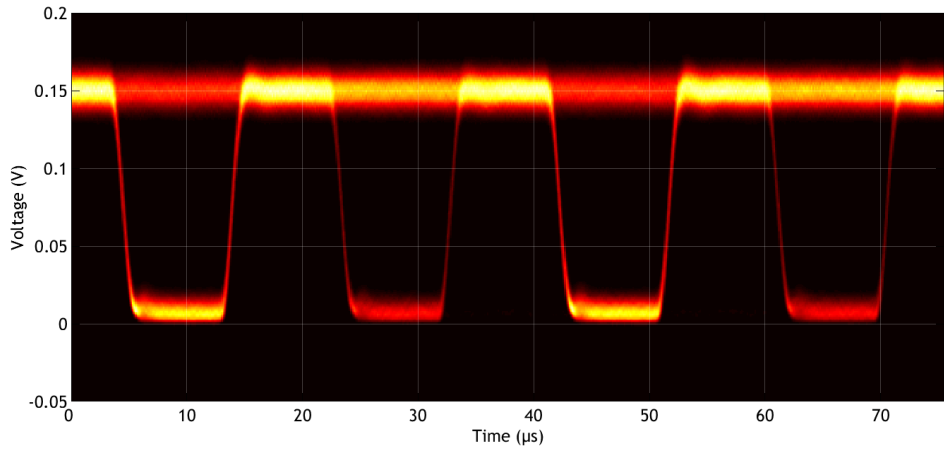


(b)

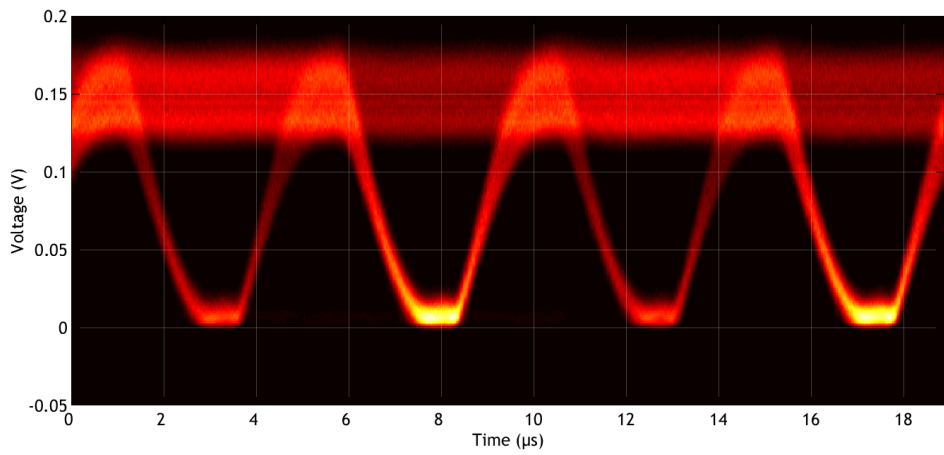


(c)

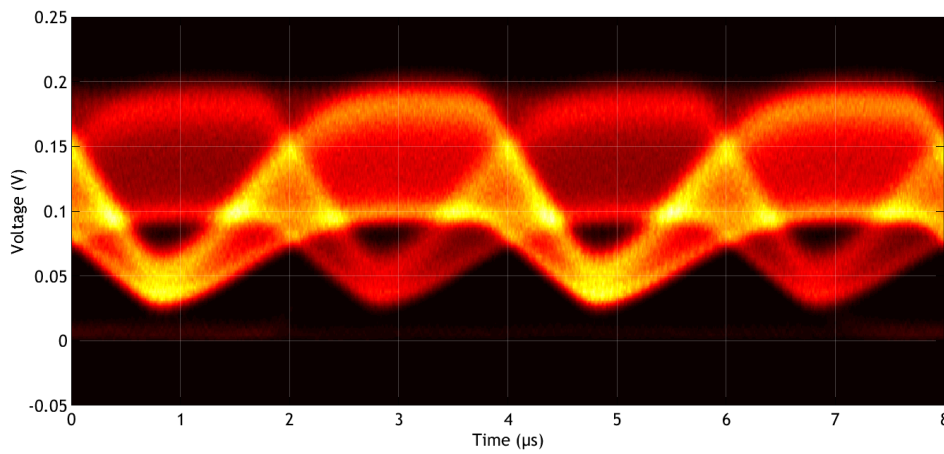
Figure 4.13 BER vs. SNR for MMC modulated signals with varying data rates: (a) 26.5 kb/s, (b) 106 kb/s, and (c) 250 kb/s.



(a)



(b)



(c)

Figure 4.14 Eye diagrams for demodulated MMC modulated signals with data rates: (a) 26.5 kb/s, (b) 106 kb/s, and (c) 250 kb/s.

4.3 IMPROVED ASYNCHRONOUS ASK RECEIVER

4.3.1 ENVELOPE DETECTOR

Looking at the AM signal in (4.3), when k is small the HIGH and LOW levels of the signal become very close. Discussed in 4.2.1, a ripple voltage is always present, pushing the HIGH level ripple towards the LOW level. Thus, if the ripple is large enough, a bit 1 may be erroneously detected as a bit 0. Even if the ripple is small, the effect of noise will be exacerbated due to the ripple.

From (4.5), the ripple may be reduced by decreasing $f_{c,LPF}$. However, there is a lower limit to $f_{c,LPF}$, beyond which the BER increases. The criterion for this lower limit was set so that the LOW level will not be pushed towards the HIGH level. It was seen in Figure 4.14 for an MMC message at 250 kb/s that the eye closes from the bottom and degrades message recovery, which is what this criterion is meant to prevent. The worst case scenario occurs when the filtered signal is just able to decay to the LOW level and remain there for the briefest moment before encountering a rising edge. Mathematically, for a first order LPF, this can be expressed as

$$V_0(1+k)e^{-2\pi f_{c,LPF}/f_m} \leq V_0(1-k) \quad (4.17)$$

where the HIGH level is $V_0(1+k)$ and the LOW level is $V_0(1-k)$. Solving for $f_{c,LPF}$, the minimum cutoff frequency is

$$f_{c,LPF} \geq \frac{f_m}{2\pi} \ln\left(\frac{1+k}{1-k}\right) \quad (4.18)$$

Eq. (4.18) produces lower cutoff frequencies than (4.8) (for values of k ranging from 0 to very close to 1), and consequently, significantly reduces the ripple voltage. It should be noted that when 100% ASK is used, (4.18) dictates that the cutoff frequency be infinite. Since this result does not make practical sense, in such cases using $0.9 \leq k < 0.99$ is good enough.

4.3.2 INPUT BAND-PASS FILTER

Consider that the decision making device is a single threshold detector with a threshold level halfway between the LOW and HIGH levels. Due to the slowed down signal decay, the duration of bit 0 is shortened. The exact fraction by which the duration is shortened is

$$C = \frac{\ln(1-k)}{\ln(1-k) - \ln(1+k)} \quad (4.19)$$

C ranges from 0.5 to 1 for k ranging from 0 to 1, respectively. This shorter duration requires the receiver to sample the symbols more precisely, which requires a more complex receiver. Fortunately, this can be easily resolved with an input BPF.

The BPF distorts both the rising and falling edges of the message signal. However, the envelope detector only distorts the falling edges. In this manner, the bit 1 durations are also shortened, thereby lengthening the duration of the bit 0s. Figure 4.15 shows the combined effect when detecting a signal with $f_0 = 180$ kHz and $f_m = 4$ kBd (Qi protocol [54]). Without the BPF, the bit 1 and bit 0 durations are $\Delta t_{AC} = 368$ μ s and $\Delta t_{CE} = 132$ μ s, respectively. The BPF evens out the durations by changing them to $\Delta t_{BD} = 319$ μ s and $\Delta t_{DF} = 181$ μ s, respectively.

The BPF was designed as a fifth-order Butterworth filter with a bandwidth that captures at least 95% of the baseband signal's power. For a rectangular pulse shape, the single-sided bandwidth that contains at least 95% of the power was numerically found to be at least twice the symbol rate. It was discussed in Section 4.2.2 that the noise bandwidth of the BPF needs to be at least as large as the noise bandwidth of the envelope detector's LPF. By using (4.18), the noise bandwidth of the LPF is much smaller than that of the BPF, and as a result, does not need to be considered in the BPF design.

4.3.3 SIMULATION RESULTS

To test the above assertions, an SDR was simulated in MATLAB. For the investigation, the

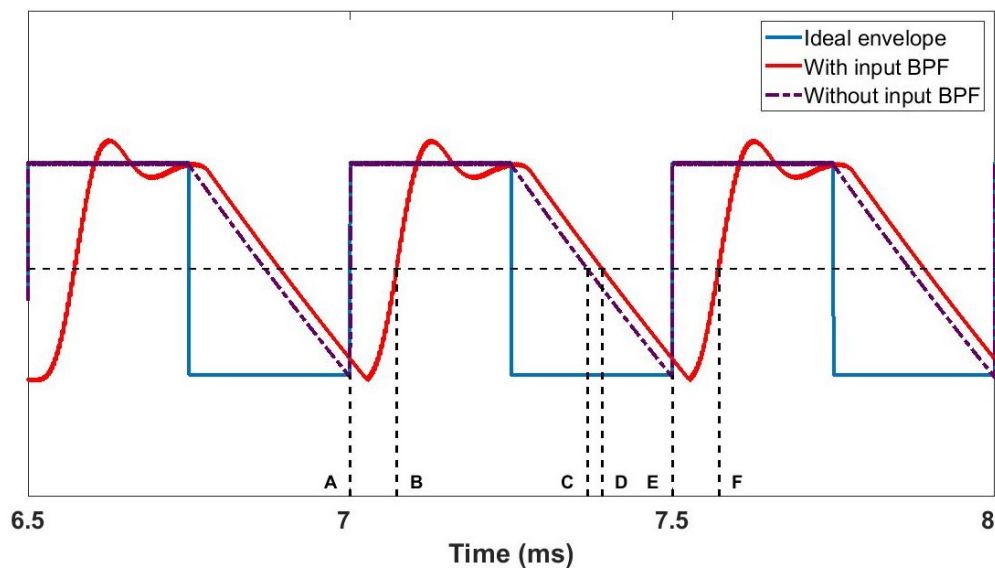


Figure 4.15 Contribution of the BPF in balancing the symbol durations.

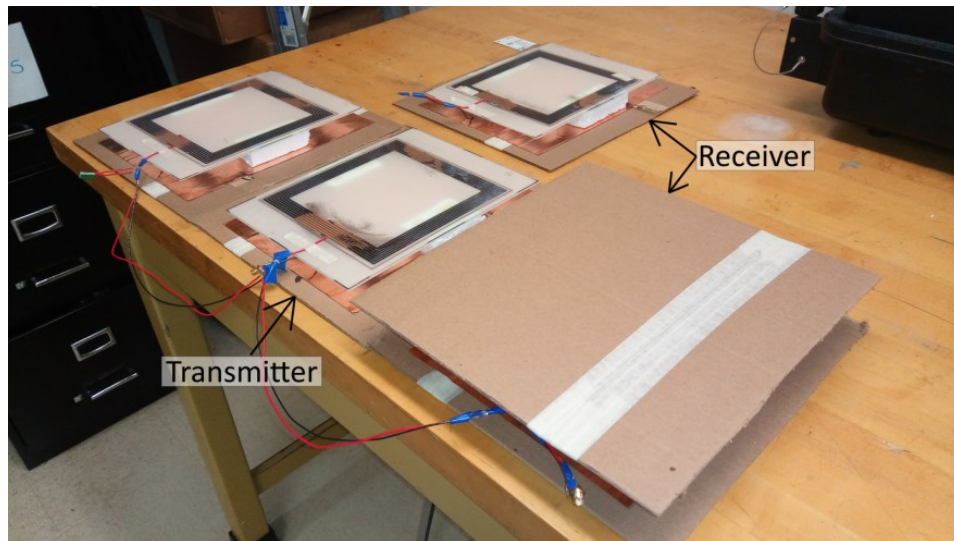
square-law envelope detection used for the simulation in Section 4.2.1 has been replaced with a different algorithm that mimics the operation of the envelope detector more closely (see Appendix C).

As well, the physical channel was replaced with one developed for the Qi protocol [see Figure 4.16(a)] with the frequency response shown in Figure 4.16(b). The biphasic mark line code specified in the protocol [54] was used, where bit 1 is represented by a level change at the beginning and at half the bit duration, and bit 0 is represented by a level change only at the beginning of the bit duration (see Figure 4.17). [54] also specifies a bit rate of 2 kb/s (hence, the symbol rate is $f_m = 4$ kBd). As before, a stream of 10,000 encoded bits was generated in MATLAB, shaped with rectangular pulses, and upconverted to 180 kHz. The modulation index was set to $k = 0.07$ based on measurements obtained from a commercial Qi receiver communicating with a transmitter. Using this information and (4.18), $f_{c,LPF} = 89.3$ Hz, which is 97.8% smaller than the symbol rate and 99.4% smaller than the cutoff frequency specified by (4.8). The BPF was designed to have a bandwidth of 16 kHz (four times the symbol rate) centred at 180 kHz.

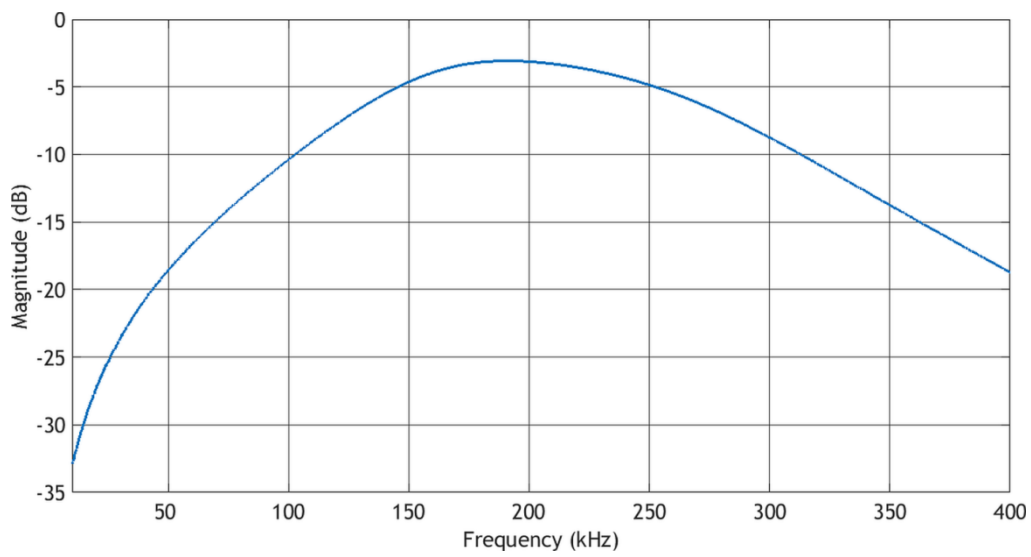
The simulation was run in a Monte-Carlo fashion with $f_{c,LPF}$ being both higher and lower than the 89.3 Hz value. The resulting BER curves are plotted in Figure 4.18. Figure 4.19 compares the individual BER performances, where it is evident that a design based on (4.18) indeed results in the least amount of errors. Three remarks can be made about Figure 4.18 and Figure 4.19:

1. With $f_{c,LPF} = 14$ kHz [from (4.8)], the error is always high because the HIGH level ripple voltage is predicted by (4.5) to be $0.261V_0$, but the difference in levels is only $0.14V_0$.
2. With $f_{c,LPF} = 44.6$ Hz (half the optimal $f_{c,LPF}$), the error increases significantly because the signal does not decay all the way to the LOW level. At $f_{c,LPF} = 44.6$ Hz, the signal only decays to $0.998V_0$, which is only slightly below the threshold of the single threshold detector.
3. While $f_{c,LPF} = 89.3$ Hz achieves a better BER than $f_{c,LPF} = 357.1$ Hz (as shown in Figure 4.19), Figure 4.18(d)-(e) show that the BER performance with the latter frequency is more consistent than with the former. This is due to the fact that a lower $f_{c,LPF}$ shortens the LOW level durations (Figure 4.15). Therefore, the sampling clock must be more accurate. With a slightly higher $f_{c,LPF}$, the receiver becomes more immune to

sampling jitter since the LOW and HIGH level durations are more equal, as shown in Figure 4.20, leading to more consistent behaviour.



(a)



(b)

Figure 4.16 (a) Qi channel and (b) its frequency response (S_{21} parameter).

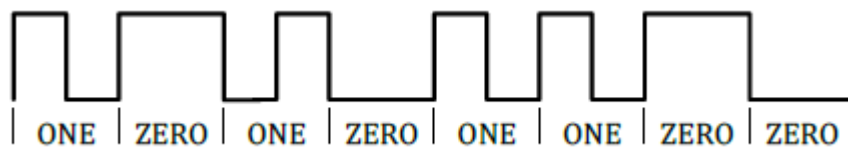


Figure 4.17 Biphas mark line code [54].

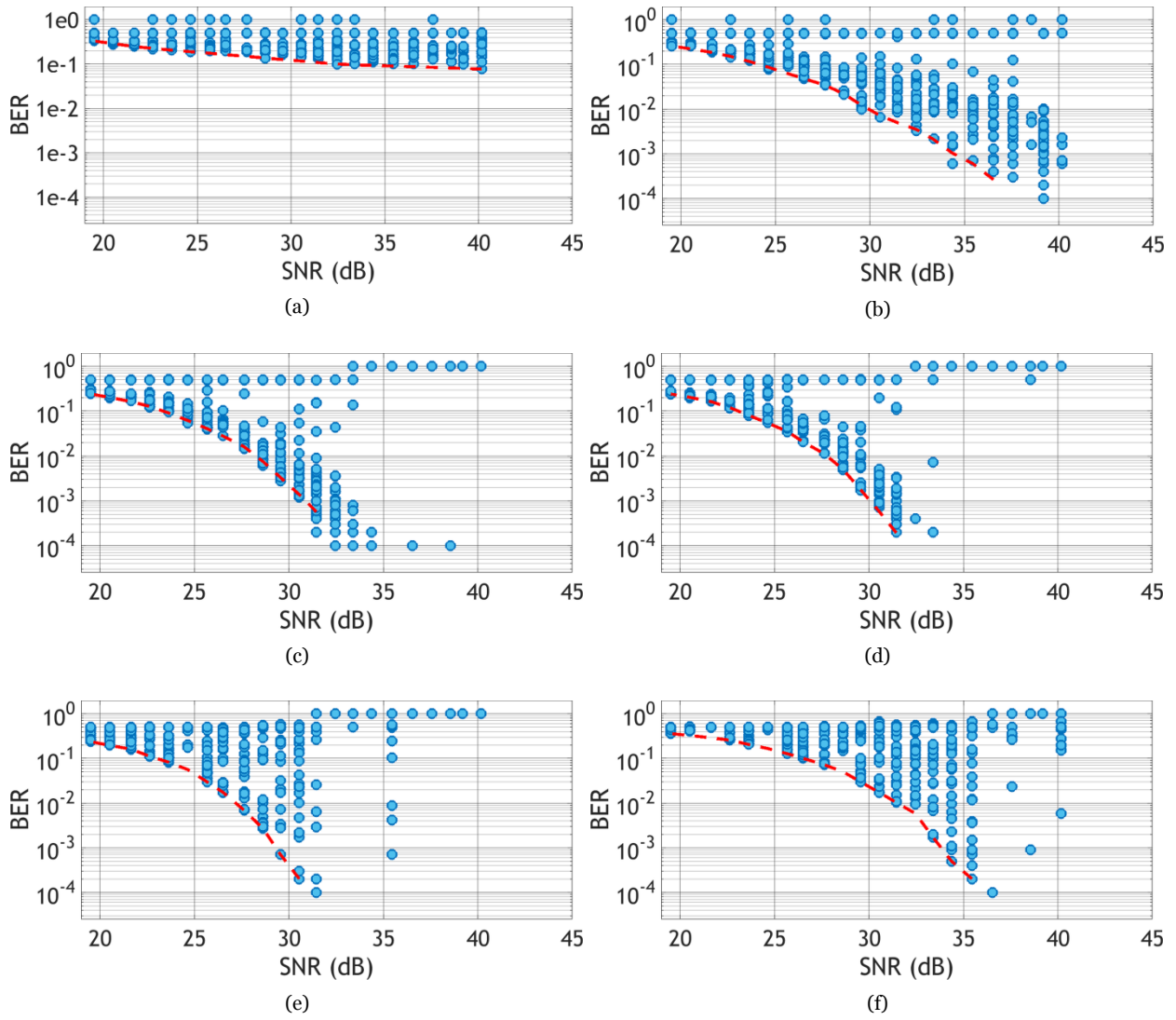


Figure 4.18 BER performance for various cutoff frequencies: (a) 14 kHz, (b) 6 kHz, (c) 1.28 kHz, (d) 357.1 Hz, (e) 89.3 Hz, and (f) 44.6 Hz. The dashed line approximates the best performance at each frequency.

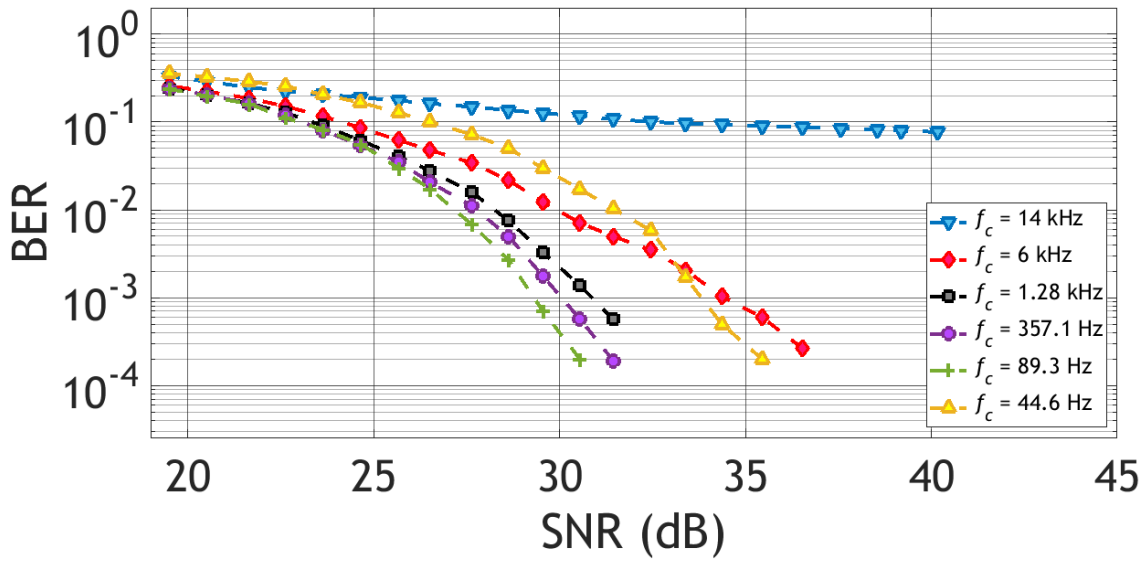


Figure 4.19 Performance comparison of receivers with different cutoff frequencies.

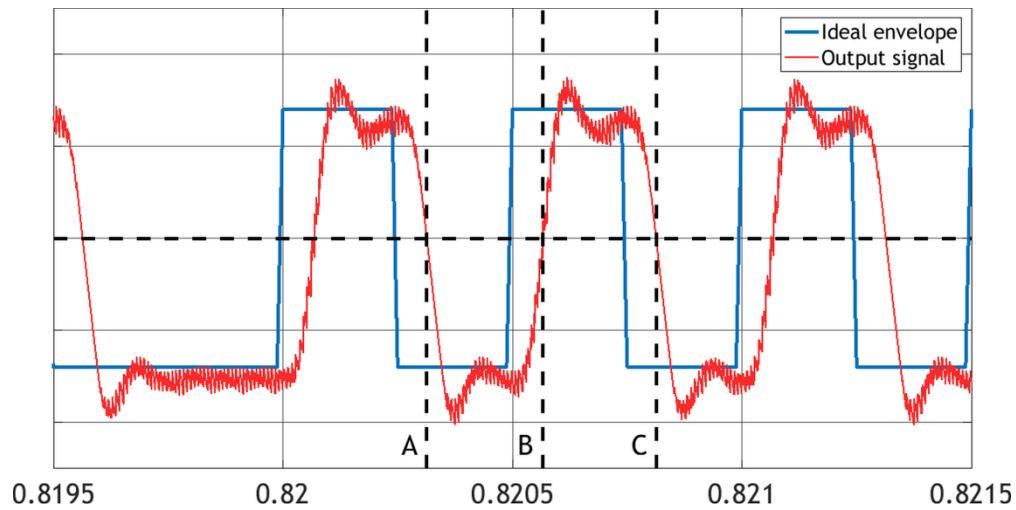


Figure 4.20 Received signal after passing through an envelope detector with $f_{c,LPF} = 357.1$ Hz. The HIGH and LOW level durations are $\Delta t_{AB} = 253 \mu\text{s}$ and $\Delta t_{BC} = 246 \mu\text{s}$, respectively.

4.3.4 APPLICATION TO WIPT

The above design procedure was shown to be quite robust in its reduction of errors for a variety of modulation indices but is also elegant in its simplicity, where the single most important design parameter is simply the cutoff frequency of the LPF in the envelope detector stage.

Moreover, it is predicted that this design can be very beneficial in SWIPT and wirelessly powered backscatter communication. One method by which battery-less WPT receivers communicate with transmitters is load modulation (as discussed above for both RFID [51], [52] and Qi [54] power receivers) due to its low power consumption [55]. Because load modulation requires the WPT receiver to change its impedance [56], the receiver takes itself in and out of the impedance matched condition in order to communicate, which prevents it from receiving the maximum available power from the WPT transmitter. The level of mismatch (i.e., the reflection coefficient) sets the modulation index [55], [57]. Thus, reliable ASK communication requires 100% modulation but necessitates a high level of mismatch. The receiver design procedure discussed above improves the reliability of communication with a low modulation index, which enables the WPT receiver to avoid deep impedance mismatches and ensures high power transfer.

In addition, this method may be beneficial in WPT transmitter-to-receiver communication in the sense that a WPT transmitter may transmit a signal whose amplitude is more constant due to the low modulation index (i.e., higher power), and the receiver will be able to recover the message more reliably.

Chapter 5 Band-Pass Filter Theory in the Design of Single-Conductor Channels

Power and data transfer have traditionally been dealt with separately, and for a good reason. Consider for example the frequency response of a resonant WPT system with frequency splitting, as in Figure 5.1. Power transfer attempts to achieve either the maximum power transferred to the load (i.e., maximum transducer gain $|S_{21}|$), which occurs when the system is operated at either f_{TG1} or f_{TG2} [as given by (2.75) and (2.76)], or a high power gain, which occurs when the system is operated at f_{PG} [as given by (2.63)]. In both cases, power transfer benefits most when a single sinusoid is transmitted.

On the other hand, data transfer attempts to maximize the data rate (i.e., the capacity of the channel), which is possible only if the signal occupies wider bandwidth. Even though the frequency-selective nature of the channel in Figure 5.1 will distort the data signal, the problem can be remedied using channel equalization or the water-filling power allocation technique [53]. Thus, a frequency-selective channel is much more detrimental to WPT than it is to data transfer. Hence, achieving both maximum power transfer and maximum data rate is impossible and a trade-off exists [53], [58].

However, it has been reported in literature that when it comes to AC-to-DC power conversion, WPT also stands to benefit from utilizing wider bandwidths. Due to the non-linear nature of a

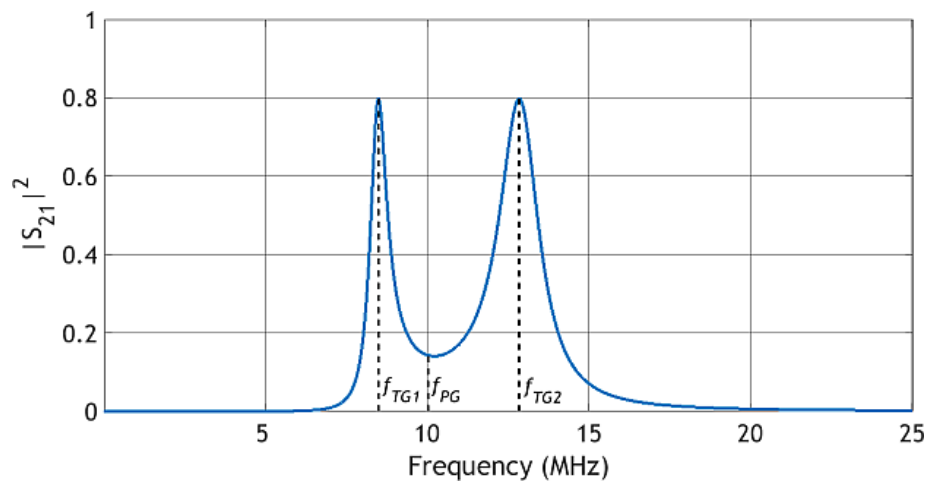


Figure 5.1 Channel frequency response for a resonant WPT system with frequency splitting.

diode, which is often used in AC-to-DC power converters, it was discovered by Trotter et al. [59] that some signals that exhibit large peak-to-average power ratios (PAPR) result in better power conversion efficiencies. Such signals (called power optimized signals in literature) exhibit wider bandwidths than the single tone sinusoids that are traditionally used. The signals indicated by [59] as good candidates include: multitone signals, Gaussian waveforms, and raised cosine waveforms. Collado et al. [60] showed that other high PAPR signals such as OFDM (used in modern communication networks), white noise, and chaotic signals are also excellent candidates. Boaventura et al. [61] mathematically demonstrated that when the frequency components of the power optimized signals are in phase, the efficiency is maximized. The results of [59]–[61] are significant to SWIPT as they demonstrate that raised cosine and Gaussian waveforms, which are commonly used in communication and satisfy the in-phase condition for maximum efficiency, as well as OFDM signals are better suited for WPT than the traditionally used single sinusoid. These results were applied in SWIPT to enhance the performance of communication to and from battery-less sensors and to create novel modulation schemes for WPT [62]–[65]. It is worthwhile to note that the conclusions drawn in [59]–[61] are not valid for voltage multiplier rectifiers [66] or at high input powers [67].

The above discussion points to the conclusion that signals occupying non-zero bandwidth are beneficial to both communication and WPT (with a rectifying receiver). However, the channel may be frequency-selective and may require one or more of the following actions:

- Equalization to undo the distortion caused by the channel on the communication signal and to reduce ISI.
- Power allocation to frequencies for which the channel gain is strongest, according to the conventional or modified water-filling algorithm, in order to increase the channel capacity [13], [53], [58].
- Power allocation to frequencies for which the channel gain is strongest in order to exploit the rectifier's non-linearity and harvest more power [13], [63].

Hence, both WPT and communication will benefit from a frequency-flat channel.

In this chapter, the design of frequency-flat resonant WPT channels is considered based on the design of Butterworth band-pass filters. BPF theory was chosen because of its ease of use and because bandwidth is a design parameter. However, it should be noted that the size of the bandwidth is not without a limit and is governed by the Bode-Fano criterion [68].

Although the design of BPFs using coupled resonators is well established [3], [69], it is underutilized among resonant WPT designers. In [70], [71], the authors describe the method for resonant WPT system design based on BPF theory. However, their conclusions only focus on its ease of use over other design methods and do not delve into the benefits of being able to choose the bandwidth. In [72], the authors note that, contrary to popular belief, use of the high Q resonators required for high power transfer (discussed in Section 2.2.3) does not necessarily produce small bandwidths. They exploited this fact to construct a resonant WIPT channel but did not use BPF theory. As noted in [73], the ability to choose bandwidth as a design parameter is highly advantageous to the design of resonant WIPT channels. Here, BPF theory is extended to the design of resonant WPT systems employing coupled quarter-wave sheath helices with bandwidth as the main parameter.

5.1 INDUCTIVELY COUPLED RESONATORS IN THE DESIGN OF MAXIMALLY FLAT BAND-PASS FILTERS

Consider the N^{th} order ladder network BPF circuit in Figure 5.2(a). The series component values are given by [3]

$$L_n = \frac{Rg_n}{\Delta\omega_0}$$

$$C_n = \frac{\Delta}{Rg_n\omega_0}$$
(5.20)

and the shunt component values are given by

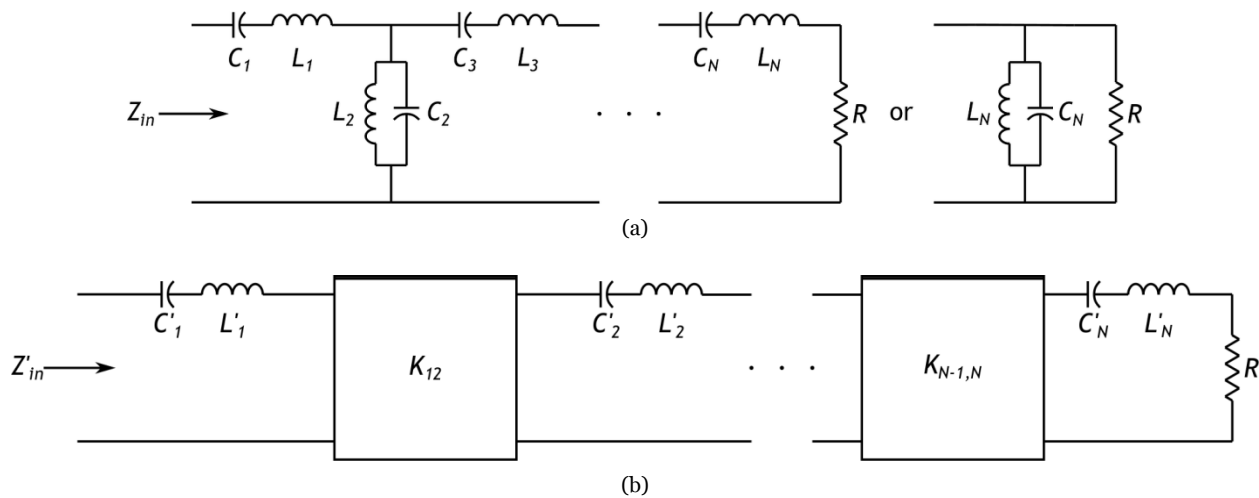


Figure 5.2 An N^{th} order (a) ladder network and (b) impedance transformer synthesis of a BPF.

$$L_n = \frac{R\Delta}{g_n\omega_0} \quad (5.21)$$

$$C_n = \frac{g_n}{R\Delta\omega_0}$$

where the resonant frequency ω_0 and the fractional bandwidth Δ are given by

$$\omega_0 = \sqrt{\omega_1\omega_2} \quad (5.22)$$

$$\Delta = \frac{\omega_2 - \omega_1}{\omega_0} \quad (5.23)$$

where ω_1 and ω_2 are the passband edge frequencies where the response drops to -3 dB, and g_n for a maximally flat (Butterworth) filter is given by

$$g_n = 2 \sin\left(\frac{2n-1}{2N}\pi\right) \quad 1 \leq n \leq N \quad (5.24)$$

Now consider the N^{th} order BPF implemented with impedance transformers in Figure 5.2(b). The input impedances of both implementations are given by

$$Z_{in} = j\omega L_1 - \frac{j}{\omega C_1} + \frac{1}{j\omega C_2 - \frac{j}{\omega L_2} + \frac{1}{j\omega L_3 - \frac{j}{\omega C_3} + \dots}} \quad (5.25)$$

$$Z'_{in} = j\omega L'_1 - \frac{j}{\omega C'_1} + \frac{K_{12}^2}{j\omega L'_2 - \frac{j}{\omega C'_2} + \frac{K_{23}^2}{j\omega L'_3 - \frac{j}{\omega C'_3} + \dots}} \quad (5.26)$$

For both implementations to be equivalent, it can be shown that the following relationships must be satisfied:

$$L'_n = \begin{cases} L_1 & n = 1 \\ \left(\frac{K_{23}K_{45} \dots K_{n-1,n}}{K_{12}K_{34} \dots K_{n-2,n-1}}\right)^2 L_n & n \text{ odd}, n \neq 1 \\ \left(\frac{K_{12}K_{34} \dots K_{n-1,n}}{K_{23}K_{45} \dots K_{n-2,n-1}}\right)^2 C_n & n \text{ even} \end{cases} \quad (5.27)$$

$$C'_n = \begin{cases} C_1 & n = 1 \\ \left(\frac{K_{12}K_{34} \dots K_{n-2,n-1}}{K_{23}K_{45} \dots K_{n-1,n}} \right)^2 C_n & n \text{ odd}, n \neq 1 \\ \left(\frac{K_{23}K_{45} \dots K_{n-2,n-1}}{K_{12}K_{34} \dots K_{n-1,n}} \right)^2 L_n & n \text{ even} \end{cases}$$

$$\begin{cases} \frac{K_{12}K_{34} \dots K_{N-2,N-1}}{K_{23}K_{45} \dots K_{N-1,N}} = 1 & N \text{ odd} \\ \frac{K_{12}K_{34} \dots K_{N-1,N}}{K_{23}K_{45} \dots K_{N-2,N-1}} = R & N \text{ even} \end{cases} \quad (5.28)$$

It can be concluded from (5.28) that for an odd order there is more design freedom in choosing the load (and source) impedance (which was briefly discussed in Section 2.2.3.2).

The impedance inverter can be implemented as a magnetically coupled circuit (as shown in Figure 5.3), where the input impedance is

$$Z_{in} = j\omega L_1 + \frac{(\omega M)^2}{R + j\omega L_2} = j\omega L_1 + \frac{K^2}{R + j\omega L_2} \quad (5.29)$$

Thus,

$$K = \omega M \quad (5.30)$$

It is important to note that K is a constant but in (5.30) it is frequency dependent. Hence, we choose

$$K = \omega_0 M \quad (5.31)$$

and the BPF may be constructed with coupled resonators as shown in Figure 5.4.

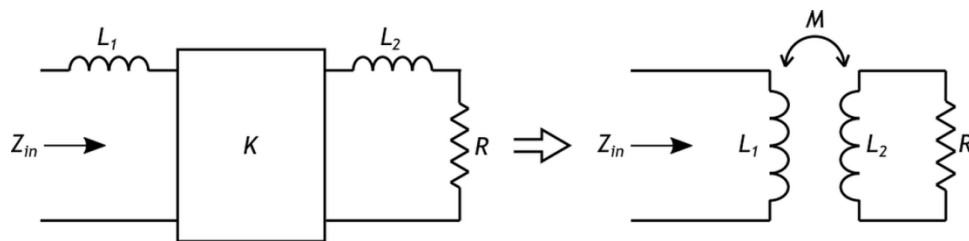


Figure 5.3 Impedance inverter implemented as an inductively coupled circuit.

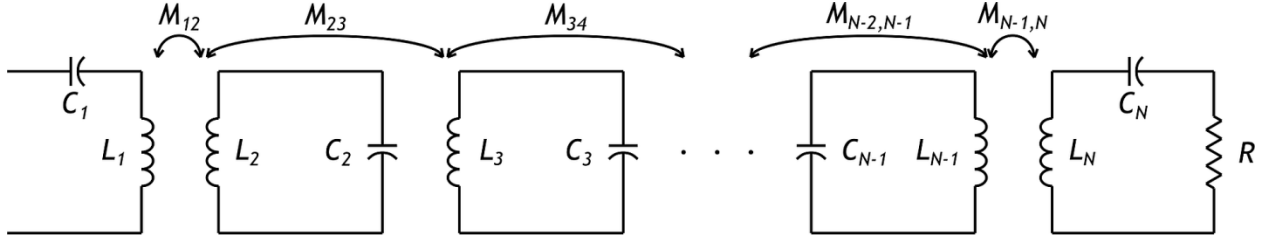


Figure 5.4 N^{th} order inductively coupled resonator synthesis of a BPF.

5.2 SHEATH HELIX EQUIVALENT CIRCUIT MODEL

5.2.1 QUARTER-WAVE SHEATH HELIX

The grounded sheath helix that was presented in Section 3.1.2 can be modeled by the circuit in Figure 5.5. From the voltage and current profiles given in Section 3.1.2, it can be deduced that the impedance at resonance is low since the voltage is low and the current is high at the input port. Hence, the sheath helix is represented by the series connection of an inductor L_0 and a capacitor C_0 . However, there is a large accumulation of charge at the open end that will couple to ground, which is represented by the shunt capacitor C_a .

A helix (with the parameters given in Table IV) was simulated in HFSS with a single lumped port between the ground plane and the helix [as shown in Figure 5.6(a)]. The imaginary Z_{11} parameters (i.e., input reactance) are given in Figure 5.6(b).

Table IV Sheath helix dimensions

Parameter	Description	Value
n	Number of turns	55
r	Radius	50 mm
a	Wire diameter	0.51 mm (24 AWG)
p	Pitch	3 mm

From Figure 5.5, the reactance of the helix is given by

$$X_{helix} = -\frac{\omega^2 L_0 C_0 - 1}{\omega(C_0 + C_a) \left(\omega^2 L_0 \frac{C_0 C_a}{C_0 + C_a} - 1 \right)} \quad (5.32)$$

L_0 can be derived from X_{helix} by evaluating the derivative of X_{helix} with respect to ω at $\omega_0 = 1/\sqrt{L_0 C_0}$

$$\left. \frac{dX_{helix}}{d\omega} \right|_{\omega=\omega_0} = 2L_0 \quad (5.33)$$

Then, C_0 can be calculated from

$$\omega_0^2 = \frac{1}{L_0 C_0} \quad (5.34)$$

Finally, C_a can be calculated from

$$\left(\frac{\omega_0}{\omega_a} \right)^2 = \frac{C_a}{C_0 + C_a} \quad (5.35)$$

where ω_a is the antiresonance frequency.

Using (5.32)-(5.35), the lumped circuit components are: $L_0 = 120.982 \mu\text{H}$, $C_0 = 6.248 \text{ pF}$, and $C_a = 5.781 \text{ pF}$. Figure 5.6(b) shows that the equivalent circuit and the simulated helix produce identical reactance profiles – confirming the validity of the circuit model.

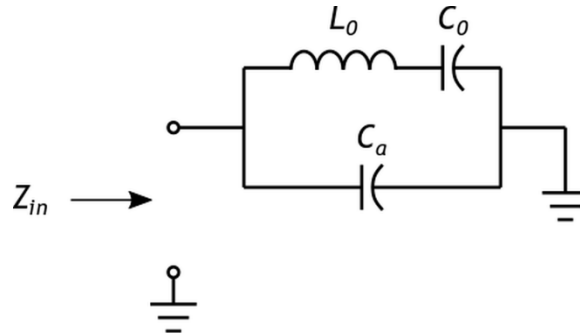


Figure 5.5 Equivalent lumped-element model of the quarter-wave sheath helix resonator.

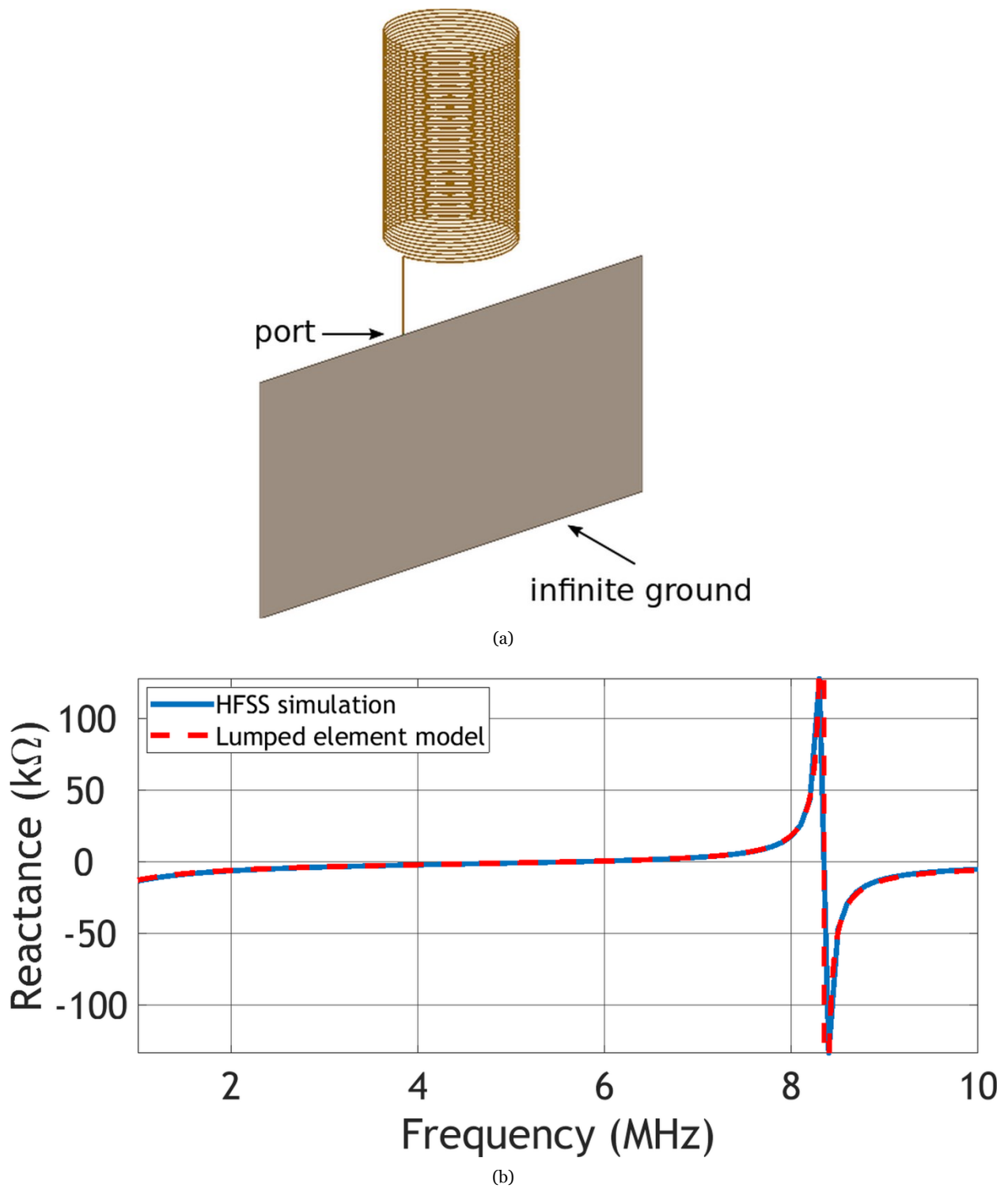
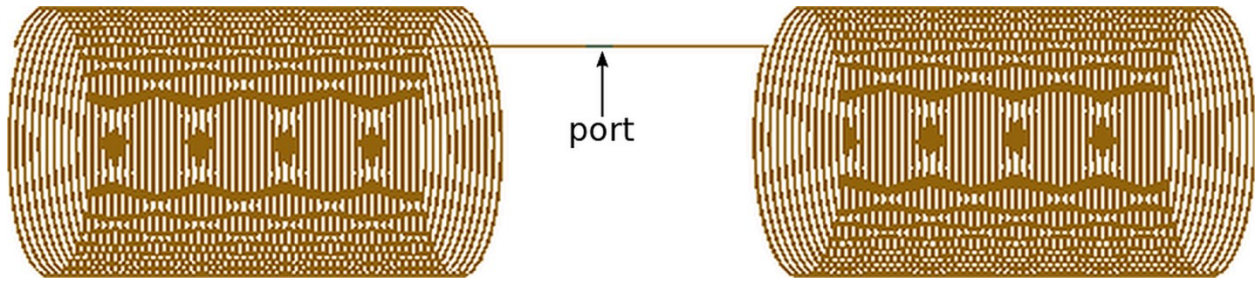


Figure 5.6 (a) HFSS model of the quarter-wave sheath helix resonator. (b) Reactances of the sheath helix and its equivalent lumped-element circuit.

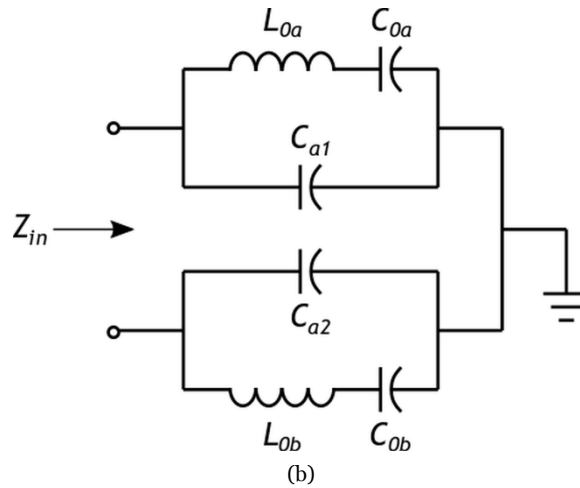
5.2.2 CAPACITIVELY COUPLED QUARTER-WAVE SHEATH HELICES

If two quarter-wave helices are connected, the resultant circuit will be a half-wave helix. Figure 5.7(a) depicts the structure with a port between the two helices. The dimensions of the two quarter-wave helices that compose the half-wave helix are the same as those listed in Table IV. To develop the equivalent lumped-element circuit model, consider the structure in Figure 5.6(a) again. Due to the infinite ground, image theory can be used to visualize the quarter-wave helix as two series-connected quarter-wave helices, i.e., a half-wave helix. By extension, the half-wave helix lumped-element circuit model should take the form shown in Figure 5.7(b), which is derived from Figure 5.5. The reactance of the half-wave helix is given in Figure 5.7(c). Using (5.32)-(5.35), the circuit parameters are: $L_0 = 251.574 \mu\text{H}$, $C_0 = 2.767 \text{ pF}$, and $C_a = 2.983 \text{ pF}$, and the reactance of the equivalent lumped-element circuit is plotted in Figure 5.7(c). Due to the symmetry of the structure, the lumped element values in Figure 5.7(b) are given by $L_{0a} = L_{0b} = L_0/2$, $C_{0a} = C_{0b} = 2C_0$, and $C_{a1} = C_{a2} = 2C_a$.

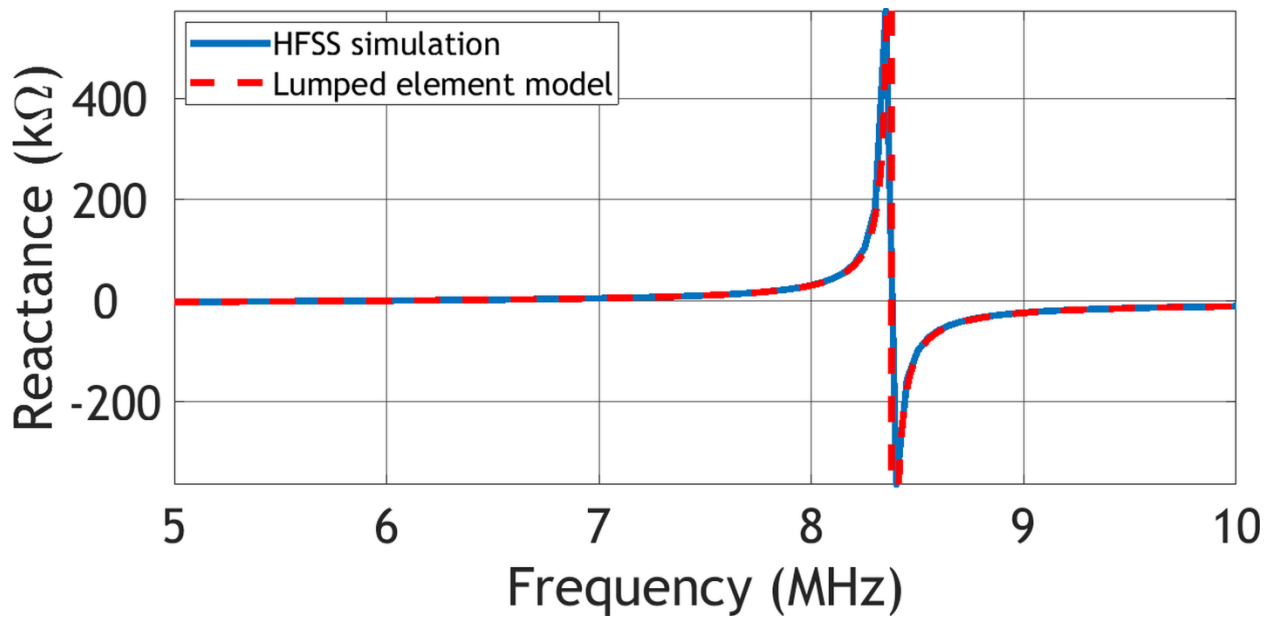
Now, if a capacitive discontinuity with a square area of 0.179 m^2 and a plate separation of 10 mm is placed between the two helices [as in Figure 5.8(a)], then the structure can be represented by Figure 5.8(b), where the circuit in Figure 5.7(c) was modified to include the capacitive discontinuity $C_d = 158.536 \text{ pF}$. Figure 5.8(c) shows that the reactance profile obtained from the HFSS structure is almost identical to that of the equivalent circuit model.



(a)

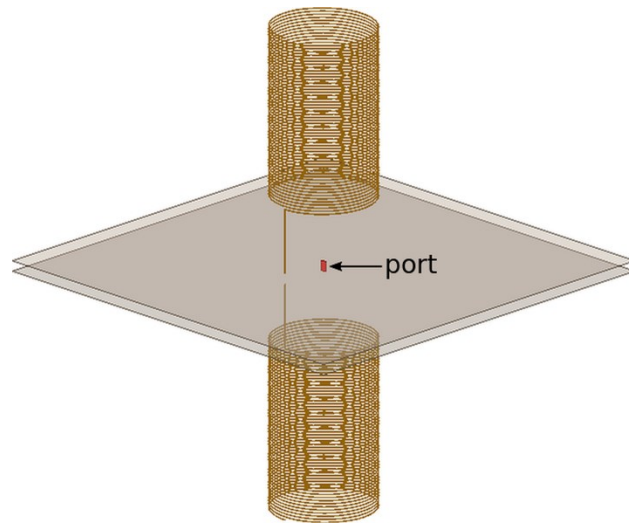


(b)

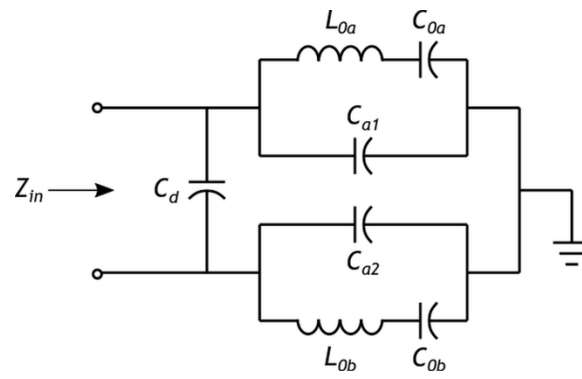


(c)

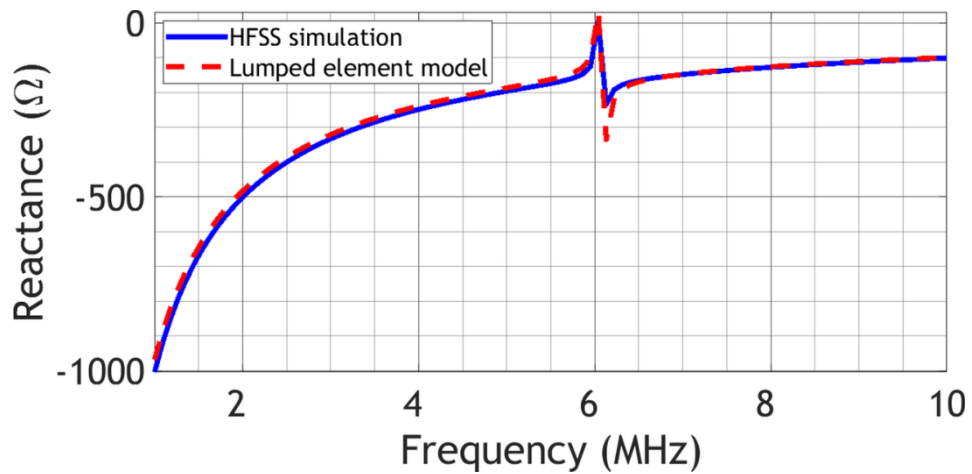
Figure 5.7 (a) HFSS model of the half-wave sheath helix resonator. (b) Equivalent lumped-element circuit of the half-wave sheath helix resonator. (c) Reactances of the sheath helix and its equivalent lumped-element circuit.



(a)



(b)



(c)

Figure 5.8 (a) HFSS model of the half-wave sheath helix resonator with a capacitive discontinuity. (b) Equivalent lumped-element circuit of the HFSS model. (c) Reactances of the HFSS model and the equivalent lumped-element circuit.

5.3 IMPLEMENTATION OF QUARTER WAVE SHEATH HELICES IN BPFs

5.3.1 SECOND ORDER BPF WITH 10% BANDWIDTH

The circuit diagram for a second order ($N = 2$) BPF with one sheath helix is shown in Figure 5.9. From Section 5.2.1, we let $L_1 = 120.982 \mu\text{H}$ and $C_1 = 6.248 \text{ pF}$ (note that C_a is disregarded because its effect is negligible at the resonant frequency). The design parameters for the second order BPF with 10% bandwidth are given in Table V.

Table V Design parameters of the second order BPF with 10% bandwidth

Parameter	Value	Parameter	Value
f_0	5.789 MHz	K [from (5.28)]	311 Ω
Δ	0.1	L_2 [from (5.21) and (5.27)]	120.982 μH
L_1	120.982 μH	C_2 [from (5.21) and (5.27)]	6.248 pF
C_1	6.248 pF	M [from (5.31)]	8.550 μH
R [from (5.20)]	311 Ω		

L_2 was split into two inductors: (a) a coil with a small inductance $L_{2a} = 1.94 \mu\text{H}$ that couples to the sheath helix and (b) a larger inductor $L_{2b} = 119.04 \mu\text{H}$ that is uncoupled from the helix. Table VI lists the parameters of L_{2a} . Since it is difficult to determine mathematically the relative positions of the sheath helix and the coil inductor that will achieve the proper mutual inductance M , a parametric sweep was performed from which it was determined that the coil inductor L_{2a} must be placed about 54 mm above the base of the sheath helix. The response of the filter is plotted in Figure 5.10 together with those of an equivalent ladder network BPF and a BPF using coupled resonators.

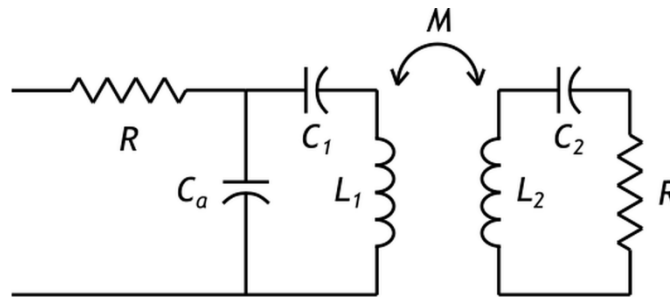


Figure 5.9 Circuit representation of a second order BPF with a sheath helix.

Table VI Coil inductor parameters for the second order BPF with 10% bandwidth

Parameter	Description	Value
n	Number of turns	3
r	Radius	49.235 mm
a	Wire diameter	0.51 mm (24 AWG)
p	Pitch	3 mm

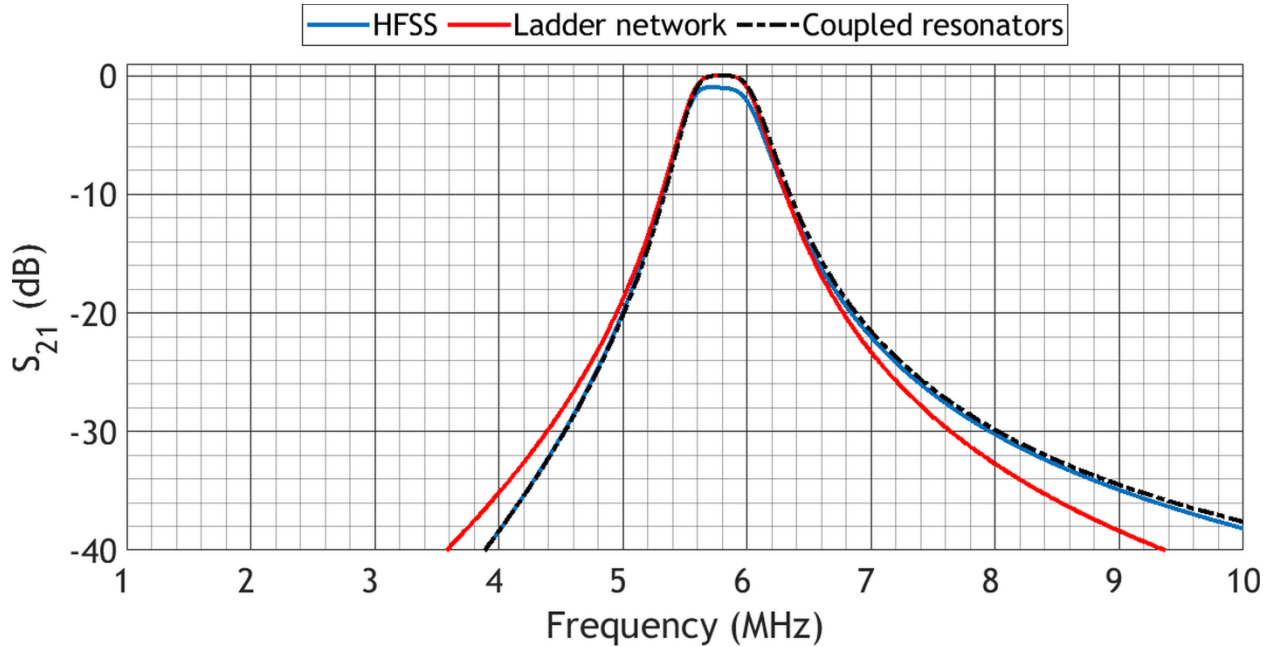


Figure 5.10 S_{21} parameters of the second order BPF with 10% bandwidth.

5.3.2 SECOND ORDER BPF WITH 50% BANDWIDTH

The design for the second order BPF with 50% bandwidth uses the same architecture shown in Figure 5.9, with the design parameters listed in Table VII. Once again, L_2 was split into two inductors: $L_{2a} = 67.51 \mu\text{H}$ (coupled to the sheath helix) and $L_{2b} = 53.47 \mu\text{H}$ (not coupled). When L_{2a} is 90 mm above the base of the sheath helix, the response is given by Figure 5.11.

Table VII Design parameters of the second order BPF with 50% bandwidth

Parameter	Value	Parameter	Value
f_0	5.789 MHz	K [from (5.28)]	1.556 k Ω
Δ	0.5	L_2 [from (5.21) and (5.27)]	120.982 μ H
L_1	120.982 μ H	C_2 [from (5.21) and (5.27)]	6.248 pF
C_1	6.248 pF	M [from (5.31)]	42.774 μ H
R [from (5.20)]	1.556 k Ω		

Table VIII Coil inductor parameters for the second order BPF with 50% bandwidth

Parameter	Description	Value
n	Number of turns	17
r	Radius	49.235 mm
a	Wire diameter	0.51 mm (24 AWG)
p	Pitch	0.62 mm

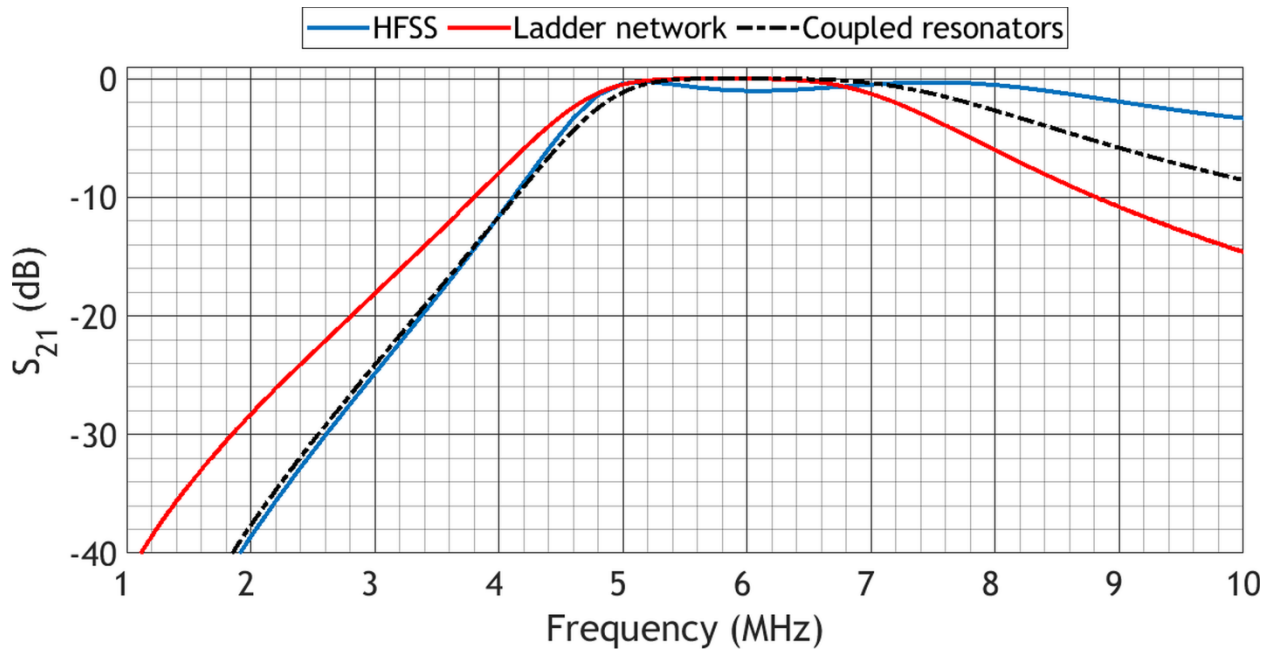


Figure 5.11 S_{21} parameters of the second order BPF with 50% bandwidth.

5.3.3 THIRD ORDER BPF WITH 10% BANDWIDTH

The circuit diagram for the third order ($N = 3$) BPF with two sheath helices separated by a capacitive discontinuity is shown in Figure 5.12. From Section 5.2.2, we let $L_{2a} = L_{2b} = L_2/2 = 125.787 \mu\text{H}$ and $C_{2a} = C_{2b} = 2C_2 = 5.534 \text{ pF}$ (again, C_a is disregarded in the design). As mentioned in Section 5.1, for an odd order there is freedom to choose R , hence we choose $R = 50 \Omega$. The design parameters for the third order BPF with 10% bandwidth are given in Table IX.

Table IX Design parameters of the third order BPF with 10% bandwidth

Parameter	Value	Parameter	Value
f_0	6.032 MHz	$K_{12} = K_{23}$ [from (5.27) and (5.28)]	154.32 Ω
Δ	0.1	$L_1 = L_3$ [from (5.21) and (5.27)]	13.19 μH
L_2	251.57 μH	$C_1 = C_3$ [from (5.21) and (5.27)]	52.77 pF
C_2	2.77 pF	$M_{12} = M_{23}$ [from (5.31)]	4.07 μH
R	50 Ω		

Again, L_1 and L_3 were split into $L_{1a} = L_{3a} = 1 \mu\text{H}$, which couple to the sheath helix, and $L_{1b} = L_{3b} = 12.19 \mu\text{H}$. In the HFSS simulation, L_{1a} and L_{3a} were simulated as coils with the dimensions listed in Table X. The responses of the filter and those of the ladder network and coupled resonator BPFs are plotted in Figure 5.13. It is noted that the passbands are similar in width, though shifted from the ladder network and coupled resonator implementations.

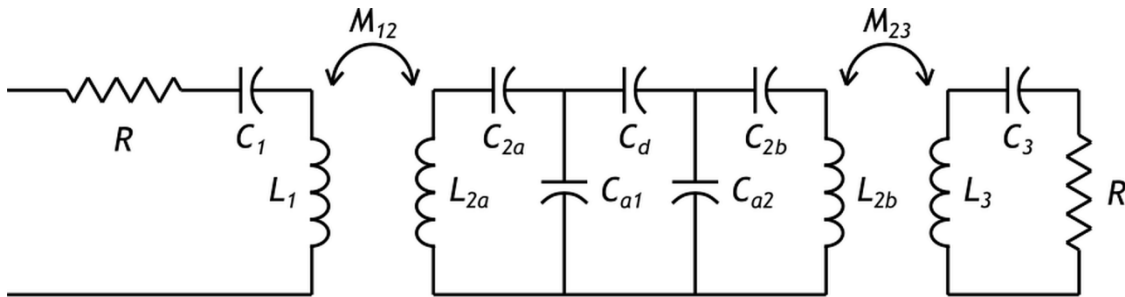


Figure 5.12 Circuit representation of the third order BPF with sheath helices and a capacitive discontinuity.

Table X Coil inductor parameters for the third order BPF with 10% bandwidth

Parameter	Description	Value
n	Number of turns	2
r	Radius	49.235 mm
a	Wire diameter	0.51 mm (24 AWG)
p	Pitch	3 mm

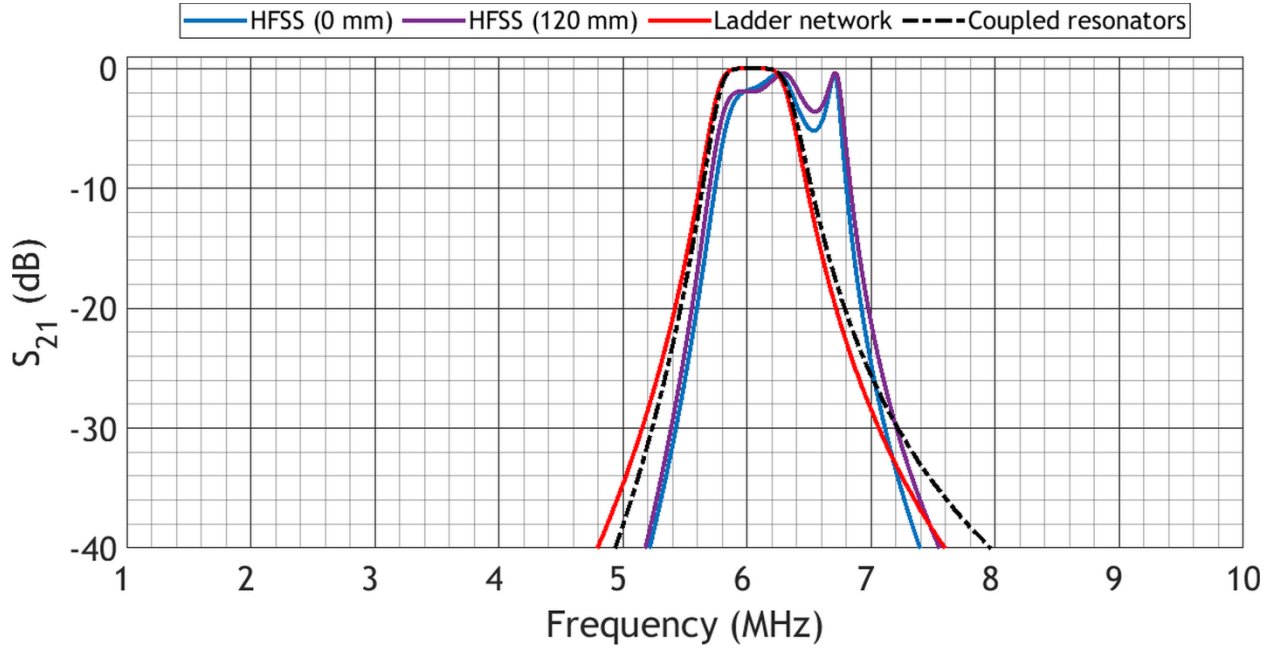


Figure 5.13 S_{21} parameters of the third order BPF with 10% bandwidth.

5.3.4 THIRD ORDER BPF WITH 50% BANDWIDTH

The design for the third order BPF with 50% bandwidth uses the same architecture shown in Figure 5.12, with the design parameters listed in Table XI. Once again, L_1 and L_3 were split into two inductors: $L_{1a} = L_{3a} = 67.51 \mu\text{H}$ (coupled to the sheath helices) and $L_{1b} = L_{3b} = 53.47 \mu\text{H}$. The dimensions for coils L_{1a} and L_{3a} are given in Table XII. Figure 5.14 plots the responses for the simulated, ladder network, and coupled resonator filters.

It is shown that the responses do not agree, which is due to C_a of the sheath helices. Also plotted in Figure 5.14 are the responses of the lumped-element model simulated in Keysight ADS with $C_a = 14.84 \text{ pF}$. When C_a is taken into account, a strong agreement is observed.

Table XI Design parameters of the third order BPF with 50% bandwidth

Parameter	Value	Parameter	Value
f_0	6.032 MHz	$K_{12} = K_{23}$ [from (5.27) and (5.28)]	345.06 Ω
Δ	0.1	$L_1 = L_3$ [from (5.21) and (5.27)]	2.64 μH
L_2	251.57 μH	$C_1 = C_3$ [from (5.21) and (5.27)]	263.85 pF
C_2	2.77 pF	$M_{12} = M_{23}$ [from (5.31)]	9.11 μH
R	50 Ω		

Table XII Coil inductor parameters for the third order BPF with 50% bandwidth

Parameter	Description	Value
n	Number of turns	3
r	Radius	49.235 mm
a	Wire diameter	0.51 mm (24 AWG)
p	Pitch	0.65 mm

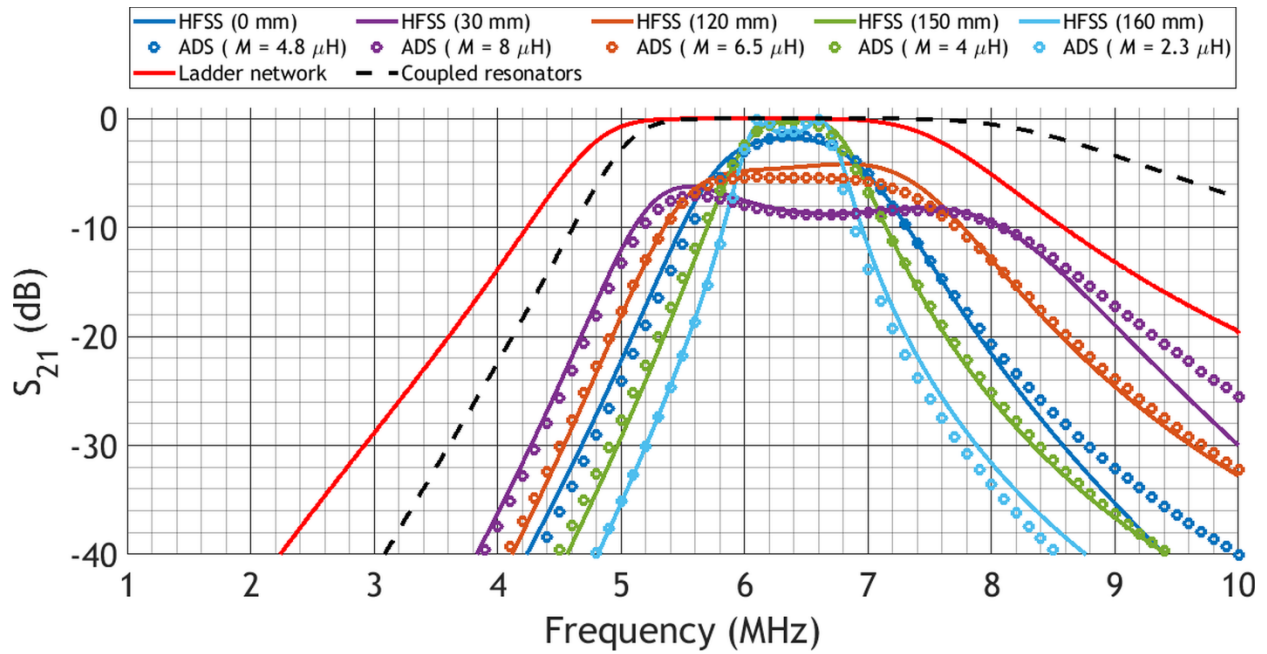


Figure 5.14 S_{21} parameters of the third order BPF with 50% bandwidth.

Chapter 6 Conclusion

This thesis has explored a method of power and data transmission that uses only a single conductor with no ground return. To facilitate this study, a few fundamental concepts on inductive and resonant WPT were developed in order to demonstrate the superiority of resonant WPT over traditional inductive WPT. Moreover, the benefits of a relay in increasing transfer distance and design flexibility were discussed in the specific case of a 3-resonator system. The last introductory concept was that of the sheath helix, which forms the most crucial element of the single-conductor system presented here.

The capability of the proposed single-conductor system to be used as a communication channel was studied. OOK modulation was used due to its simplicity, which was then extended to the modified Miller line code widely used in RFID and NFC communication. The results showed that data rates in the hundreds of kilobits per second are possible with the chosen modulation schemes, rendering the system suitable for RFID and NFC application. However, it was shown that communication at higher data rates is severely limited by the bandwidth of the system.

In order to increase the data rate for the channel, two methods were investigated:

1. Ripple voltage reduction: In addition to the ISI introduced by the frequency-selective nature of the single-conductor system, higher data rates suffer from increased ripple voltage that hinders the reliable reception of data. To combat this, a new design criterion was developed for the asynchronous receiver. The criterion relies on distorting the incoming signal by reducing the cutoff frequency of the receiver's LPF, which in turn reduces the ripple voltage. Simulation results demonstrated that this new criterion significantly improves the communication performance by decreasing the BER, thereby allowing higher data rates to be used. An additional consequence of this criterion is the reliable detection of messages with a lower modulation index, which is theorized to be highly beneficial to SWIPT and wirelessly powered backscatter communication.
2. System bandwidth enlargement: By modeling the sheath helix as a resonant lumped-element circuit, it was possible to apply well-known band-pass filter design techniques for Butterworth filters, in which bandwidth is a design parameter. This provides a framework for the design of single-conductor communication systems with a bandwidth requirement.

Mathematical relationships were derived to convert from the ladder-network synthesis to the inductively coupled resonator synthesis. These equations were utilized to design four single-conductor systems employing sheath helices in HFSS: two second-order systems with 10% and 50% bandwidths and two third-order systems with 10% and 50% bandwidths. Simulation results for the structures closely agreed with simulation results performed in Keysight ADS for the equivalent lumped-element circuits. These results demonstrated how easy it is to design single-conductor systems with desired bandwidths for WIPT purposes.

6.1 FUTURE WORK

This work opens up several directions for further investigation:

- Chapter 4 presented results showing the potential of the single-conductor system for use with RFID sensors. However, the results were produced only with an SDR. Hence, a practical implementation with an RFID sensor should be performed to confirm the results.
- Chapter 4 also introduced a new receiver design, which was only implemented as an SDR. Again, a practical implementation to confirm the results of the simulation is desired. Further, it was discussed that the design may be highly applicable to SWIPT and wirelessly powered backscatter communication –applications that warrant further study, both theoretically and practically.
- It was shown in literature and this thesis that a wire or a capacitive discontinuity placed between the sheath helices supports WPT and data transfer. It is of interest to test other conductive structures of arbitrary shapes and sizes as this could inspire new applications. A related study should explore the transmission range enabled by this technology by using longer conductors between the sheath helices. Studying the shape, size, and length of the conductor is of interest because they will change the structure of the overall system and thus affect its resonant frequency, bandwidth, and gain.
- As with any transmission medium, multiple-input multiple-output (MIMO) should be applied to it to study its potential for use in data and power networks. As with the shape, size, and length of the conductor, multiple transmitters and receivers will affect the resonant frequency, bandwidth, and gain of the overall system.
- In order to exploit existing band-pass filter architectures, Chapter 5 used a simple circuit model for the helix. However, it was seen that the model is imperfect, which resulted in a discrepancy between the design criteria and the actual simulation results. A more accurate model would enable a better design such that the criteria are met.

- Chapter 5 only provided simulation results of the proposed BPF design method, which should be confirmed by measurement. Moreover, the BPF design method relied on equal source and load impedances, which may not always be possible. The literature cited in this work provides a method to design systems that are not bound by this restriction and that should be implemented with the single-conductor system.
- This thesis looked into two methods to increase the data rates: an improved envelope detector for ASK and bandwidth enlargement of the system. Another popular method that should be investigated is equalization.

References

- [1] R. S. Elliott, “The history of electromagnetics as Hertz would have known it,” *IEEE Transactions on Microwave Theory and Techniques*, vol. 36, no. 5, pp. 806–823, 1988.
- [2] M. Mitolo and R. Araneo, “A brief history of electromagnetism,” *IEEE Industry Applications Magazine*, vol. 25, no. 2, pp. 7–11, 2019.
- [3] D. M. Pozar, *Microwave Engineering*, 4th ed. Hoboken, NJ: Wiley, 2012.
- [4] “Guglielmo Marconi – Nobel Lecture,” *NobelPrize.org*. <https://www.nobelprize.org/prizes/physics/1909/marconi/lecture/> (accessed Mar. 31, 2020).
- [5] N. Tesla, “System of transmission of electrical energy,” U.S. Patent 645,576, Mar. 20, 1900.
- [6] X. Lu, P. Wang, D. Niyato, D. I. Kim, and Z. Han, “Wireless charging technologies: fundamentals, standards, and network applications,” *IEEE Communications Surveys*, vol. 18, no. 2, pp. 1413–1452, 2016.
- [7] W. C. Brown, “The history of power transmission by radio waves,” *IEEE Transactions on Microwave Theory and Techniques*, vol. 32, no. 9, pp. 1230–1242, 1984.
- [8] A. Kurs, A. Karalis, R. Moffatt, J. D. Joannopoulos, P. Fisher, and M. Soljačić, “Wireless power transfer via strongly coupled magnetic resonances,” *Science*, vol. 317, no. 5834, pp. 83–86, 2007.
- [9] Wireless Power Consortium, “About the WPC,” *Wireless Power Consortium*, 2018. <https://www.wirelesspowerconsortium.com/> (accessed Apr. 02, 2020).
- [10] R. McCormick, “Former wireless charging rivals join forces as new AirFuel Alliance,” *The Verge*, Nov. 03, 2015. <https://www.theverge.com/2015/11/3/9666960/airfuel-alliance-formed-a4wp-pma-wireless-charging> (accessed Apr. 02, 2020).
- [11] T. Ong, “Qi reigns as the standard for wireless charging after Powermat joins WPC,” *The Verge*, Jan. 08, 2018. <https://www.theverge.com/2018/1/8/16862244/powermat-wireless-power-consortium-qi-charging> (accessed Apr. 02, 2020).
- [12] M. Roberti, “The History of RFID Technology,” *RFID Journal*, 2005. <https://www.rfidjournal.com/articles/view?1338> (accessed Apr. 02, 2020).
- [13] B. Clerckx, A. Costanzo, A. Georgiadis, and N. Borges Carvalho, “Toward 1G mobile power networks: RF, signal, and system designs to make smart objects autonomous,” *IEEE Microwave Magazine*, vol. 19, no. 6, pp. 69–82, 2018.
- [14] A. Sharma, A. T. Hoang, and M. S. Reynolds, “Long-range battery-free UHF RFID with a

- single wire transmission line,” *IEEE Sensors Journal*, vol. 17, no. 17, pp. 5687–5693, 2017.
- [15] S. M. Amjadi and K. Sarabandi, “A compact single conductor transmission line launcher for telemetry in borehole drilling,” *IEEE Transactions on Geoscience and Remote Sensing*, vol. 55, no. 5, pp. 2674–2681, 2017.
- [16] F. C. Domingos, “Wireless power transmission topology using capacitively coupled open-ended helical resonators,” M.S. thesis, Dept. of Elec. and Comp. Eng., Univ. of Alberta, Edmonton, Canada, 2019.
- [17] S. V. de C. de Freitas, “Capacitive resonant single-conductor system for wireless power transfer to devices with metallic embodiments,” M.S. thesis, Dept. of Elec. and Comp. Eng., Univ. of Alberta, Edmonton, Canada, 2019.
- [18] F. Cezar Domingos, S. Vital De Campos De Freitas, R. Mirzavand, and P. Mousavi, “Capacitively Coupled Resonators for Misalignment-Tolerant Wireless Charging through Metallic Cases,” *2019 IEEE Wireless Power Transfer Conference*, pp. 174–177, 2019.
- [19] S. Vital De Campos De Freitas, F. Cezar Domingos, R. Mirzavand, and P. Mousavi, “Capacitive Resonant System to Charge Devices with Metallic Embodiments,” *2019 IEEE Wireless Power Transfer Conference*, pp. 347–350, 2019.
- [20] C. R. Paul, *Inductance: Loop and Partial*. Hoboken, NJ: Wiley, 2010.
- [21] J. A. Edminister and M. Nahvi, *Schaum’s Outline of Electromagnetics*, 4th ed. New York, NY: McGraw Hill Education, 2014.
- [22] J. D. Irwin and R. M. Nelms, *Basic Engineering Circuit Analysis*, 10th ed. Hoboken, NJ: Wiley, 2011.
- [23] A. P. Sample, S. Member, D. A. Meyer, S. Member, and J. R. Smith, “Analysis, experimental results, and range adaptation of magnetically coupled resonators for wireless power transfer,” *IEEE Transactions on Industrial Electronics*, vol. 58, no. 2, pp. 544–554, 2011.
- [24] D. Seo, “Comparative analysis of two- and three-coil WPT systems based on transmission efficiency,” *IEEE Access*, vol. 7, pp. 151962–151970, 2019.
- [25] P. J. Abatti, C. M. de Miranda, M. A. P. da Silva, and S. F. Pichorim, “Analysis and optimisation of three-coil wireless power transfer systems,” *IET Power Electronics*, vol. 11, no. 1, pp. 68–72, 2018.
- [26] M. Kiani, U. Jow, and M. Ghovanloo, “Design and optimization of a 3-coil inductive link for efficient wireless power transmission,” *IEEE Transactions on Biomedical Circuits and Systems*, vol. 5, no. 6, pp. 579–591, 2011.

- [27] R. Huang, B. Zhang, D. Qiu, and Y. Zhang, “Frequency splitting phenomena of magnetic resonant coupling wireless power transfer,” *IEEE Transactions on Magnetics*, vol. 50, no. 11, pp. 1–4, 2014.
- [28] W.-Q. Niu, J.-X. Chu, W. Gu, and A. Shen, “Exact analysis of frequency splitting phenomena of contactless power transfer systems,” *IEEE Transactions on Circuits and Systems I: Regular Papers*, vol. 60, no. 6, pp. 1670–1677, 2013.
- [29] J.-S. Hong and M. J. Lancaster, *Microstrip Filter for RF/Microwave Application*. Hoboken, NJ: Wiley, 2001.
- [30] Z.-J. Liao, Y. Sun, Z.-H. Ye, C.-S. Tang, and P.-Y. Wang, “Resonant analysis of magnetic coupling wireless power transfer systems,” *IEEE Transactions on Power Electronics*, vol. 34, no. 6, pp. 5513–5523, 2019.
- [31] G. Goubau, “Surface waves and their application to transmission lines,” *Journal of Applied Physics*, vol. 21, no. 11, pp. 1119–1128, 1950.
- [32] A. F. Harvey, “Periodic and guiding structures at microwave frequencies,” *IRE Transactions on Microwave Theory and Techniques*, vol. 8, no. 1, pp. 30–61, 1960.
- [33] H. C. Pocklington, “Electrical oscillations in wires,” *Proceedings of the Cambridge Philosophical Society*, vol. 9, no. 7, 1898.
- [34] N. Tesla, “Apparatus for transmitting electrical energy,” U.S. Patent 1,119,732, Dec. 01, 1914.
- [35] K. L. Corum and J. F. Corum, “RF coils, helical resonators and voltage magnification by coherent spatial modes,” in *5th International Conference on Telecommunications in Modern Satellite, Cable and Broadcasting Service. TELSIKS 2001. Proceedings of Papers (Cat. No.01EX517)*, 2001, pp. 339–348.
- [36] C. A. Balanis, *Antenna Theory: Analysis and Design*, 4th ed. Hoboken, NJ: Wiley, 2016.
- [37] T. Sun, X. Xie, and Z. Wang, *Wireless Power Transfer for Medical Microsystems*. New York, NY: Springer, 2013.
- [38] A. G. Kandoian and W. Sichak, “Wide-frequency-range tuned helical antennas and circuits,” in *1958 IRE International Convention Record*, 1953, pp. 42–47.
- [39] C. M. de Miranda and S. F. Pichorim, “Self-resonant frequencies of air-core single-layer solenoid coils calculated by a simple method,” *Electrical Engineering*, vol. 97, pp. 57–64, 2014.
- [40] C. M. de Miranda and S. F. Pichorim, “Self-resonant frequencies, standing waves, and impedance behavior of air-core helical solenoidal coil,” in *2015 International conference on electromagnetics in advanced applications*, 2015.

- [41] C. W. Van Neste, R. Hull, J. E. Hawk, A. Phani, M. J. Unsworth, and T. Thundat, “Electrical excitation of the local earth for resonant, wireless energy transfer,” *Wireless Power Transfer*, vol. 3, no. 2, pp. 117–125, 2016.
- [42] C. W. Van Neste *et al.*, “Single-contact transmission for the quasi-wireless delivery of power over large surfaces,” *Wireless Power Transfer*, vol. 1, no. 2, pp. 75–82, 2014.
- [43] T. Sun, X. Xie, G. Li, Y. Gu, X. Li, and Z. Wang, “A wireless energy link for endoscopy with end-fire helix emitter and load-adaptive power converter,” in *2010 IEEE Asia Pacific Conference on Circuits and Systems*, 2010, pp. 32–35.
- [44] S. V. de C. de Freitas, A. Maunder, F. C. Domingos, and P. Mousavi, “Method and system for wireless and single-conductor power and data transmission,” in *IEEE Wireless Power Transfer Conference (WPTC)*, 2016.
- [45] S. V. de C. de Freitas, F. C. Domingos, R. Mirzavand, A. Maunder, P. Naseri, and P. Mousavi, “A novel method for data and power transmission through metallic structures,” *IEEE Transactions on Industrial Electronics*, vol. 64, no. 5, pp. 4027–4036, 2017.
- [46] M. Rao and K. Sarabandi, “A tunable, high-gain, very low-profile composite monopole antenna for low-frequency applications,” *IEEE Transactions on Antennas and Propagation*, vol. 66, no. 7, pp. 3286–3294, 2018.
- [47] A. S. Sedra and K. C. Smith, *Microelectronic Circuits*, 5th ed. New York, NY: Oxford University Press, 2004.
- [48] N. S. Nise, *Control Systems Engineering*, 6th ed. Hoboken, NJ: Wiley, 2011.
- [49] M. Moher and S. S. Haykin, *Introduction to Analog and Digital Communications*, 2nd ed. Hoboken, NJ: Wiley, 2007.
- [50] R. Shelton and A. Adkins, “Noise bandwidth of common filters,” *IEEE Transactions on Communication Technology*, vol. 18, no. 6, pp. 828–830, 1970.
- [51] “Identification Cards – Contactless Integrated Circuit Cards – Proximity Cards – Part 2: Radio Frequency Power and Signal Interface,” ISO/IEC 14443-2, 2016.
- [52] “Near Field Communication - Interface and Protocol (NFCIP-1),” ECMA-340, 2013.
- [53] P. Grover and A. Sahai, “Shannon meets Tesla: wireless information and power transfer,” in *2010 IEEE International Symposium on Information Theory*, 2010, pp. 2363–2367.
- [54] Wireless Power Consortium, “The Qi Wireless Power Transfer System Power Class 0 Specification Parts 1 and 2: Interface Definitions,” 2017.
- [55] R. Correia and N. B. Carvalho, “Ultrafast backscatter modulator with low-power consumption and wireless power transmission capabilities,” *IEEE Microwave and Wireless Components Letters*, vol. 27, no. 12, pp. 1152–1154, 2017.

- [56] K. Finkenzeller, *RFID Handbook: Fundamentals and Applications in Contactless Smart Cards and Identification*, 2nd ed. Chichester, England: Wiley, 2003.
- [57] J. Besnoff, M. Abbasi, and D. S. Ricketts, “High data-rate communication in near-field RFID and wireless power using higher order modulation,” *IEEE Transactions on Microwave Theory and Techniques*, vol. 64, no. 2, pp. 401–413, 2016.
- [58] B. Clerckx, R. Zhang, R. Schober, D. W. K. Ng, D. I. Kim, and H. V. Poor, “Fundamentals of wireless information and power transfer: from RF energy harvester models to signal and system designs,” *IEEE Journal on Selected Areas in Communications*, vol. 37, no. 1, pp. 4–33, 2019.
- [59] M. S. Trotter, J. D. Griffin, and G. D. Durgin, “Power-optimized waveforms for improving the range and reliability of RFID systems,” in *2009 IEEE International Conference on RFID*, 2009, pp. 80–87.
- [60] A. Collado and A. Georgiadis, “Optimal waveforms for efficient wireless power transmission,” *IEEE Microwave and Wireless Components Letters*, vol. 24, no. 5, pp. 354–356, 2014.
- [61] A. S. Boaventura and N. B. Carvalho, “Maximizing DC power in energy harvesting circuits using multisine excitation,” in *IEEE MTT-S International Microwave Symposium Digest*, 2011, pp. 1–4.
- [62] M. Rajabi, N. Pan, S. Claessens, S. Pollin, and D. Schreurs, “Modulation techniques for simultaneous wireless information and power transfer with an integrated rectifier-receiver,” *IEEE Transactions on Microwave Theory and Techniques*, vol. 66, no. 5, pp. 2373–2385, 2018.
- [63] B. Clerckx, Z. Bayani Zawawi, and K. Huang, “Wirelessly powered backscatter communications: waveform design and SNR-energy tradeoff,” *IEEE Communications Letters*, vol. 21, no. 10, pp. 2234–2237, 2017.
- [64] D. I. Kim, J. H. Moon, and J. J. Park, “New SWIPT using PAPR: how it works,” *IEEE Wireless Communications Letters*, vol. 5, no. 6, pp. 672–675, 2016.
- [65] S. Claessens, N. Pan, D. Schreurs, and S. Pollin, “Multitone FSK modulation for SWIPT,” *IEEE Transactions on Microwave Theory and Techniques*, vol. 67, no. 5, pp. 1665–1674, 2019.
- [66] N. Shariati, J. R. Scott, D. Schreurs, and K. Ghorbani, “Multitone excitation analysis in RF energy harvesters—Considerations and limitations,” *IEEE Internet of Things Journal*, vol. 5, no. 4, pp. 2804–2816, 2018.
- [67] C. R. Valenta, M. M. Morys, and G. D. Durgin, “Theoretical energy-conversion efficiency

- for energy-harvesting circuits under power-optimized waveform excitation,” *IEEE Transactions on Microwave Theory and Techniques*, vol. 63, no. 5, pp. 1758–1767, 2015.
- [68] R. M. Fano, “Theoretical limitations on the broad-band matching of arbitrary impedances,” *Journal of the Franklin Institute*, vol. 249, no. 1, pp. 57–83, 1950.
- [69] G. L. Matthaei, L. Young, and E. M. T. Jones, *Microwave Filters, Impedance-Matching Networks, and Coupling Structures*. Dedham, MA: Artech House Books, 1980.
- [70] I. Awai, “Design theory of wireless power transfer system based on magnetically coupled resonators,” in *2010 IEEE International Conference on Wireless Information Technology and Systems, ICWITS 2010*, 2010, pp. 10–13.
- [71] B. Luo, S. Wu, and N. Zhou, “Flexible design method for multi-repeater wireless power transfer system based on coupled resonator bandpass filter model,” *IEEE Transactions on Circuits and Systems I: Regular Papers*, vol. 61, no. 11, pp. 3288–3297, 2014.
- [72] J. Besnoff and D. S. Ricketts, “Wide bandwidth for high-speed communication in mid-range, resonant WPT and RFID systems,” in *2015 European Microwave Conference (EuMC)*, 2015, pp. 147–150.
- [73] K. Ding, Y. Yu, and H. Lin, “Analysis of RWPT relays for intermediate-range simultaneous wireless information and power transfer system,” *Progress in Electromagnetics Research Letters*, vol. 57, pp. 111–116, 2015.
- [74] J. S. McLean, “Balancing networks for symmetric antennas - I: classification and fundamental operation,” *IEEE Transactions on Electromagnetic Compatibility*, vol. 44, no. 4, pp. 503–514, 2002.

Appendix A. Isolation Transformers

The measurements performed on the single-conductor system investigated in this thesis produced fickle and unreliable results. It was observed in some instances that touching or even approaching the measurement devices or their coaxial cable connections caused the measurement to change. The reason for this can be explained by considering the structure in Figure A.1(a). The sheath helix connected to a conductive plate can be viewed as an inductively-loaded monopole antenna with an electrically small ground plane. Feeding it directly with a coaxial cable will cause an undesired current I_2 to flow on the outside of the coaxial cable because it provides a path to ground with smaller impedance, thus producing unbalanced currents in the antenna, I and I_1 (where $I_1 < I$). As a result, the open-circuited end of the sheath helix will couple to the outside of the coaxial cable instead of to its ground plane, unintentionally incorporating the measurement devices, their connections, and anything that is in proximity to them into the antenna. To suppress the current flowing outside the coaxial cable, a simple isolation transformer may be used to balance the currents flowing in the monopole antenna, as shown in Figure A.1(b), thereby producing one half of the single-conductor system presented in this thesis [46], [74]. However, it was shown in [46] that a single isolation transformer was insufficient to stabilize the response and instead a cascade connection of several transformers was required.

Tests performed by the research group showed that more stable measurements, which agree with simulation, are obtained by the addition of a cascade connection of several isolation transformers at the input and output of the system, as in [46]. Figure A.2 shows the frequency response of the channel with up to five transformers at the input and output. It is clear that four transformers at each port are sufficient to stabilize the measured response.

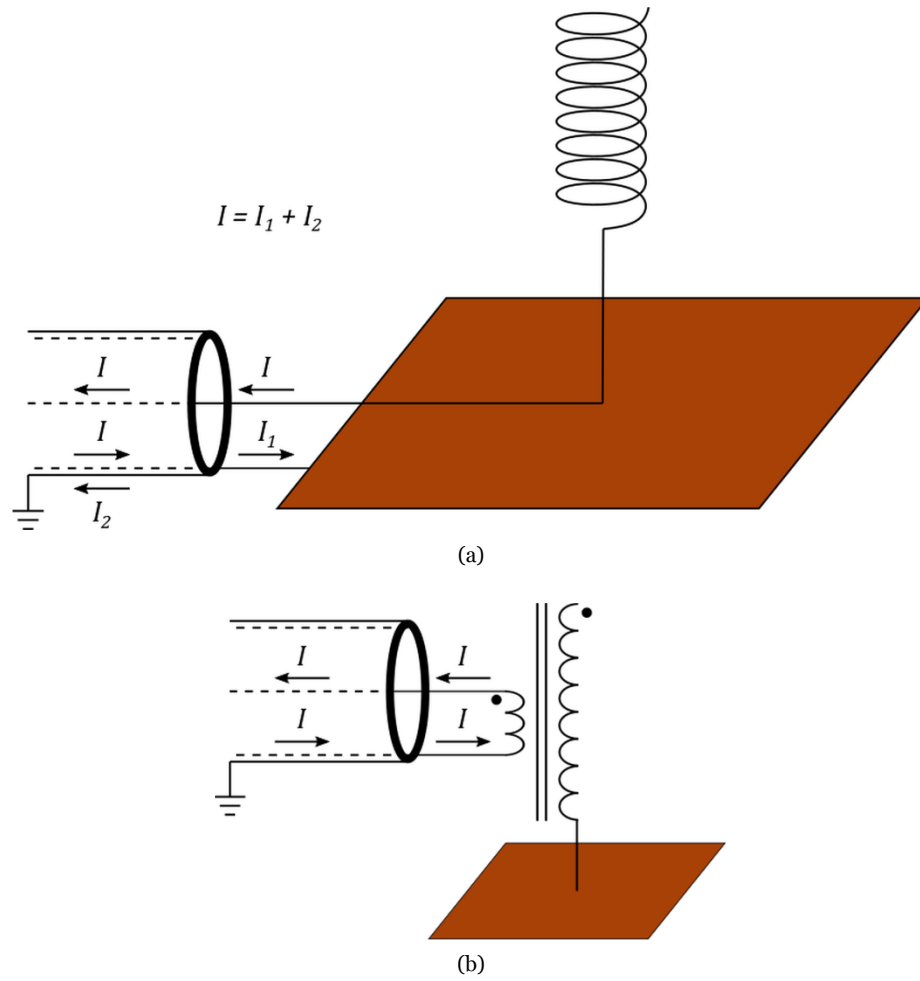


Figure A.1 (a) An inductively-loaded monopole antenna with an electrically small ground plane fed directly by a coaxial cable.
 (b) An inductively-loaded monopole fed with an isolation transformer.

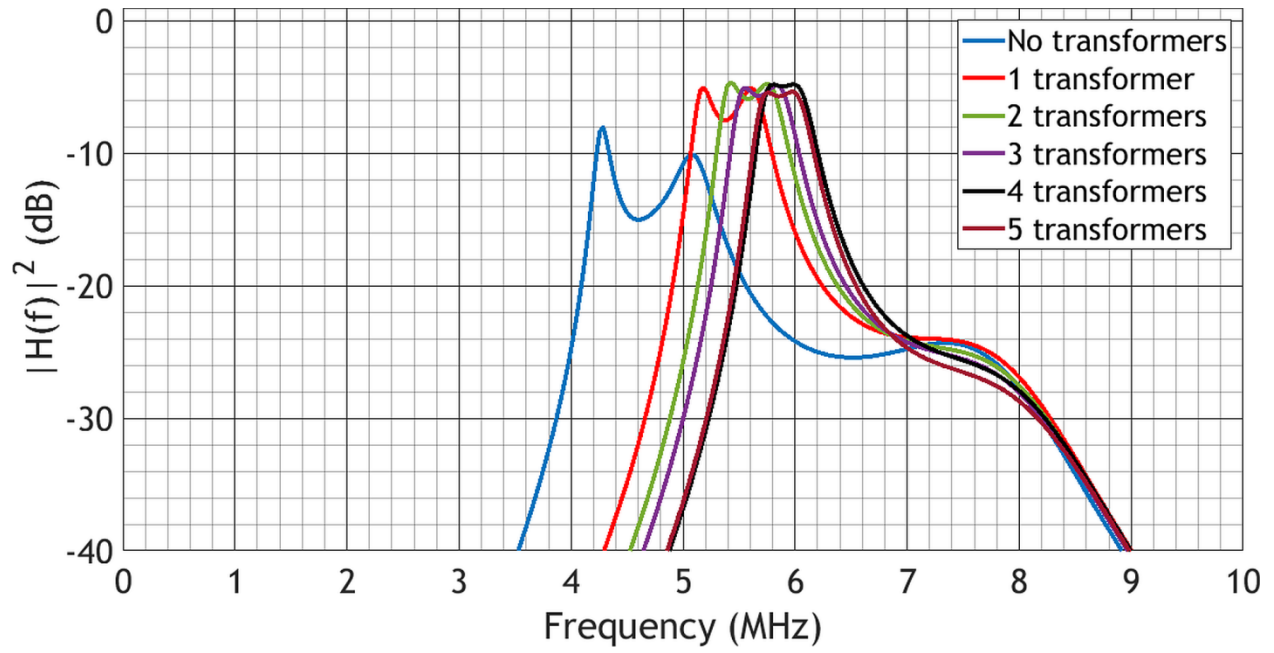


Figure A.2 Measured channel response with up to five transformers at each port.

Appendix B. Probability of Error for the Asynchronous Detection of OOK Data

AWGN is modelled by a circularly Gaussian (i.e., complex) distribution with mean μ (complex value) and variance $\sigma^2 = N_0$ as $N \sim \mathcal{CN}(\mu, N_0)$. Individually, the x and y components of the noise are represented by Gaussian variables as $N_x \sim \mathcal{N}(\mu_x, N_0/2)$ and $N_y \sim \mathcal{N}(\mu_y, N_0/2)$, where $\mu_x, \mu_y \in \mathbb{R}$. The individual distributions can be mathematically expressed as

$$f_X(x) = \frac{1}{\sqrt{\pi N_0}} e^{-\frac{(x-\mu_x)^2}{N_0}} \quad f_Y(y) = \frac{1}{\sqrt{\pi N_0}} e^{-\frac{(y-\mu_y)^2}{N_0}} \quad (\text{B.1})$$

For a signal corrupted by AWGN, the received signal passband is given by

$$\begin{aligned} r(t) &= \sum_k s_k g(t - kT_s) \cos(\omega_0 t) + n(t) \\ &= \sum_k s_k g(t - kT_s) \cos(\omega_0 t) + n_x(t) \cos(\omega_0 t) + n_y(t) \sin(\omega_0 t) \end{aligned} \quad (\text{B.2})$$

where s_k is the k^{th} symbol and $g(t - kT_s)$ is the pulse shape sent at the k^{th} symbol interval T_s . The envelope of this signal is given by

$$e(t) = \sqrt{\left[\sum_k s_k g(t - kT_s) + n_x(t) \right]^2 + [n_y(t)]^2} \quad (\text{B.3})$$

and in terms of random variables

$$E = \sqrt{(S_k + N_x)^2 + N_y^2} \quad (\text{B.4})$$

For an OOK signal, two cases must be considered: $S_k = 0$ and $S_k = A$.

$S_k = 0$:

The probability of error is given by $p_{e|0} = P(E > z)$ where z is a threshold value above which the receiver detects the symbol as A . The probability of error can be rewritten as

$$p_{e|0} = P\left(\sqrt{N_x^2 + N_y^2} > z\right) = P(N_x^2 + N_y^2 > z^2) \quad (\text{B.5})$$

where $N_x^2 + N_y^2 > z^2$ is simply the area S outside a circle with radius z and centred at the origin. Then

$$p_{e|0} = \iint_S f_{XY}(x, y) dx dy \quad (\text{B.6})$$

Since the x and y component of noise are independent of each other, their joint probability distribution function may be re-expressed as the product of their individual probability distribution functions and (B.6) becomes

$$p_{e|0} = \iint_S \frac{1}{\pi N_0} e^{-\frac{x^2+y^2}{N_0}} dx dy \quad (\text{B.7})$$

Changing from rectangular to polar coordinates

$$\begin{aligned} p_{e|0} &= \int_{\rho=z}^{\infty} \int_{\phi=0}^{2\pi} \frac{1}{\pi N_0} e^{-\frac{\rho^2}{N_0}} \rho d\phi d\rho \\ &= \int_z^{\infty} \frac{2\rho}{N_0} e^{-\frac{\rho^2}{N_0}} d\rho \end{aligned} \quad (\text{B.8})$$

$S_k = A$:

In this case, the mean of the x component has shifted to $\mu_x = A$ and hence (B.7) becomes

$$p_{e|1} = \iint_S \frac{1}{\pi N_0} e^{-\frac{(x-A)^2+y^2}{N_0}} dx dy \quad (\text{B.9})$$

and S is now the area defined by $\sqrt{(A + N_x)^2 + N_y^2} < z$. Again, converting to polar coordinates

$$\begin{aligned} p_{e|1} &= \int_{\rho=0}^z \int_{\phi=0}^{2\pi} \frac{1}{\pi N_0} e^{-\frac{\rho^2+A^2}{N_0}} e^{\frac{2\rho A \cos \phi}{N_0}} \rho d\phi d\rho \\ &= \int_{\rho=0}^z \frac{\rho}{\pi N_0} e^{-\frac{\rho^2+A^2}{N_0}} \int_{\phi=0}^{2\pi} e^{\frac{2\rho A \cos \phi}{N_0}} d\phi d\rho \\ &= \int_{\rho=0}^z \frac{2\rho}{N_0} e^{-\frac{\rho^2+A^2}{N_0}} I_0\left(\frac{2\rho A}{N_0}\right) d\rho \end{aligned} \quad (\text{B.10})$$

where I_0 is the modified Bessel function of the first kind of zero order. Then, the total probability of error is

$$p_e = \frac{1}{2} \left[\int_z^\infty \frac{2\rho}{N_0} e^{-\frac{\rho^2}{N_0}} d\rho + \int_{\rho=0}^z \frac{2\rho}{N_0} e^{-\frac{\rho^2+A^2}{N_0}} I_0\left(\frac{2\rho A}{N_0}\right) d\rho \right] \quad (\text{B.11})$$

Note that the probability distribution functions (the integrands) and the optimal threshold shift to the right with decreasing SNR (see Figure B.2). Therefore, to improve the detection of symbols, the threshold z must change.

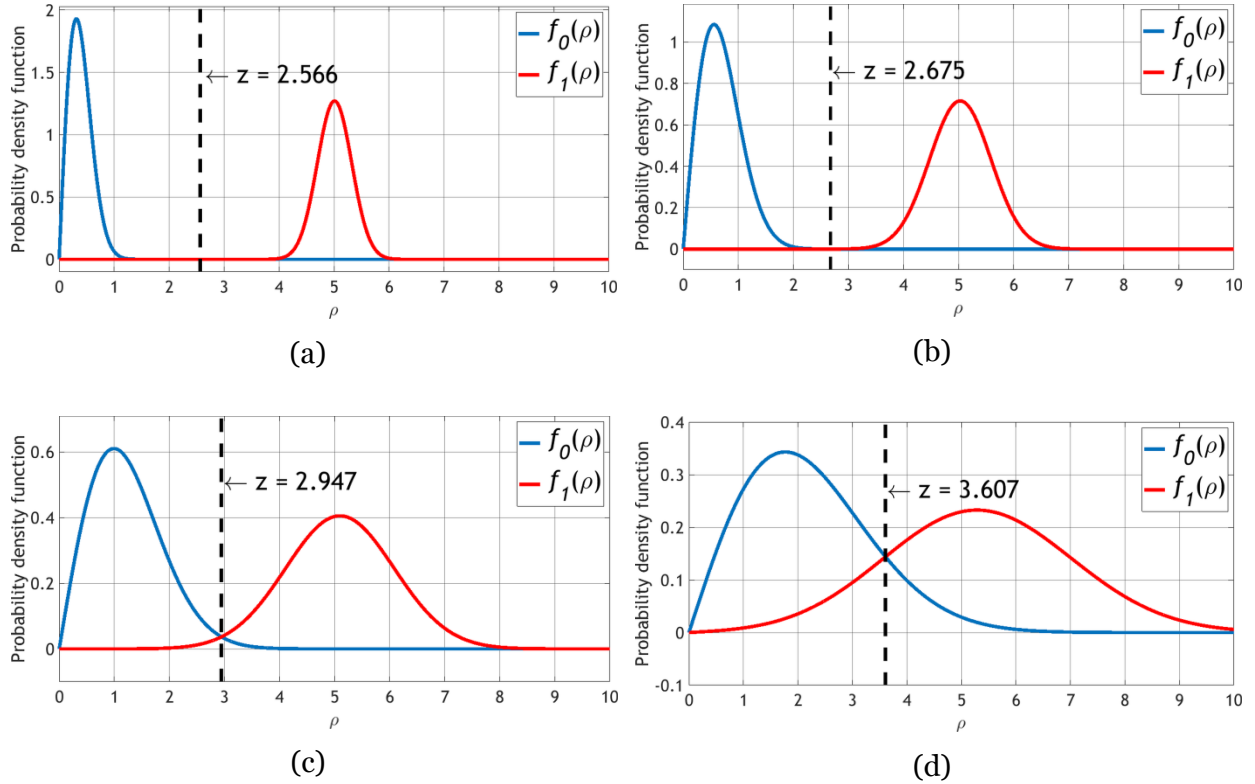


Figure B.2 Shifting threshold level as the SNR decreases for SNRs of (a) 15 dB, (b) 10 dB, (c) 5 dB, and (d) 0 dB. The noise distribution is $f_0(\rho)$ and $f_1(\rho)$ when bit 0 and bit 1 are transmitted, respectively, with $A = 5$.

Appendix C. Envelope Detector Algorithm

